1-1-2015

Understanding The Physics Of Magnetic Nanoparticles And Their Applications In The Biomedical Field

Suvra Santa Laha
Wayne State University,

UNDERSTANDING THE PHYSICS OF MAGNETIC NANOPARTICLES AND THEIR APPLICATIONS IN THE BIOMEDICAL FIELD

by

SUVRA SANTA LAHA

DISSERTATION

Submitted to the Graduate School

of Wayne State University

Detroit, Michigan

in partial fulfillment of the requirements

for the degree of

DOCTOR OF PHILOSHOPY

2015

MAJOR: PHYSICS

Approved by:

_____

Advisor Date

_____

_____

_____

_____

DEDICATION

To the memory of my father

Shri Bhanu Kumar Laha

ACKNOWLEDGEMENTS

I would like to acknowledge my principal advisor Prof. Gavin Lawes for all his support and help during the major part of my PhD career (Jan. 2011 – Dec. 2013). I am deeply thankful to my current advisors Prof. Christopher V. Kelly (from Physics) and Prof. Bhanu P. Jena (from Physiology) for their valuable guidance during the final years of my doctoral studies. Their constant encouragement and advice helped me in successful completion of my thesis work. I am also grateful to both Prof. Ratna Naik and Prof. Zhixian Zhou for being my committee members and also providing me with appropriate guidance whenever needed. Special thanks also go to Prof. Joseph Rakowski from Radiation Oncology who played a pivotal role as one of our research collaborators and also as my external committee member.

I received a tremendous amount of co-operation from both my past (Parashu, Ron Ambesh, Rajesh & Akila) and present group members (Ehab & Maheshika). I personally benefitted from each one of them on several occasions through useful discussions. I would also like to thank all my Condensed Matter colleagues at Physics@Wayne, including Ajay, Humeshkar, Kulwinder and Rupam for all their valuable support over the last few years.

I would also extend my sincere gratitude to all the fine teachers especially Prof. Gavin Lawes, Prof. J.J. Chang, Prof. Ashis Mukhopadhay, Prof. Sean Gavin, Prof. Zhixian Zhou and Prof. Boris Nadgorny who taught me and helped me in understanding the fundamentals of physics and its related disciplines. Prof. Jo Wadehra's guidance as a Graduate advisor starting from the very first day after I reached Wayne State also deserves special mention. Lastly, I am grateful to all my family, friends and colleagues who supported me throughout my PhD career and especially during the difficult phase of my life which I encountered at Wayne State.

TABLE OF CONTENTS

LIST OF TABLES

LIST OF FIGURES

CHAPTER 1

INTRODUCTION

With sizes ranging between 1 nm to 100 nm at least in one dimension, nanoparticles often have electrical, magnetic, and chemical properties that differ from their bulk counterparts [1, 2]. A high percentage of atoms in nanoparticles are at the material's surface, which typically reduces the material's net crystalline organization, electrical conductivity, and magnetic saturation. This size-dependence of the material properties thereby results in diverse phenomena, including the quantum confinement effect observed in semiconductor particles [3], the surface plasmon resonance in some metallic nanoparticles [4] and the phenomenon of superparamagnetism in magnetic nanomaterials [5]. As such, these tiny particles have immense potential and are expected to be building blocks for a wide range of future applications. Nanoparticles manifest in several different shapes, namely the nanospheres [6, 7], nanotubes [8], nanorods [7, 9, 10], nanoribbons [8, 11], and nanoflowers [12]. Some of the most common synthetic nanoparticles include carbon nanotubes, fullerenes (C 60), quantum dots (CdTe, CdSe, InAs), polymeric nanoparticles, dendrimers, inorganic (TiO_2, ZnO), metallic (gold, silver, copper, iron) and magnetic nanoparticles (Fe_3O_4, NiO, $NiFe_2O_4$).

This dissertation focuses on understanding and controlling the magnetic properties of nanoparticles. The magnetic nanoparticles are of great interest because of their potential uses in magnetic-recording, medical diagnostic and therapeutic applications. Additionally, they also offer an opportunity to understand the physics underlying the complex behavior exhibited by these materials. This dissertation describes the relaxation dynamics, surface phenomena, and magnetic dipolar interactions existing in nanoparticles that are of particular interest in biomedical applications. We have also investigated how these tiny structures can be utilized in magnetic hyperthermia and can also be incorporated to cell membranes for various detection and treatment

purposes. The intracellular distribution of these nanoparticles is a topic of intense scientific research because it can actually reveal to what subcellular organelle these nanoparticles will localize after penetrating through the cell membrane. A thorough study in this specific area could serve as a paradigm shift and can open a new chapter in the future nanomedicine research.

1.1 MAGNETIC MATERIALS AND MAGNETIC NANOPARTICLES

Bulk magnets can be classified into the following categories. They are *diamagnets* (*e.g.*, water, copper, bismuth), *paramagnets* (*e.g.*, aluminum, magnesium, sodium) *ferromagnets* (*e.g.*, iron, cobalt, nickel), *ferrimagnets* (Fe_3O_4, $NiFe_2O_4$, Mn_3O_4) [13-15] and *aniferromagnets* (FeMn, NiO, MnO) [14, 16, 17]. The magnetization (M) exhibited by a material is found to be proportional to the applied field (H), and can be expressed as $M=\chi H$, with the constant of proportionality being the volumetric magnetic susceptibility (χ). χ is small but negative for diamagnets (-10^{-6} to -10^{-3}) while it is small and positive for paramagnets (10^{-6} - 10^{-1}) [18]. The ferro, ferri and the antiferromagnets possess a positive value of χ, which is generally the largest in the case of ferromagnets (10^3 - 10^4). The ferromagnets and ferrimagnets also exhibit a phenomenon called hysteresis (figure 1.1), which is caused by domain wall motion [18]. A domain is the region within the material where the atomic magnetic moments are aligned in the same direction. The magnetization retained by a sample even after complete removal of the applied field is called the remanent magnetization (M_r). The field required in the opposite direction to demagnetize a sample after it has achieved saturation magnetization (M_S) is called the coercive field or coercivity (H_C) [2, 18, 19].

The magnetic moment of nanoparticles are more affected by thermal fluctuations than their bulk counterparts [20]. In sufficiently small ferromagnetic or ferrimagnetic particles,

thermal fluctuations can alter the direction of their magnetic moments giving rise to the phenomenon known as superparamagnetism (SPM). SPM can evolve into a spin-glass-like behavior with an increase in the interaction energy amongst the nanoparticles [21]. In the following sections, a detailed explanation on magnetic anisotropy, superparamagnetism, spin-glass behavior, and biomedical applications in context to magnetic nanoparticles is provided.

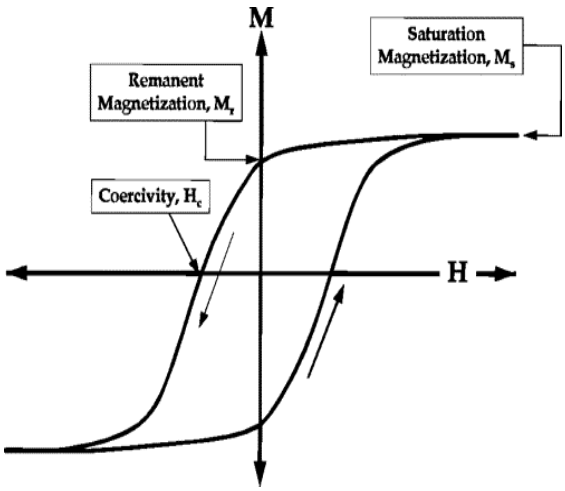

Figure 1.1 Magnetization (M) *vs* Magnetic Field (H) loop showing hysteresis [2].

1.2 ANISOTROPY IN MAGNETIC NANOPARTICLES

The difference in magnetic energy to produce saturation in a hard and an easy direction is called the anisotropy energy. Along the easy and hard directions, saturation magnetization is achieved by applying relatively small and large fields respectively. The two most prominent anisotropies observed in magnetic nanoparticles are magneto-crystalline anisotropy and shape anisotropy [2].

a) Magneto-crystalline anisotropy

The easy and hard directions arise from the interaction of the spin magnetic moment with the crystal lattice. This phenomenon results in spin-orbit coupling which produces the magneto-

crystalline anisotropy [2]. For simplicity we consider uniaxial anisotropy in magnetic nanoparticles [2, 18] and the magneto-crystalline anisotropy energy (E_A) is given by

$$E_A = KV\sin^2\theta \quad (1.1)$$

where, K is the magnetic anisotropy constant, V is the particle volume and θ is the angle between the magnetization vector (**M**) and an easy direction of magnetization (figure 1.2). Along the easy direction, one attains M_S even with a relatively small H. This energy has two minima at θ = 0° and 180°; the spins flip between these two stable energy minima that are separated by the anisotropy energy barrier E_A [22]. The magneto-crystalline anisotropy constant 'K' for bulk magnetite is 1.35×10^5 erg/cc [23]. The anisotropy constant is an inherent property of the material and is not influenced by its shape. Also, larger values of K result in larger H_C of a material.

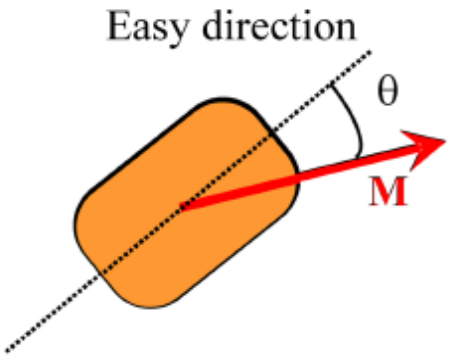

Figure 1.2 Magnetization vector **M** makes an angle θ with the easy axis of a nanoparticle [20].

b) Shape anisotropy

The dipole interactions within a material are long-ranged and yield a variation in the magnetization depending on the shape of the particle. Shape anisotropy is caused by dipolar interactions within non-spherical particles. A perfectly spherical nanoparticle having symmetry along all possible directions will carry no shape anisotropy whereas non-symmetric structures, like cylindrical particles, do possess shape anisotropy [2]. In thin films, the magnetic moments

tend to align with the plane of the film, whereas in nanorods the alignment is along the axis of the rod.

1.3 SUPERPARAMAGNETISM

Superparamagnetism, a prominent nanomagnetic phenomenon is observed in single domain nanoparticles. In a single domain particle, every spin within the interior of the particle points in the same direction with the total magnetic moment of the particle being equal to the sum of all the atomic spins. As evident from equation 1.1, the anisotropy energy of a particle is proportional to its volume. In sufficiently small magnetic nanoparticles (< 20 nm), the thermal energy becomes comparable with E_A. If the measurement time (τ_m) is large compared to the mean time for the spin relaxation (τ), then superparamagnetism is observed. Over the course of this measurement, the particle's spin will flip stochastically between the two stable minima orientations (figure 1.3) and its time-average magnetization reduces to zero, similarly to a paramagnet. Since a single domain magnet usually contains 10^4-10^5 atoms and the magnetic moment of an electron is equal to 1 Bohr magneton (μ_B), each superparmagnetic nanoparticle can have large net magnetic moments (>10,000 μ_B) as compared to paramagnets with a magnetic moment of ~1 μ_B [22]. Therefore, in this case, the nanoparticle apparently behaves like a paramagnet but with an enhanced magnetic moment, hence the name *superparamagnetism*.

If $\tau_m << \tau$, the particle's spin will not undergo a complete flip during this measurement time, and it will appear to be in a blocked state. The temperature at which $\tau_m=\tau$ is defined as the blocking temperarture (T_B). Therefore, below T_B, the particles' spins are blocked while above this temperature they behave as a superparamagnet following the T^{-1} dependence of the Curie's law.

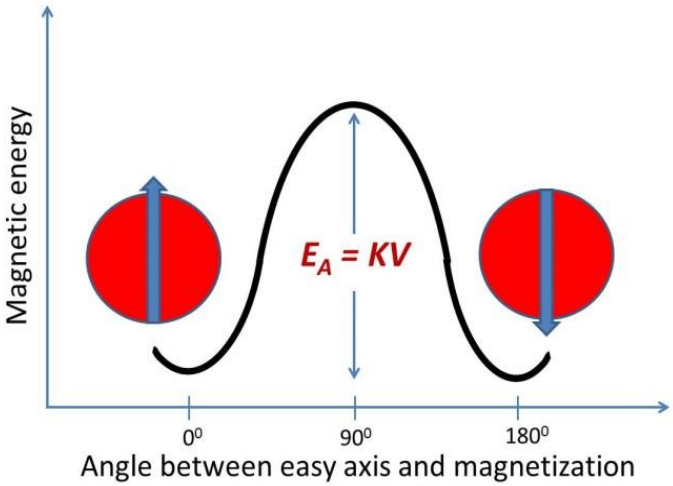

Figure 1.3 The particle spin flips overcoming the anisotropy energy barrier (E_A).

SPM is demonstrated by a sigmoidal, anhysteretic M *vs* H plot (figure 1.4). The mean relaxation time of the particle spin is given by the Néel–Brown equation, $\tau = \tau_0 \exp(KV/k_BT)$, where k_B is the Boltzmann's constant, T is the temperature and τ_0 is the attempt time characteristic of the material. In case of SPM, the magnitude of τ_0 is of the order of 10^{-13}–10^{-9} s [22, 24]. Typical for laboratory measurements with $\tau \approx 100$ s and $\tau_0 \approx 10^{-9}$ s, T_B from the Néel–Brown equation approximately equals $25KV/k_B$.

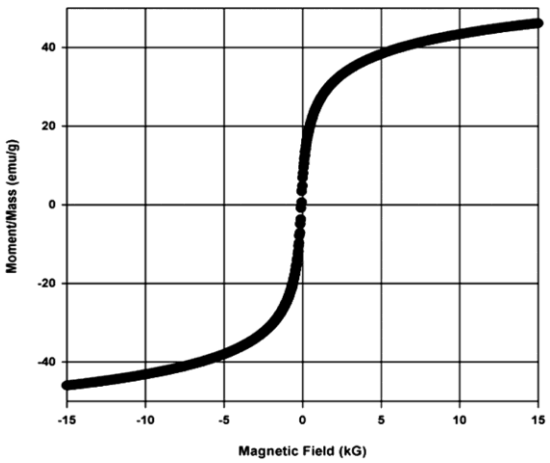

Figure 1.4 Magnetization (M) *vs* Magnetic Field (H) plot for γ-Fe_2O_3 nanoparticles showing superparamagnetic behavior [25].

When the size of a nanoparticle falls below a critical value (D_c), it becomes single domain. However, a single domain particle may still show a large value H_c (figure 1.5). A superparamagnetic nanoparticle must have only a single domain, but a single domain nanoparticle may not be superparamagnetic. The area under the hysteresis loop is greatest for single domain particles with diameter = D_S, however, H_c gets reduced as the particle size increases. Generally, hysteretic behavior is associated with domain wall motion. However, in the case of large single domain nanoparticles, the hysteresis loss is instead achieved by spin rotation rather than domain wall motion, which effectively increases the H_C [2]. As the size of the nanoparticle continues to decrease, H_C approaches zero. At this limit, there is no hysteresis loss and the magnetization returns to zero on removal of the applied external magnetic field and SPM is observed. This specific property of exhibiting zero H_C and zero M_r enable important applications in the biomedical field. For example, SPM limits particle agglomeration at the tumor site even after removal of the external magnetic field [26].

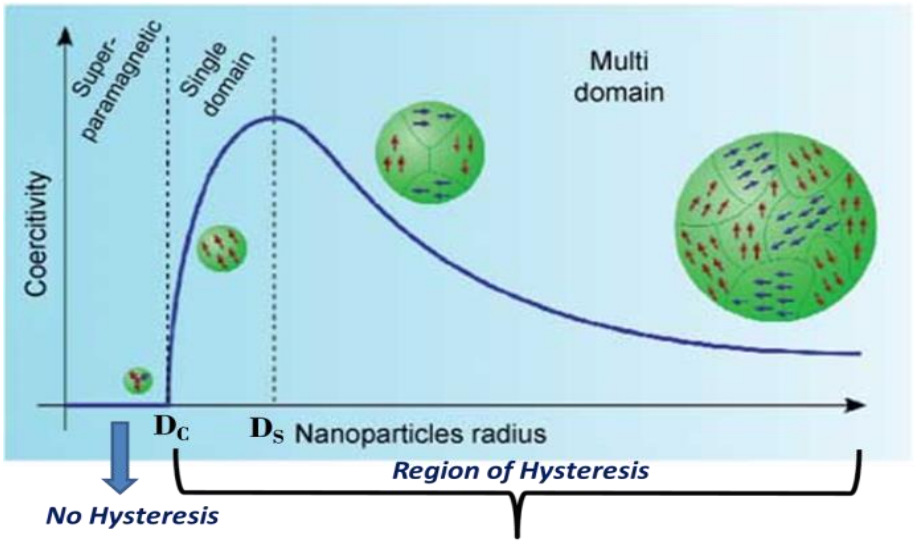

Figure 1.5 Coercivity (H_c) *vs* particle size (D) plot. [27]

The temperature dependence of the magnetization is studied under an applied magnetic field (usually 100 Oe) after the sample has been cooled in the presence (Field Cooled or FC) and in absence (Zero Field Cooled or ZFC) of a magnetic field. The peak of the ZFC curve gives a value for the blocking temperature T_B. Figure 1.6 shows the FC and ZFC measurements done on nanocrystalline nickel–zinc ferrites. The peak of the ZFC curve provides the value of T_B, which in this case is near 120 K [28]. In a typical ZFC measurement, when the nanoparticle sample is cooled in the absence of a magnetic field, their moments get randomly frozen in all possible directions below T_B. Then the magnetization *vs* temperature is studied by applying a nominal field while warming up the sample. Following an increase in temperature, the thermal energy becomes sufficient for some of the particles to overcome the anisotropy barrier. As the temperature keeps on increasing, more and more particles align with the applied field, as a result, the magnetization increases monotonically until it assumes its maximum value at T_B. In case of FC, since the sample is initially cooled in the presence of magnetic field, the particle moments tend to align themselves with the field. Therefore, during warming up of the sample, the FC curve shows an enhanced magnetization at temperatures below T_B as compared to the ZFC. However, beyond T_B, both FC and ZFC follow a typical T^{-1} dependence of the Curie's law signifying the superparamagnetic behavior of these particles.

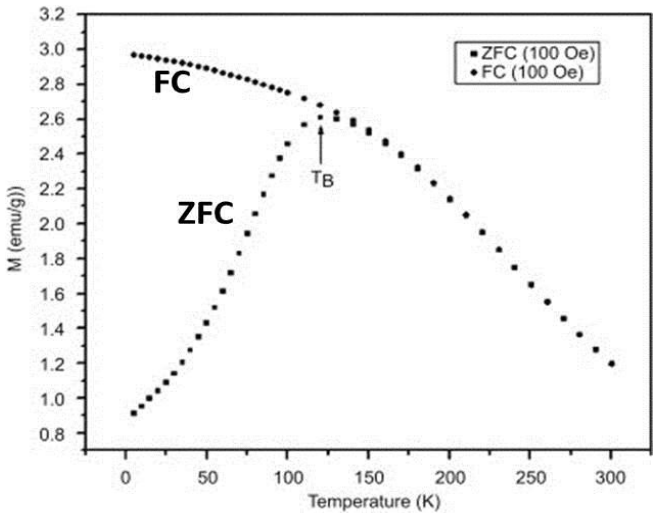

Figure 1.6 FC and ZFC curves for nanocrystalline nickel–zinc ferrites [28].

1.4 SPIN GLASS

The Neel-Brown (NB) model describes the behavior of an ensemble of non-interacting and single domain magnetic nanoparticles [29]. The relaxation time (τ) for the magnetic moments of such individual nanoparticles is governed by an Arrhenius relation given by $\tau = \tau_0 \exp(E_A/k_BT)$. The NB model describes SPM and blocking of the magnetic moments at high and low temperatures respectively [21]. Shtrikmann and Wohlfarth [30] considered the introduction of weak interactions to the NB model and described the τ using the Vogel-Fulcher relation given by $\tau = \tau_0 \exp [E_A/k_B(T-T_0)]$, where T_0 measures the strength of the interaction. However, when the interactions between the particles are strong enough, the relaxation time of the magnetic moments exhibits collective behavior following a specific power law given by $\tau = \tau_0[T_f/(T(\nu)-T_f)]^{z\nu}$, where T_f is the freezing temperature at the zero frequency limit, $T(\nu)$ is the frequency dependent freezing temperature and $z\nu$ is the critical exponent [24, 31]. This relaxation is no longer a single particle effect, but depends on the ensemble of nanoparticles. The particle spins get frozen in this state and is known as spin-glass-like freezing. The values of τ_0 and $z\nu$ are

typically in the range of 10^{-9}-10^{-13} s and 4-12 for the spin glass systems, respectively [24]. The freezing of the magnetic moments in an assembly of nanoparticles due to strong dipole-dipole interaction is sometimes referred to as *superspin freezing* shown in figure 1.7(a) [22, 32]. The dipole–dipole interaction energy (E_d) in an ensemble of randomly distributed magnetic nanoparticles is given by $E_d = \frac{\mu_o \mu^2}{4\pi a^3}\left(\frac{\pi}{4}\right)^2$, where, μ_0 is the permeability of free space, μ is the average magnetic moment, and *a* is the mean separation between the particles [22, 33]. For 10-12 nm Fe_3O_4 nanoparticles, with average magnetic moment of 10,000 μ_B, the interaction energy becomes comparable to thermal energy at 300 K when *a* = 6 nm.

Disorder can also be observed on the surface of sufficiently small particles because of the increased surface to volume ratio. With the decrease in particle size, the presence of more atoms in close proximity to the surface of the nanoparticles produces additional spin disorder, which can lead to glassy magnetic behavior [34]. The freezing of the spins on the surface of individual nanoparticles is referred to as *surface spin-glass freezing*, as shown in figure 1.7(b) [32]. Kodama *et al.* [35] have reported surface spin-glass freezing in Nickel ferrite ($NiFe_2O_4$) nanoparticles. The model proposed by Kodama *et al.* [35] mentions about a ferrimagnetic core of aligned spins surrounded by a shell having a disordered arrangement of surface spins. Winkler *et al.* [36] and Peddis *et al.* [37] have also shown surface spin freezing in Nickel Oxide (NiO) and Cobalt Ferrite ($CoFe_2O_4$) nanoparticles.

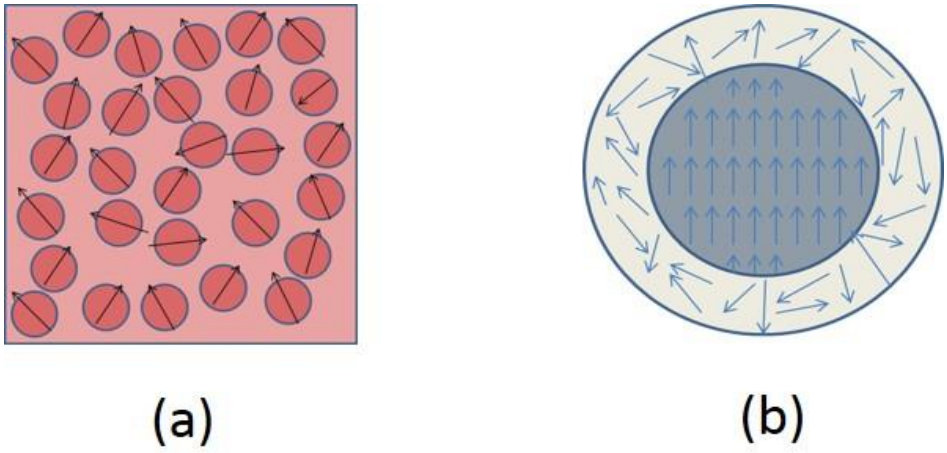

Figure 1.7 (a)Superspin glass freezing and (b) Surface spin glass freezing are mechanisms for reduced magnetization from superparamagnetic nanoparticles.

While the magnetic properties of many nanoparticle systems can be fully understood in the framework of the non-interacting Neel-Brown model, for some specific situations, the effects of interactions cannot be neglected. In these cases, the magnetic dynamics of the nanoparticles are often intermediate between non-interacting superparamagnetism and strongly interacting spin glass behavior. In order to distinguish these two regimes, a brief discussion of some of the most salient features of spin glasses is included below. Both superparamagnetic blocking and spin-glass-like freezing have similar features in out-of-phase *ac* susceptibility ($\chi^{//}$) *vs* T plots [38]. Tackett *et al.* [38] claimed that the low temperature relaxation in Mn_3O_4 nanoparticles arises from superparamagnetism whereas Nadeem *et al.* [32] reported surface spin-glass freezing in $NiFe_2O_4$ nanoparticles. Figure 1.8 shows the $\chi^{//}$ *vs* T for Mn_3O_4 nanoparticles with an average particle size of 13 nm. The inset clearly hints at the presence of low temperature features with the temperature peak shifting as the frequency changes. Similarly, figure 1.9 shows frequency dependent temperature peaks in the low temperature range for $NiFe_2O_4$ nanoparticles of size 8 nm. The $\chi^{//}$ *vs* T plots are qualitatively similar for both cases; it is not possible to clearly

distinguish between SPM and spin-glass behavior just from the presence of low temperature relaxation.

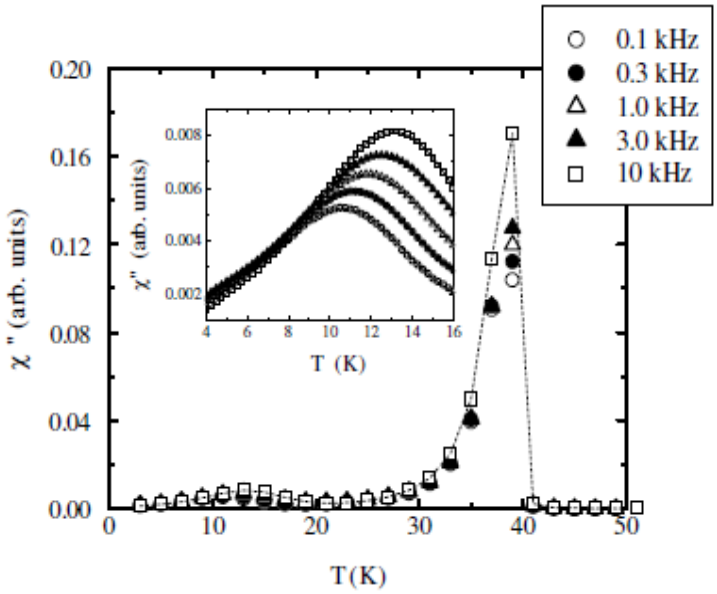

Figure 1.8 $\chi^{//}$ *vs* T graph for Mn_3O_4 nanoparticles with an average particle size of 13 nm. The inset shows the magnified version of the T dependence on $\chi^{//}$ at the low temperature regime for five different frequencies [38].

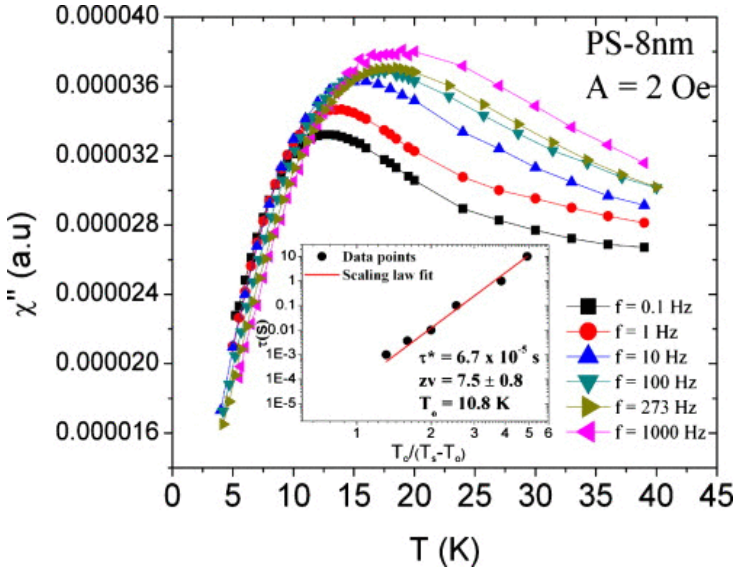

Figure 1.9 $\chi^{//}$ *vs* T graph for $NiFe_2O_4$ nanoparticles for six different frequencies with particle size of 8 nm. The inset shows the best fit of the dynamic scaling law [32].

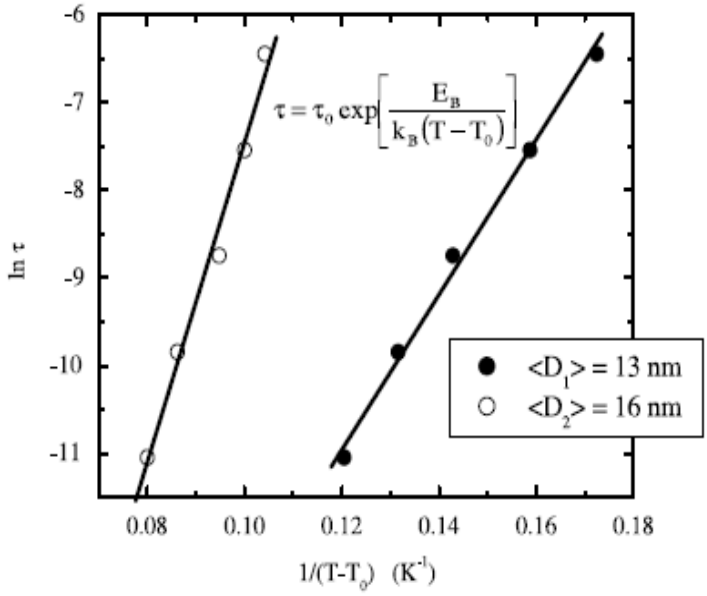

Figure 1.10 Vogel Fulcher fit for slightly interacting particles of Mn_3O_4 having diameters of 13 nm and 16 nm [38].

Therefore, we will rely on specific parameters to determine whether a phenomenon is SPM blocking (non-interacting behavior) or spin-glass freezing (strongly interacting behavior). If a plot of ln τ *vs* (1/T) follows the functional form expected for the NB model or a plot of ln τ *vs* 1/ (T-T_0) for a small T_0, as is appropriate for a Vogel Fulcher dependence for a weakly interacting system, and yields τ_0 in the range of 10^{-9}-10^{-13} s [24], then we suppose that the relaxation at low temperature is due to SPM blocking. However, if a plot of ln τ *vs* ln [(T(ν)/T_f) – 1] gives a straight line with the value of τ_0 in the range of 10^{-9}-10^{-13}s and the critical exponent (zν) lying between 4 – 12 [24], then the low temperature relaxation arises because of spin-glass behavior. Tackett *et al.* [38] have shown that a linear relation exists between ln τ and 1/ (T-T_0) following the Vogel-Fulcher law with the value of τ_0 being equal to 10^{-10}s and T_0 = 4.8 K (figure 1.10). This suggests that superparamagnetic blocking is responsible for the magnetic relaxation observed in Mn_3O_4 nanoparticle ensemble at low temperatures. On the other hand, the inset in

figure 1.9 depicts a linear relation between τ and $[T_o/(T_s-T_o)]$ following the non-exponential relaxation and indicates the presence of spin-glass freezing in these nanoparticles. Here, T_o is the freezing temperature at the zero frequency limit and T_s is the frequency dependent temperature of the peak. Nadeem *et al.* [32] have estimated the value of zv and τ_0 to be equal to 7.5 and 6.7×10^{-5} s respectively. A higher value of τ_0 is due to the fact that frozen agglomerates of highly disordered and frustrated surface spins have a much longer relaxation time.

Another parameter used to differentiate between the blocking and the freezing process is given by $\alpha = \Delta T/ [T^*\Delta (\log_{10} f)]$. Here ΔT is the difference between two frequency (f) dependent temperatures (freezing or blocking) and T is the mean value between them. In a typical spin glass system, the value of α lies between 0.005 and 0.05 whereas for non-interacting and weakly interacting systems α assumes a value usually greater than 0.05 [24, 31]. Tackett *et al.* [38] have calculated the value of α to be 0.11 for their Mn_3O_4 nanoparticles and thus reported superparamagnetism at low temperatures in this system.

As discussed by Tackett *et al.* [38] the collective spin-glass freezing temperature remains relatively insensitive to the average particle size of an ensemble of nanoparticles while the SPM blocking temperature strongly depends on the nanoparticle size. The blocking temperature in an ideal SPM system is directly proportional to the cube of the average particle size. If T_B be the blocking temperature and D the mean diameter of the nanoparticles, then T_B is proportional to D^3 for non-interacting nanoparticles while (T_B-T_0) is proportional to D^3 for the weakly interacting systems. Tackett *et al.* [38] have confirmed low-temperature superparamagnetism in Mn_3O_4 nanoparticles by showing the blocking temperature shift for two different sizes of the nanoparticles. In this system, T_B changed significantly from 10.3 K to 14.8 K with the increase in

mean particle size from 13 nm to 16 nm, respectively, for a specific frequency of 100 Hz (figure 1.11).

Nadeem *et al.* [32] have shown that the surface spin-glass freezing temperature remains unchanged with a change in particle size for $NiFe_2O_4$ nanoparticles. The freezing temperature remains at about 15 K even as the particle size varies from 8 nm to 12 nm (figure 1.12). The graph also shows that the freezing becomes more dominant with decreasing particle size, which supports the fact that the fraction of disordered spins at the surface is greater for particles with an increased surface to volume ratio.

Peaks for both superparamagnetism (blocking temperature, T_B) and spin-glasses (freezing temperature, T_f) are observed in a zero-field cooled (ZFC) plot. [39]. The difference being, that generally below T_B, the FC curve attains or tends to attain saturation in the case of a spin-glass system [39], while it keeps on increasing with no tendency to reach saturation for superparamagnetic particles, indicating that the inter-particle interactions do not influence the relaxation dynamics [40] .

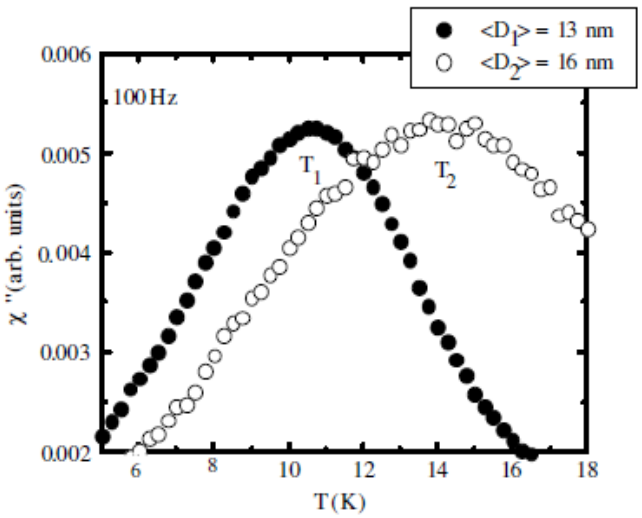

Figure 1.11 The size dependency on the blocking temperature for Mn_3O_4 nanoparticles having diameters of 13 nm and 16 nm [38].

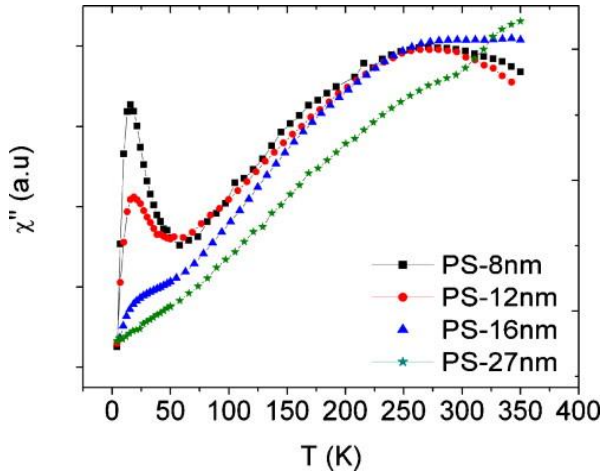

Figure 1.12 The freezing temperature (T_f) remains unaffected with varying particle size for $NiFe_2O_4$ nanoparticles [32].

1.5 BIOMEDICAL APPLICATIONS OF MAGNETIC NANOPARTICLES

Nanoparticles have played a significant role in modernizing present healthcare industries. There has been extensive use of gold [41, 42], silver [43], iron [44], silica [45], and polymeric nanoparticles [46] for the detection and treatment of various deadly diseases. The interaction of nanoparticles with the human cell line has been widely studied in the recent years. Researchers have worked with silver [47], gold [48], zinc oxide [49] , silica [50], cerium oxide [51] to investigate the distribution and cytotoxicity of these nanoparticles. In the last decade, the superparamagnetic nanoparticles, especially iron oxide based nanoparticles have emerged as a potential candidate in the field of nanomedicine with their applications ranging from molecular imaging, targeted drug/gene delivery to regenerative medicine, tissue engineering [52-57].

1.5.1 Magnetic nanoparticles for drug delivery applications

Magnetic nanoparticles have been applied widely in the field of targeted drug delivery. Because of their magnetic nature, these tiny particles can be driven directly at the tumor site by

means of an externally applied magnetic field [58, 59]. This promotes accumulation of magnetic nanoparticles in close proximity to the cancer cells (specific targeting) without affecting the healthy tissues of the human body, hence reducing the possibility of adverse side effects [58, 59]. At the tumor site, these nanoparticles carrying anti-cancer drugs release the medicine either by enzymatic activity, or via changes in the physiological conditions like pH and temperature [58]. The superparamagnetic behavior of iron oxide nanoparticles of less than 20 nm diameter at room temperature coupled with its biocompatibility and non-toxic nature makes them well suited for in-vivo applications [60]. Since they possess a sufficiently high value of saturation magnetization (M_s ~ 65-70 emu/g) [61], they can be well guided to the tumor site by an externally applied magnetic field. However, due to their superparamagnetic behavior, they do not agglomerate even after the removal of the external applied field [62]. Further, the surface functionalized iron oxide nanoparticles conjugated with the chemotherapy drug doxorubicin creates a widely studied anti-cancer therapeutic complex. Researchers have shown that PEG (Polyethylene Glycol) functionalized porous silica shell onto doxorubicin-conjugated Fe_3O_4 nanoparticle cores [63], PAMAM (Poly(amidoamine)) coated Fe_3O_4 nanoparticles-doxorubicin complex [64], doxorubicin loaded Fe_3O_4 nanoparticles modified with PLGA-PEG copolymers [65] could potentially serve as a promising candidate in therapeutic cancer treatment.

1.5.2 Magnetic nanoparticles for hyperthermia

At the tumor site, localized heating by magnetic nanoparticles can also cause effective damage to the malignant tissues [27]. Elevated temperatures above the physiological body temperature (40^o - 45^oC) have been found to inhibit the growth of the cancer cells without affecting the normal tissues [62, 66]. For example, a colloidal suspension of magnetic

nanoparticles, known as ferrofluids, when subjected to an alternating magnetic field is capable of dissipating heat energy in the surrounding medium [66]. This heat energy is basically produced as a result of hysteresis loss and also due to two prominent relaxation phenomena occurring in magnetic nanoparticles: (a) Neel and (b) Brownian relaxation [66]. In the former, the magnetic spin of the particle simply rotates while the latter is caused by the effective rotation of the entire particle as shown in figure 1.13. The specific absorption rate commonly known as SAR (usually expressed as W/g) is an important parameter in magnetic hyperthermia studies. SAR is a measure of the heat energy absorbed by the magnetic nanoparticles per unit mass under an alternating magnetic field of certain amplitude and frequency and is expressed as

$$\text{SAR} = \frac{C}{m} \times \frac{dT}{dt}$$, where C is the specific heat capacity of water per unit volume, m is the concentration (in g/L) of the magnetic material in solution and $\frac{dT}{dt}$ is the rate of change of temperature. [66]. An elevated SAR value, which is an essential requirement for effective cancer hyperthermia treatment, can be achieved by increasing the amplitude (A) and the frequency (f) of the magnetic field. However, beyond a certain threshold value ($A \times f = 5 \times 10^9$ $Am^{-1}s^{-1}$) [66], clinical trials on human may give rise to certain complications. Therefore, developing an efficient magnetic nanoparticle system with optimized SAR value is a crucial challenge in magnetic hyperthermia (MHT) research for cancer treatment.

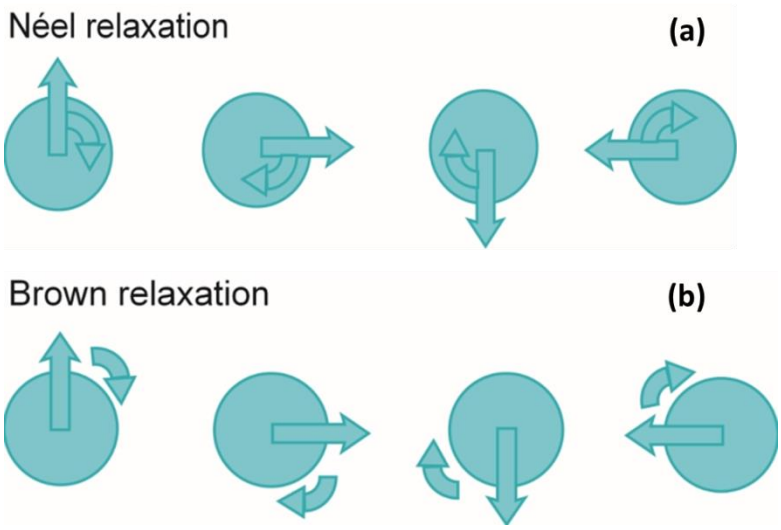

Figure 1.13 (a) The Neel relaxation shows the rotation only the magnetic spin with the particle being fixed (b) The Brownian relaxation indicates the physical rotation of the entire particle. (Image by courtesy of nanotherics.com)

1.5.3 Magnetic nanoparticles as contrast agents in MRI imaging

MRI is a valuable, non-invasive imaging methodology for many ailments and diseases; however, it often lacks contrast between tumor and healthy tissue in cancer diagnosis. MRI measures the relaxation rates of the hydrogen nuclei in water, which are affected by the local magnetic environment that differs between different tissue types. The hydrogen nuclei within the water naturally align in the direction of the external magnetic fields, and, when the appropriate radio frequency pulses are introduced, these protons are excited. When the pulses are switched off, the protons precess and relax to their original position while emitting characteristic electromagnetic signatures. This emission is used to visualize the morphology of the human body tissues as different tissue types yield different emission. While natural and diseased tissues occasionally emit indistinguishable signals, these signals can be made distinct and, therefore, images can further be sharpened by introducing *contrast agents* that are conjugated to biomarkers or antibodies for specific targeting to diseased tissues. MRI contrast is characterized

by the two major spin relaxation processes namely T_1 (spin-lattice or longitudinal) and T_2 (spin-spin or transverse). The magnetic contrast agents change the rates of these relaxation processes for the tissue that surrounds them. The paramagnetic gadolinium chelate complexes are known to accelerate the T_1 relaxation rates producing 'bright' contrasts whereas the superparamagnetic iron oxide nanoparticles play an important role as a T_2 enhancer creating 'dark' or negative contrasts [18, 67, 68].

1.6 SCOPE OF THE THESIS

This dissertation describes the fundamental physical principles governing magnetic nanoparticles and also how nanomagnetism plays a prominent role in biomedical applications. Chapter 2 of this thesis introduces the working principles of the key characterization techniques used throughout this research. In Chapter 3, studies involving structural, optical, and *ac* magnetic properties in undoped and doped (*B*, *Co*, *Gd*, *La*) Fe_3O_4 nanoparticle systems are presented. The Chapter 4 describes the magnetic dipolar interactions in two different systems of iron oxide nanoparticles. Understanding interactions and magnetic relaxation in undoped and boron doped Mn_3O_4 nanoparticles are included in Chapter 5. The magnetic properties and possible biomedical applications of dextran coated undoped and Gd-doped Fe_3O_4 as well as $BiFeO_3$ nanoparticles are also investigated in Chapter 6, Chapter 7 and Chapter 8. Finally, the conclusions and future work are placed in Chapter 9.

CHAPTER 2

MAJOR EXPERIMENTAL TECHNIQUES

This chapter describes the basic working principles of some of the characterization techniques used in this dissertation. They are as follows: 1. X-ray Diffraction, 2. Raman Spectroscopy, 3. Scanning Electron Microscopy, 4. Transmission Electron Microscopy, 5. Dynamic Light Scattering & Zeta Potential measurements, 6. Physical Property Measurement System, and 7. Magnetic Hyperthermia (MHT) Measurements.

2.1 X-RAY DIFFRACTION (XRD)

The crystallite size and phase identification of a sample can be obtained from the XRD analysis. The XRD works on the basic principle of Bragg's law given by,

$$2d_{(hkl)} \sin\theta = n\lambda \tag{2.1}$$

where, $d_{(hkl)}$ is the spacing between the atomic planes corresponding to the Miller indices hkl, θ is the angle between the incident rays and the atomic planes, n is any positive integer and λ is the wavelength of the incident rays. This Bragg's condition is satisfied only when the incident rays, with wavelength comparable to the lattice spacings, undergo a constructive interference after getting reflected from the atomic planes.

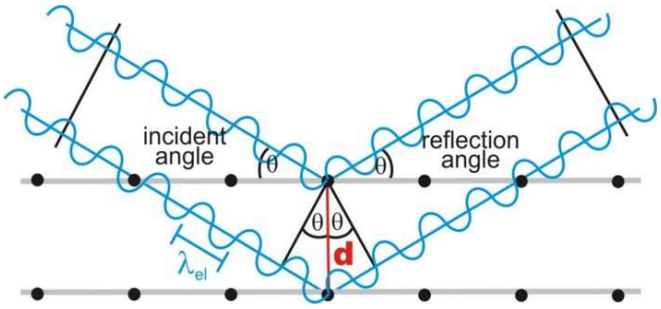

Figure 2.1 The X-rays after reflection from the atomic planes undergo constructive interference (image courtesy of ETH, Zurich).

The average crystallite size of the nanoparticles is calculated using the Debye-Scherrer equation

$$d_{avg.} = \frac{k\,\lambda}{\beta_{FWHM} cos\theta} \tag{2.2}$$

where, $d_{avg.}$ is the average crystallite size of the particle, λ is the X-ray wavelength, k is the shape factor which is roughly equal to 0.94 for spherical particles, β_{FWHM} is the full width at half maxima (in radians) of the diffraction peak, and θ is angle of diffraction. The $d_{avg.}$ is inversely related to β_{FWHM}, indicating that the peak width increases for a decrease in the crystallite size. For investigation of the crystalline structure and phase purity of our nanoparticle samples, we used a Rigaku MiniFlex 600 X-ray diffractometer with a θ-2θ scanning mode (*i.e.*, stationary source, rotating stage, and rotating detector) as shown in figure 2.2 (a) generating Cu K_α radiation (λ = 1.54 Å) under a supply voltage of 40 kV and an emission current of 15 mA. In a typical θ-2θ scanning mode, the x-ray beam is incident at an angle θ with the lattice planes, and then gets diffracted making an angle 2θ with the direction of incidence. Finally, the intensity of the diffracted beam is recorded as a function of 2θ as shown in a typical XRD spectrum in figure 2.2 (b).

(a)

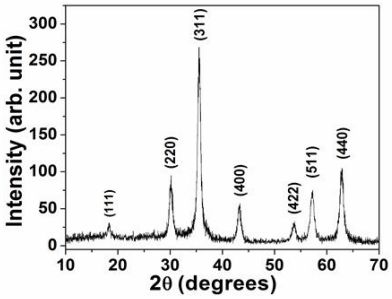

(b)

Figure 2.2 (a) The Rigaku MiniFlex 600 XRD instrument used for our nanoparticle analysis. (b) A typical XRD spectrum of Fe_3O_4 nanoparticles.

2.2 RAMAN SPECTROSCOPY

Proposed by the Indian scientist Sir C.V. Raman in 1928, this is a highly sophisticated spectroscopic technique used for analyzing rotational, vibrational and other low frequency transitions in molecules of solids, liquids and gaseous samples. It is based on the principle of inelastic scattering of monochromatic light, usually from a laser source. The laser light initially interacts with the molecules of the sample and emits photons of both lower (ν-$\delta\nu$) and higher (ν+$\delta\nu$) frequencies as compared to the frequency of the parent monochromatic source (ν). The photons thus emitted with lower and higher frequencies are termed as Stokes and Anti-Stokes lines respectively (figure 2.3(a)). Information regarding a specific sample can be obtained from these characteristic lines, which are collectively called the Raman lines. The Raman scattered light is collected by the detector while a notch filter cuts off the effect of the Rayleigh photons. The Raman measurements were conducted on our nanoparticle samples at room temperature using a Raman spectrometer (HORIBA Jobin Yvon, Triax 550 detector) emitting green light (λ = 514.5 nm) from an Ar^+ ion laser source. Solid nanoparticle samples in the form of pellets were used for the characterization purposes. In a typical Raman spectrum, the scattered intensity is plotted as a function of wavenumber (cm^{-1}) as shown in figure 2.3 (b).

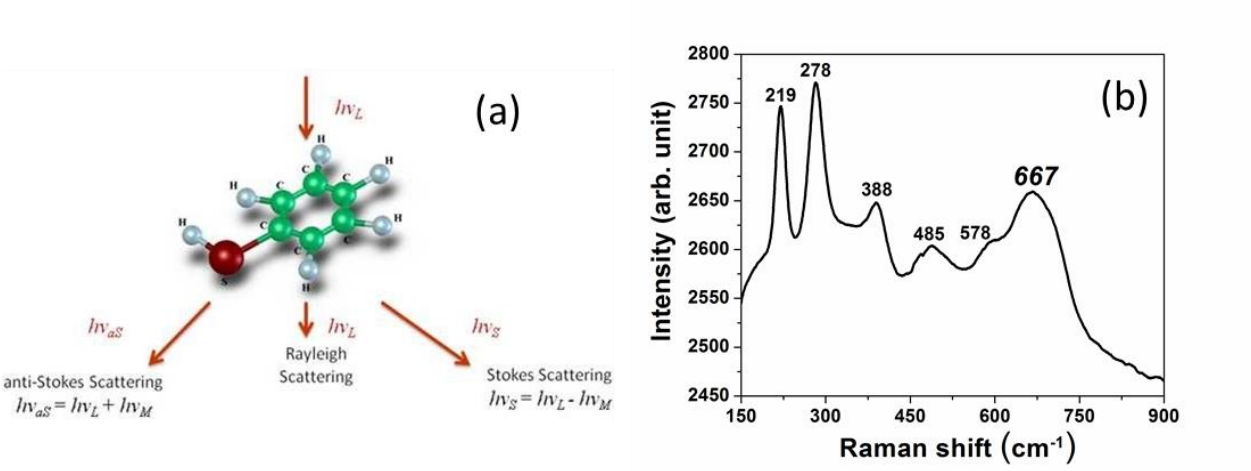

Figure 2.3 (a) Schematic showing the Raman scattering [69] (b) A typical Raman spectrum of boron doped Fe_3O_4 nanoparticles showing the 667 cm^{-1} peak corresponding to Fe_3O_4 along with the presence of amorphous secondary phase of goethite (α-FeOOH).

2.3 SCANNING ELECTRON MICROSCOPY (SEM)

In a SEM, a highly focused beam of electrons emanating from an electron gun is targeted onto the surface of the sample. Before interacting with the sample, the electrons travel through a vacuum and are guided by electromagnetic lenses. When the electron beam hits the surface of the sample, X-rays, secondary electrons, backscattered electrons, and Auger electrons are ejected (figure 2.4). These ejected electrons and X-rays carry useful information regarding the morphology, chemical composition and crystalline properties of the sample, and therefore they are collected by a detector. The detector is connected to a computer screen in which one can see the high resolution 2D images of the sample. Generally in SEMs, the sample to be studied needs to be electrically conductive or is given a conductive coating (*i.e.*, gold). The secondary electrons mainly originating from areas in proximity to the surface of the sample give information pertaining to topography. Backscattered electrons and the characteristic X-rays coming from deeper regions inside the sample provide details regarding the chemical composition of the sample. Unlike light microscopes, electrons are used instead of ordinary light and hence the

much enhanced resolution of the images photographed by a SEM versus optical microscopes. SEMs incorporating energy dispersive spectroscopy (EDS) and wavelength dispersive spectroscopy (WDS) provide elemental composition details of the sample. While EDS is the most commonly used technique for elemental detection, but with elements having low atomic numbers (generally Z<10), WDS plays a very important role. For our boron doped nanoparticles, we used WDS for the detection of boron; however, we failed to quantify its actual content in our samples due to the absence of proper standards. In all other cases, we have adopted the EDS technique to roughly estimate the dopant concentrations (Co, Gd, La) in our doped nanoparticle systems.

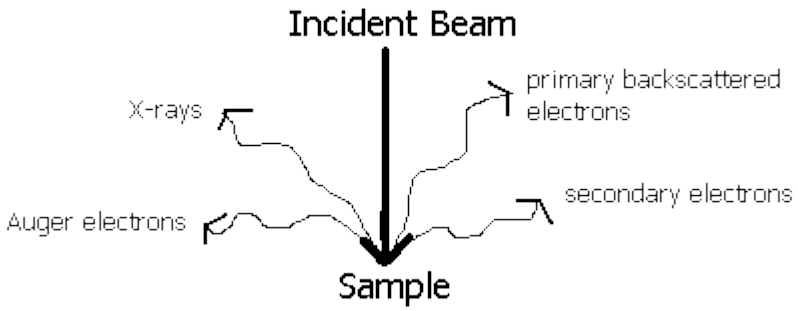

Figure 2.4 The electrons (secondary, backscattered and Auger) and X-rays are ejected when high-energy focused electron beam strikes the sample surface in a SEM. (image courtesy of Purdue University).

2.4 TRANSMISSION ELECTRON MICROSCOPY (TEM)

Like SEM, a TEM is also a 2D imaging technique with sub-nanometer resolution. The electrons originating from an electron gun are focused into a thin beam by means of electromagnetic lenses. The concentrated electron beam is incident on a very thin sample to facilitate sufficient transmission of electrons through it. These electrons are absorbed, scattered

or transmitted through the sample. For our experiments, we generally use one or two drops of a very dilute solution of nanoparticles dispersed in ethanol before mounting them on a carbon coated copper grid for capturing the images. The electron beam which transmits through the sample and the copper grid strikes the fluorescent or photographic screen and produces an image of the specimen which is visualized by means of a sophisticated camera. The transmitted central beam consisting of unscattered electrons gives rise to "bright-field" image while the scattered non-central electrons produce the "dark-field" image. These images collectively contain useful structural information involving the morphology and crystal structure of the sample. A JEOL-2010 FasTEM transmission electron microscope operated at 200 kV was used to capture high resolution images of our nanoparticles. Our main purpose of using TEM was to determine the shape, size and degree of polydispersity of our nanoparticles. From the high resolution TEM images better known as HRTEM, the spacing between the atomic planes (of the order of few angstroms) in crystalline nanoparticle samples was also estimated. Like SEM, a TEM also comes with EDS option for elemental analysis.

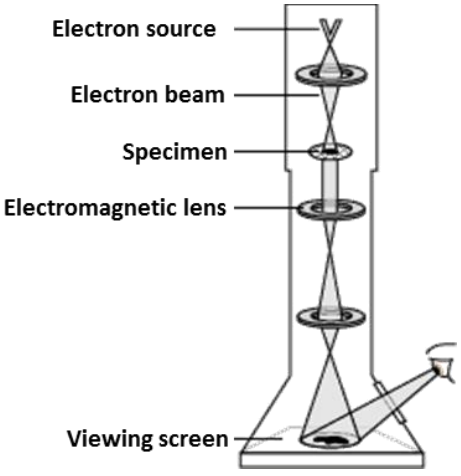

Figure 2.5 Schematic of a TEM (image courtesy of nobelprize.org)

2.5 DYNAMIC LIGHT SCATTERING (DLS) & ZETA POTENTIAL

DLS provides the hydrodynamic size and size distribution of particles undergoing Brownian motion in liquid suspensions. When a monochromatic beam of light, usually from a laser source, hits the particles in solution, there is a time-dependent fluctuation in the scattering intensity due to the random motion of the particles. An autocorrelation analysis of these intensity fluctuations provides information regarding the diffusion coefficient (*D*). Finally, an estimation of the hydrodymic size or diameter (d_H) can be obtained with the aid of Stokes-Einstein relation given by

$$d_H = \frac{k_B T}{3\pi\eta D} \tag{2.3}$$

where, k_B is the Boltzmann constant, η is the viscocity of the medium and T is the absolute temperature. The *hydrodynamic size* is defined as the diameter of a sphere in the same medium having an identical diffusion coefficient as that of the particle.

The zeta potential (ζ) measurements were also conducted to determine the stability of our nanoparticle dispersions. The zeta potential is defined as the electrokinetic potential difference between the particle surface and the dispersing medium. The ionic concentration of the medium and the pH are crucial factors for defining the zeta potential. A large magnitude of ζ , usually $|\zeta| > 40$ mV, implies the existence of strong electrostatic charges on the surface of the particles. These similar charges repel one another and prevent aggregation or clustering of the particles, and thereby remain well suspended inside the solution. We have used a Nano ZS90, Malvern Instruments for estimating the hydrodynamic size distribution and zeta potentials for our nanoparticle samples. The concentration of the nanoparticle dispersions used for DLS and zeta potential measurements were usually between 50-100 μg/ml.

2.6 PHYSICAL PROPERTY MEASUREMENT SYSTEM (PPMS)

The PPMS is used to record magnetization (*dc* and *ac*), heat capacity, electro-transport and thermal transport of the concerned sample. The Quantum Design PPMS (Model 6000) used for characterizing our nanoparticle samples have the following specifications:

1. Magnetic Field Range: -9T to +9T
2. Temperature Range: 1.8-400 K
3. AC Frequency Range: 10 Hz to 10 kHz
4. AC Field Amplitude Range: 2 mOe to 15 Oe
5. Sensitivity of DC magnetization measurements: 2.5×10^{-5} emu
6. Sensitivity of AC susceptibility measurements: 2×10^{-8} emu

Approximately, 20-30 mg of the nanoparticle sample was placed in a gelatin capsule packed with cotton (cotton restricts the motion of the sample) and mounted in a straw with proper stitching for performing the *magnetic* measurements in a PPMS.

dc Magnetometer & *ac* susceptometer

When a constant field is applied in the measurement region in case of *dc* magnetic measurements, the sample rapidly travels through both sets of detection coils (figure 2.6) causing a change in the magnetic flux. Hence, following Faraday's law, signals get induced in these detection coils. During the *ac* measurements, when an alternating field is applied in the measurement region, the sample is moved to the center of each detection coil. These coils basically detect any change in the applied *ac* field amplitude due to the presence of the sample.

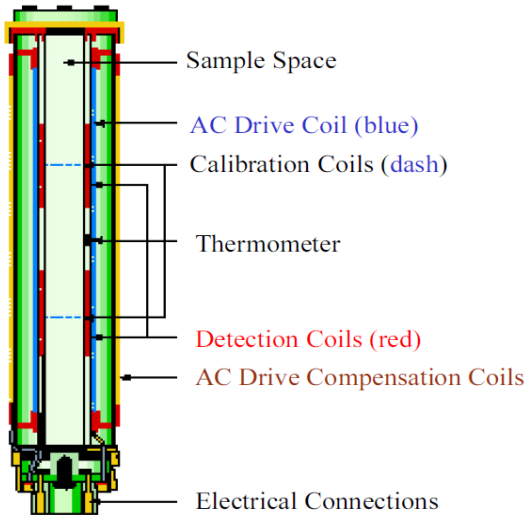

Figure 2.6 ACMS coil set of PPMS (image courtesy of Quantum Design)

We use the *dc* extraction technique to determine saturation magnetization for our nanoparticle samples from the magnetization (M) *vs* applied field (H) plots. From the *ac* susceptibility measurements, frequency dependent peaks are observed in χ' *vs* T and χ'' *vs* T plots to analyze superparamagnetic blocking or spin-glass like freezing in nanoparticles. The frequency independent features in these plots are marked by phase transitions, especially from ferri/ferro/antiferromagnetic to a paramagnetic phase. The *ac* magnetic susceptibility can be written as

$$\chi_{ac} = \chi' - i\chi'' \tag{2.4}$$

where, χ' and χ'' are the real and imaginary parts of the susceptibility. Following the Debye relaxation model [70] they can be expressed as

$$\chi' = \frac{\chi_o}{1+(\omega\tau)^2} \tag{2.5}$$

$$\chi'' = \frac{\chi_o \omega\tau}{1+(\omega\tau)^2} \tag{2.6}$$

Here, χ_o, ω and τ are the *dc* magnetic susceptibility, angular frequency and relaxation time of the particles. It can be inferred from the above equations that $\chi/$ increases with a decrease in frequency *f* of the applied *ac* field while $\chi//$ peaks at $\omega\tau = 1$, where $\omega = 2\pi f$.

2.7 MAGNETIC HYPERTHERMIA MEASUREMENTS

The experimental set-up of a typical MHT system is shown in figure 2.7. The MHT measurements were conducted by using an Ambrell Easy Heat station coupled with a simple solenoid. This set-up creates an oscillating magnetic field of a specific amplitude and frequency which raises the temperature of the ferrofluid positioned inside the solenoid. The ferrofluid is provided with an insulation cover to prevent heat exchange with the surroundings. The temperature (T) rise with time (t) is recorded with the aid of a thermometer. The slope of T *vs* t curve provides an essential parameter for estimating the SAR of the concerned ferrofluid. The current passing through the circuit gives estimation on the amplitude of the magnetic field while the values of L and C determine the magnitude of the frequency. All our measurements had been recorded at a frequency of 375 kHz and under an *ac* magnetic field amplitude of 235 Oe.

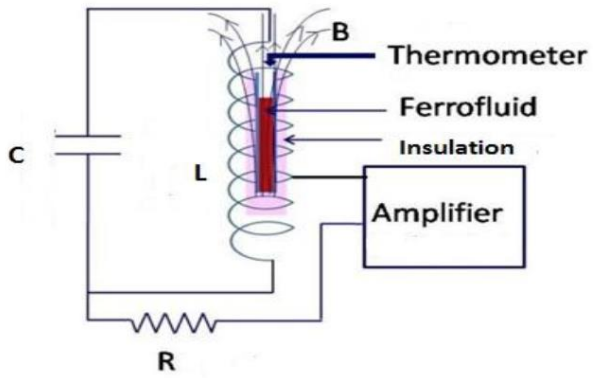

Figure 2.7 Schematic of a typical MHT system [70]

CHAPTER 3

STRUCTURAL ORIGIN FOR LOW-TEMPERATURE RELAXATION FEATURES IN DOPED Fe_3O_4 NANOPARTICLES

3.1 INTRODUCTION

Fe_3O_4 Nanoparticles

Fe_3O_4 has an inverse spinel crystal structure. The tetrahedral sites are occupied only by the Fe^{3+} ions while the octahedral positions have been occupied by alternating Fe^{3+} and Fe^{2+} ions as shown in figure 3.1 [71]. Fe_3O_4 nanoparticles (usually less than 20 nm) are superparamagnetic at the room temperature. These nanoparticles have applications ranging from magnetic recording to cancer research. These nanoparticles are extensively used as contrast agents for magnetic resonance imaging (MRI), used to target tumors inside the body and can also be utilized to treat cancer via hyperthermia [72]. The M_s value for bulk Fe_3O_4 is 92 emu/g [73] whereas the M_s value of 12 nm Fe_3O_4 nanoparticles is typically about 2/3 as large [61].

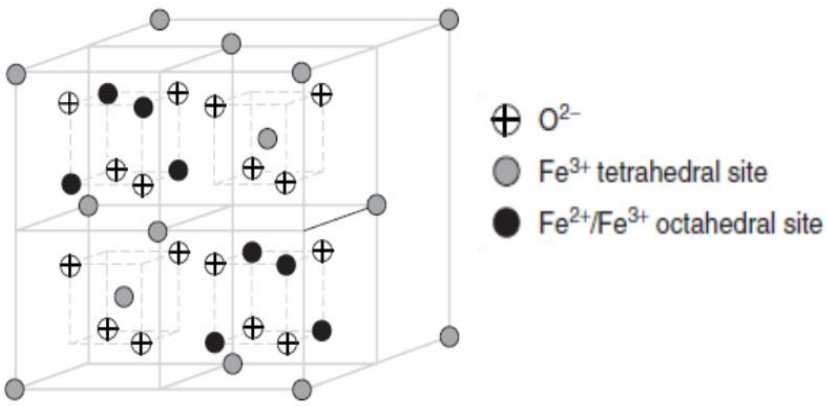

Figure 3.1 Inverse spinel structure of Fe_3O_4 with Fe^{3+} ions occupying the tetrahedral sites and Fe^{2+}/Fe^{3+} ions occupying the octahedral sites alternatively [71].

In addition to features attributed to superparamagnetic relaxation, nanoparticles can also exhibit magnetic relaxation effects at lower temperatures. Disordered surface spins have been

proposed as one possible origin for this relaxation. Sufficiently small particles, having very large surface to volume ratios, typically exhibit surface structural disorder [34, 36]. This structural disorder can induce spin disorder. This in turn may result in glassy magnetic behavior at low temperatures, which can be observed in nanoparticles addition to the higher-temperature superparamagnetic relaxation [32]. The freezing of the disorder-induced spins on the surface of a nanoparticle, typically referred to as "surface spin-glass freezing" [32], is widely observed, including studies by Peddis *et al.*[37] in $CoFe_2O_4$ nanopartcles, Winkler *et al.*[36] in NiO nanoparticles, Nadeem *et al.*[32] , Kodama *et al.*[35] and Tackett *et al.* [74] in $NiFe_2O_4$ nanoparticles. The model proposed by Kodama *et al.* considers a ferrimagnetic core of ordered spins surrounded by a shell consisting of spins having random orientations [35]. In this model, the glassy behavior is a single particle phenomenon in which the disordered surface spins produce the relaxation. Doping nanoparticles can also give rise to magnetic relaxation by introducing additional structural disorder, which can modify the local magnetic structure leading to spin-glass-like relaxation [75, 76]. Recently, using Mössbauer studies, Burianova *et al.* [77] have observed surface spin effects when Lanthanum (La) was doped into $CoFe_2O_4$ nanoparticles. However, there are also suggestions that this low temperature relaxation could arise from weak interparticle interactions. This magnetic relaxation driven by interactions among nanoparticles has been referred to as "superspin glass-like freezing" and is observed by Suzuki *et al.*[78] in Fe_3O_4 nanoparticles. Because of the importance of magnetic oxides in a wide range of applications from magnetic storage to catalysis [79], it is crucial to understand the interplay between structural disorder, dopants and interactions in determining the low temperature relaxation in Fe_3O_4 nanoparticles.

While experimental observations of low temperature glassy behavior in magnetic nanoparticle systems is well established [32, 36, 74, 78] there are conflicting proposals for the mechanisms responsible for these effects. The goal of our study is to elucidate the materials properties underlying the glassy relaxation in magnetic nanoparticles by intentionally introducing disorder into the system. In the present work, we report the effect of doping on the low temperature magnetic properties of Fe_3O_4 nanoparticles. Metal ions including Co^{2+}, Gd^{3+} and La^{3+} along with non-metallic B^{3+} were doped into Fe_3O_4 nanoparticles to probe the characteristics leading to this low temperature glassy behavior in magnetic nanostructures.

3.2 EXPERIMENTAL PROCEDURE

Synthesis of Fe_3O_4 nanoparticles

An aqueous solution of $FeCl_3.6H_2O$ (10.8 g) and $FeCl_2.4H_2O$ (4.0 g) in a molar ratio of 2:1 were initially mixed in a beaker. 1M NH_4OH (500 ml) solution was then added drop wise to the mixture under continuous stirring. We initially obtained a brown precipitate which ultimately turned into black as the sample continued to oxidize. The solution was then washed with deionized water until it became neutral. The nanoparticle solution was then freeze-dried for several hours to get fine powders of Fe_3O_4.

Synthesis of B, Gd, La and Co doped Fe_3O_4 nanoparticles

The same procedure was used for preparing the doped Fe_3O_4 nanoparticles with a slight alteration in the molar ratio of the iron salts. For synthesizing 5 at% B–Fe_3O_4, Gd–Fe_3O_4 and La–Fe_3O_4 nanoparticles, aqueous solution of $FeCl_3 \cdot 6H_2O$, $FeCl_2 \cdot 4H_2O$ and the corresponding source material used for doping were mixed together in a molar ratio of 1.85 : 1.00 : 0.15, while the molar ratio changes to 2.00 : 0.85 : 0.15 for preparing 5 at% Co–Fe_3O_4 nanoparticles. The

final nanoparticle sample was black in all cases, indicating the formation of ferrite nanoparticles, with the exception of the La–Fe_3O_4 nanoparticles having a brownish hue, which may be associated with the presence of highly oxidized iron oxide nanoparticle impurity phase.

3.3 RESULTS AND DISCUSSION

3.3.1 X-ray diffraction

The X-ray diffraction (XRD) patterns for the Fe_3O_4, Co-Fe_3O_4, B-Fe_3O_4, La-Fe_3O_4 and Gd-Fe_3O_4 nanoparticles measured at room temperature are plotted in figure 3.2. The distinct diffraction peaks for the undoped sample can be indexed to the crystal structure for Fe_3O_4 (JCPDS card number: 85-1436), confirming the formation of single phase crystalline nanoparticles. The peaks for the doped samples match the XRD spectrum for undoped Fe_3O_4, so doping does not substantially modify the crystal structure of the nanoparticles. Cell refinement studies performed on the XRD spectra of these nanoparticles, having a cubic symmetry, reveal that doping has caused a contraction of the lattice. The lattice parameter for undoped Fe_3O_4 nanoparticles is 8.382 Å, which is consistent with the results reported by Huan *et al.* [80].The refined lattice parameters for Co-Fe_3O_4, B-Fe_3O_4, Gd-Fe_3O_4 and La-Fe_3O_4 nanoparticles are estimated to be close to 8.349 Å, 8.366 Å, 8.368 Å and 8.371 Å respectively. The absence of any additional peaks in the XRD spectra for Co-Fe_3O_4 and B-Fe_3O_4 confirms that these samples are also comprised of single phase crystalline nanoparticles. However, additional peaks in the rare-earth doped nanoparticles, indicated with arrows in figure 3.2, suggest the formation of α-FeOOH (goethite) phase (JCPDS card number: 81-0462) along with Fe_3O_4 nanocrystals. The formation of α-FeOOH during the preparation of iron oxide nanoparticles has been previously attributed to the alkalinity of the synthetic medium [79]. The broadening of the (311) peak in the

XRD spectrum of the La doped sample is due to the overlap of the diffraction peaks corresponding to both Fe_3O_4 and α-FeOOH lattices [79] (JCPDS card numbers: 85-1436 and 81-0462).

Fe_3O_4 has an inverse spinel crystal structure. The tetrahedral sites accommodate only Fe^{3+} ions while the octahedral sites are occupied by both Fe^{3+} and Fe^{2+} ions alternatively [71]. Previous studies on doping in spinels find that lanthanide ions (Gd^{3+} / La^{3+}) and Co^{2+} ions are likely to occupy the octahedral sites by replacing the Fe^{3+} and Fe^{2+} ions respectively [81-83]. Since the ionic radii of Gd^{3+} (0.0938 nm) and La^{3+} (0.106 nm) are much larger than that of Fe^{3+} (0.064 nm), these ions are expected to cause large structural defects than Co^{2+} ion (0.072 nm) which has an ionic size very close to Fe^{2+} ion (0.078 nm) [82, 84-86]. Smaller trivalent ions like Al^{3+} (0.051 nm) when doped into $CoFe_2O_4$ nanoparticles have a stronger affinity for occupying the octahedral sites by replacing the Fe^{3+} ions [87], which we also expect for B^{3+} ions (0.041 nm) [88].

The average crystallite size of the nanoparticles was estimated by the Debye Scherrer equation, as $d=0.9\lambda/\beta\cos\theta$, where d is the average diameter or size of the particle, λ is the X-ray wavelength and β is the full width at half maxima of the peak corresponding to the Bragg angle θ [89]. The (220), (311) and (400) peaks were used to calculate the average crystalline particle size for the cobalt, boron and gadolinium doped nanoparticles, as well as for the undoped nanoparticles. The mean crystallite size estimated for the Co-Fe_3O_4, B-Fe_3O_4 and Gd-Fe_3O_4 nanoparticles is approximately 14 nm, 13 nm and 23 nm respectively, compared to 12.5 nm for the undoped particles. Because the (311) peak for La doped nanoparticles is broadened, we used only the (220) peak for estimating the particle size which gave a diameter of approximately 22 nm. These XRD measurements suggest that while boron and cobalt substitution have a negligible

effect on the Fe_3O_4 nanoparticle size, rare earth doping increases the particle size roughly by a factor of two, for the given synthesis conditions. This means that while the surface to volume ratio for the B and Co doped nanoparticles is nearly unchanged, this *decreases* by approximately a factor of two for the La and Gd doped samples.

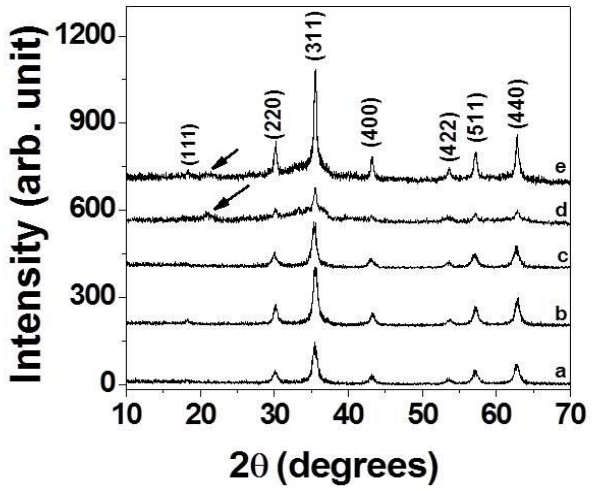

Figure 3.2 XRD spectra of (a) Fe_3O_4 (b) Co-Fe_3O_4 (c) B-Fe_3O_4 (d) La-Fe_3O_4 and (e) Gd-Fe_3O_4 nanoparticles. The curves have been offset vertically for clarity.

3.3.2 Transmission electron microscopy

We also used transmission electron microscopy (TEM) imaging to more fully parameterize the structure of the nanoparticles. Figure 3.3 shows TEM images of the B-Fe_3O_4 and Gd-Fe_3O_4 nanoparticles, together with high resolution images of both Gd and La substituted Fe_3O_4. The B-Fe_3O_4 nanoparticles (figure 3.3(a)) are roughly spherical with an average particle size 13-14 nm. This is very slightly larger than the size estimated from XRD, implying that there could be a thin amorphous layer on the surface of these nanoparticles. The TEM image for the Gd-Fe_3O_4 nanoparticles (figure 3.3(b)) show cubical or rhombohedral morphologies. This deviation from sphericity with gadolinium doping is similar to that reported by Drake *et al.* [89],

although they have not observed such a large change in nanoparticle size. However, for our nanoparticle sample, the increase in particle size suggested by XRD is confirmed by high resolution TEM (HRTEM) image, as illustrated in figure 3.3(c), which shows the formation of a crystalline Gd-Fe_3O_4 nanoparticle with slightly larger dimensions than those obtained from the XRD data. A HRTEM image for the La-Fe_3O_4 nanoparticles is also shown in figure 3.3(d) with the formation of crystal planes being clearly indicated by the encircled region. However, no significant defect sites or distortions in the crystal planes are located from these HRTEM images.

The larger particle size determined using TEM as compared to XRD can potentially be attributed to an amorphous surface layer, as the XRD peak width reflects only the crystalline component. The saturation magnetization of nanoparticles is routinely found to be smaller than in bulk materials (on the order of 68 emu/g for nanoparticles compared to 92 emu/g [90] in bulk for Fe_3O_4), which is typically associated with a non-magnetic surface layer. The proposed structural amorphous layer and magnetically amorphous layer need not overlap, since a material can be structurally ordered but magnetically disordered. The possible presence of this magnetically disordered layer could be relevant for understanding the enhanced low temperature magnetic relaxation in certain nanoparticles.

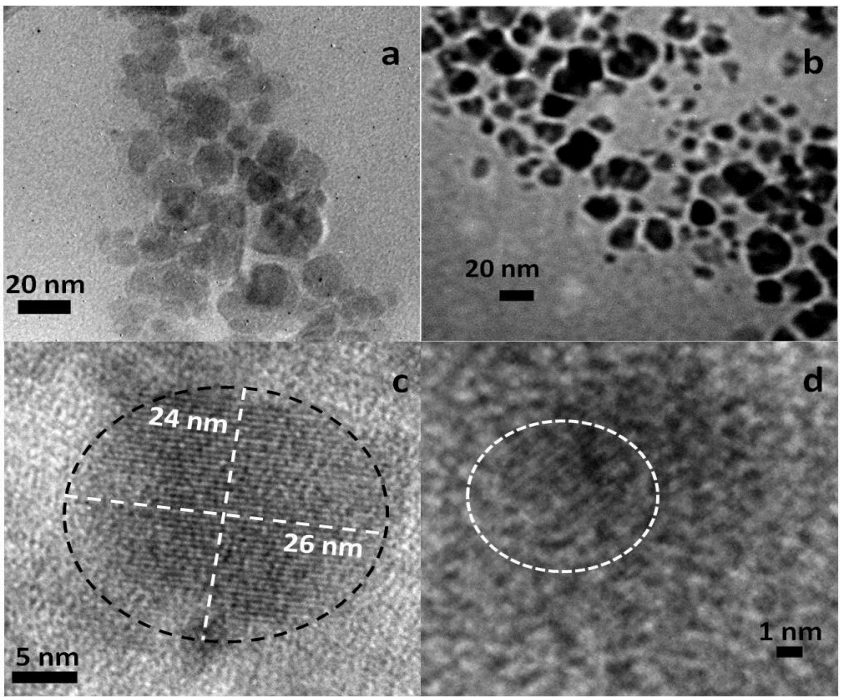

Figure 3.3 TEM images of (a) B-Fe_3O_4 and (b) Gd-Fe_3O_4 nanoparticles, HRTEM images of (c) Gd-Fe_3O_4 and (d) La-Fe_3O_4 nanoparticles.

3.3.3 Raman spectroscopy

We have also used Raman spectroscopy to investigate the local structural properties of the nanoparticles, and more carefully probe for non-crystalline secondary phases, which would not be observed in XRD studies. Figure 3.4 plots the Raman spectra for the B-Fe_3O_4, Gd-Fe_3O_4 and La-Fe_3O_4 nanoparticles. Mandal *et al*. [73] reported the presence of distinct peaks at 211, 283, 490 and 682 cm^{-1} for undoped Fe_3O_4 nanoparticles, which correspond to the T_{2g}, E_g, T_{2g} and A_{1g} modes respectively, while the peak corresponding to 390 cm^{-1} was associated with a magnon excitation. However, the interpretation of these peaks is ambiguous. Features near these frequencies have been assigned to α-FeOOH in Raman measurements reported by Legodi *et al.* [91]. Since our XRD data unambiguously identifies the presence of α-FeOOH in the rare-earth doped nanoparticles, we attribute the peaks at 219, 278, 388, 485 and 578 cm^{-1} in figure 3.4 to the presence of a goethite impurity phase in all the samples, even those appearing phase pure in

the XRD measurements. Bulk α-FeOOH is antiferromagnetic with Neel temperature, T_N=393 K, but nanoparticles can show a non-zero magnetic moment, [1] so this impurity phase could possibly affect the magnetic response of the nanoparticles. According to studies by Ni *et al.* [92], the peak observed at 667 cm^{-1} in spectrum (a) of figure 3.4 for the B-Fe_3O_4 nanoparticle sample is attributed to the A_{1g} mode in Fe_3O_4, which is shifted to even smaller wavenumbers, close to 650 cm^{-1}, on rare-earth doping as seen from spectra (b) and (c). The shift to lower energies may arise from substituting the more massive rare-earth ions into the lattice, which will decrease the frequency of metal-oxygen vibrations. These Raman measurements clearly identify the presence of some impurity phases in the nanoparticles, including those that are XRD clean, and other structural defects in the doped samples.

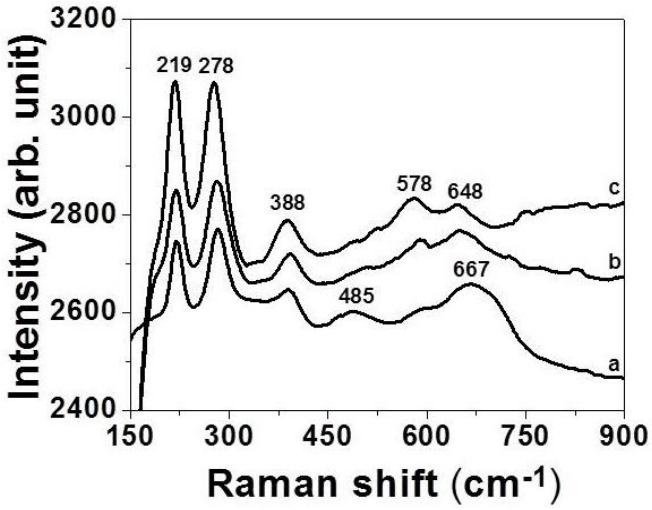

Figure 3.4 Raman spectra of (a) B-Fe_3O_4 (b) Gd-Fe_3O_4 and (c) La-Fe_3O_4 nanoparticles. The curves have been offset vertically for clarity.

Energy Dispersive Spectroscopy (EDS) measurements (not shown) confirm that approximately 5.4, 8.2 and 5.7 at. % of Co^{2+}, Gd^{3+} and La^{3+} had been incorporated into the Fe_3O_4 nanoparticles during the synthesis process. While EDS is only appropriate for semi-quantitative

analysis, these values are roughly consistent with the nominal initial doping percentage (5 at. %). Since EDS is unable to detect the presence of very light elements, including boron, we used ICP-OES to estimate the boron content in our nanoparticle sample. The B-Fe_3O_4 nanoparticles, having a nominal B composition of 5 at.%, was dissolved in a weak nitric acid solution for the analysis. The ICP-OES data (not shown) reveal that approximately 2.5 at.% of B has been incorporated into the Fe_3O_4 nanoparticles. This B fraction is smaller than the initial doping percentage (5 at.%). The loss of boron may be attributed to its high volatility, as studies have found that a very small percentage of boron can get vaporized from a solution of H_3BO_3 in water [93].

3.3.4 Magnetic measurements

Figure 3.5 shows M *vs* H plots for the undoped, boron doped, cobalt doped and gadolinium doped Fe_3O_4 nanoparticles at room temperature. The saturation magnetization (M_s) values obtained for the undoped (M_s=68 emu/g), boron doped (M_s=66.5 emu/g) and cobalt doped (M_s=66 emu/g) Fe_3O_4 nanoparticles are identical within experimental uncertainties (+/-1 emu/g, coming mainly from the uncertainty in measuring the sample mass). Conversely, the M_s value obtained for Gd-Fe_3O_4 nanoparticles is close to 24 emu/g, a decrease by roughly 65 % compared to the undoped nanoparticles. This substantial decrease in saturation magnetization for Gd-Fe_3O_4 nanoparticles is consistent with the value reported by Liang *et al.*[79], although this work does not provide the specific doping fraction and so a direct comparison is not possible. With doping less than 1 at. %, Drake *et al.* have reported that the M_s value for Gd-Fe_3O_4 nanoparticles was unchanged [89]. The saturation magnetization of Fe_3O_4 nanoparticles on rare earth doping appears to depend very strongly on the doping fraction. This speculation is supported by results

from Huan *et al*. [80] who found that saturation magnetization strongly suppresses in lanthanide-doped (Eu and Sm) Fe_3O_4 nanoparticles, decreasing roughly by a factor of 2 to 3 at10% doping.

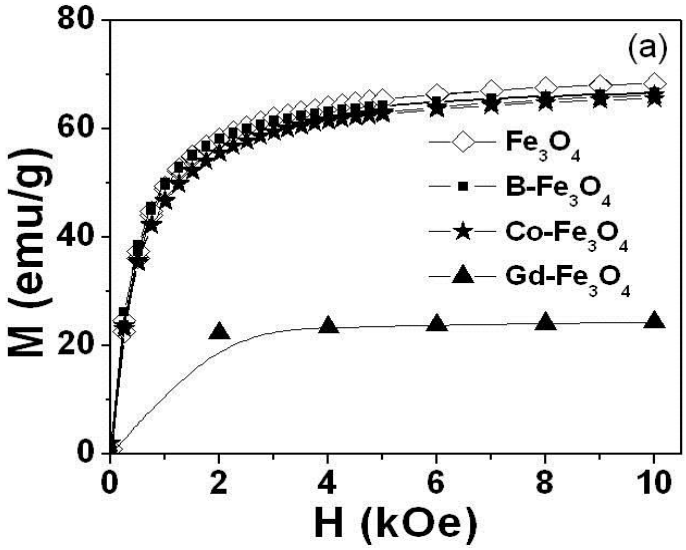

Figure 3.5 M *vs* H plots for Fe_3O_4, B-Fe_3O_4, Co-Fe_3O_4 and Gd-Fe_3O_4 nanoparticles at room temperature.

Figure 3.6 shows χ''/χ' (10K) *vs* T for the Fe_3O_4, Co-Fe_3O_4, Gd-Fe_3O_4, La-Fe_3O_4 and B-Fe_3O_4 nanoparticles at low temperatures using a fixed excitation frequency of 10 kHz under an excitation field of 10 Oe. The susceptibilities were scaled to the value at 10 K to allow a direct comparison between the results for the different samples. For the boron, gadolinium and lanthanum doped samples, large and pronounced peaks in the magnetic dissipation are seen near 35 K. These peaks indicate the onset of low temperature relaxation, typically associated with a glassy magnetic response [32, 36, 74, 78]. Similar features, but having much smaller amplitudes, are observed for both the undoped and cobalt doped Fe_3O_4 nanoparticles. Therefore, while doping with B^{3+}, Gd^{3+} and La^{3+} has produced a significant enhancement in the low temperature magnetic relaxation in Fe_3O_4 nanoparticles, this relaxation is still present in the undoped parent compound and also in the Co^{2+} doped nanoparticles, so the magnetic dissipation is not produced

solely by presence of these dopants. The inset in figure 3.6 shows the χ''/χ' (10K) *vs* T graph for a different set of Fe_3O_4 and B-Fe_3O_4 nanoparticle samples clearly depicting the low temperature magnetic features and also the superparamagnetic blocking near 200 K. We do not see any significant shift in the superparamagnetic relaxation temperature (T_B) in these doped nanoparticles. Since the particle sizes for the undoped and boron doped nanoparticles are roughly fixed, we presume that the magnetocrystalline anisotropy is not changed substantially for small doping levels. This is consistent with previous studies performed on Co doped Fe_3O_4 nanoparticles [94].

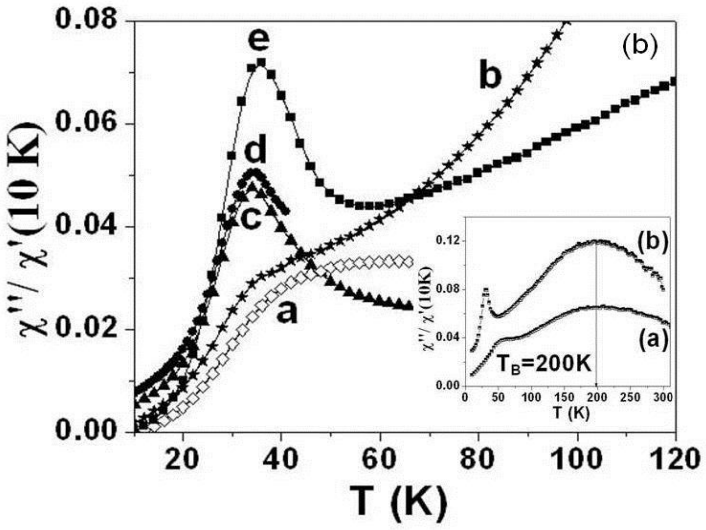

Figure 3.6 χ''/χ'(10K) *vs* Temperature (T) graph for (a) Fe_3O_4, (b) Co-Fe_3O_4, (c) Gd-Fe_3O_4, (d) La-Fe_3O_4 and (e)B-Fe_3O_4 nanoparticles at a specific excitation frequency of 10kHz under an excitation field of 10 Oe. The inset shows the χ''/χ'(10K) *vs* Temperature (T) graph for a different set of (a) Fe_3O_4 and (b)B-Fe_3O_4 nanoparticles at a specific excitation frequency of 1kHz under an excitation field of 10 Oe. The curves in the inset have been offset vertically for clarity.

We now consider a possible origin for this magnetic relaxation, consistent with the large enhancement found with B, Gd and La doping. The amplitude of the magnetic relaxation in both the boron and rare-earth doped nanoparticle samples increases by roughly a factor of three above

the undoped particles. This increase cannot be attributed to defect spins developing simply because of an increase in the surface to volume ratio, as these doped nanoparticles are of the same size or larger than the undoped particles. Motivated by the fact that there is a significant increase in the dissipation on B, Gd and La doping, which can produce structural defects, but not with Co substitution, which has roughly the same ionic radius as Fe^{2+}, we suppose that structural defects rather than dopant magnetic moments are responsible for this low temperature relaxation.

Because the susceptibility peaks in the doped and undoped samples plotted in figure 3.6 are qualitatively similar, falling at nearly the same temperature, the magnetic relaxation must not be sensitive to the specific nature of the structural defect, whether arising from an impurity dopant, or as an intrinsic defect. To more carefully parameterize the low temperature magnetic properties in the different nanoparticle samples, we have analyzed the temperature and frequency dependence of the relaxation by fitting to a thermally activated process. Figure 3.7(a) shows ln τ *vs* (1/T) plot for the undoped Fe_3O_4 nanoparticles. This curve is approximately linear, and can be fit to an Arrhenius equation with the activation energy E_A/k_B being equal to 570 K and a characteristic relaxation time of $\tau_0 \sim 10^{-9}$s. Similar fits in to the data in Figures 3.7(b) and 3.7(c) yield the values of τ_0 in the range of $\sim 10^{-11}$s to 10^{-12} s for B-Fe_3O_4 and Gd-Fe_3O_4 nanoparticles respectively with activation energies close to E_A/k_B = 500 K. There is some change in the microscopic time constant τ_0 for the relaxation for these different samples, but these are within approximately one order of magnitude, and the activation energy changes only slightly (by roughly 10%) on doping. The relaxation data presented in figure 3.7 therefore suggest that the relaxation mechanism giving rise to the peaks in the low temperature susceptibility is unchanged on doping. These quantitative similarities in the relaxation dynamics suggest that the magnetic degrees of freedom relaxing in the doped samples are the same, or similar, to the relaxing

moments in the undoped nanoparticles. This is consistent with the Mössbauer measurements reported by Burianova *et al.*[77] where they observe that the doping of La into $CoFe_2O_4$ nanoparticles gives a significant spin canting of only the Fe^{3+} ions. In this context, doping has produced additional structural defects in the nanoparticles leading to an increase in the amplitude of relaxation. XPS studies performed on Co substituted Fe_3O_4 show a gradual shift of the Fe peaks to lower binding energies, as well as peak broadening, with increasing Co concentration, but do not clearly demonstrate any change in the Fe^{2+}/Fe^{3+} ratio (within the available resolution) [95]. The α-FeOOH impurity phases seen in Raman and XRD may also contribute to the magnetic properties of these nanoparticles. However, we attribute this low temperature relaxation to the intrinsic properties of Fe_3O_4 motivated by Mössbauer studies on the La doped nanoparticles.

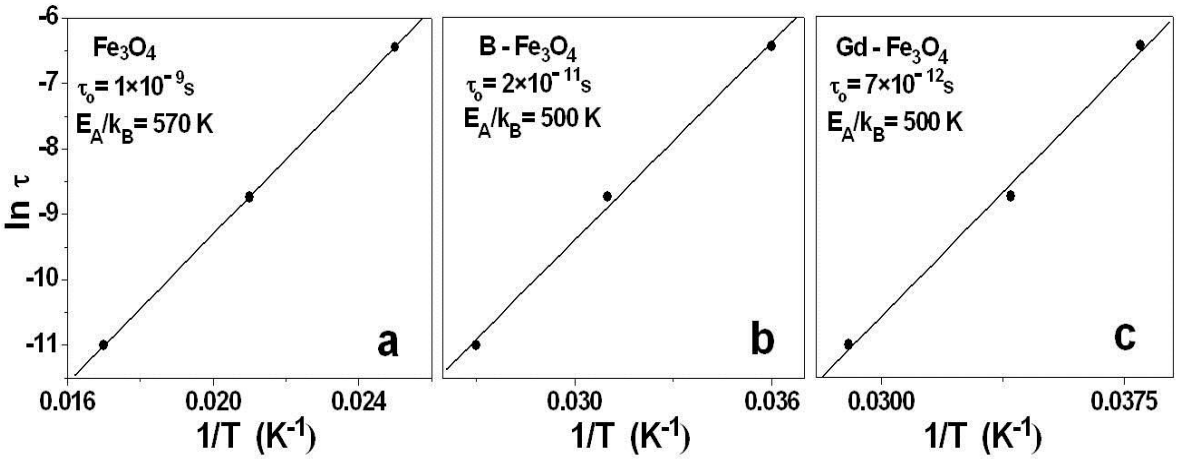

Figure 3.7 Arrhenius fits for (a) Fe_3O_4, (b) B-Fe_3O_4 and (c) Gd-Fe_3O_4 nanoparticles

We have observed that the surface to volume ratio is roughly unchanged for the cobalt and boron doped nanoparticles as compared to the undoped nanoparticles, therefore, we argue that the *intrinsic* surface spin contribution (that is, the contribution arising from spins at the

surface of the nanoparticle) is similar. For the rare-earth doped nanoparticles, the nanoparticles are larger, hence the surface to volume ratio is smaller so the relative intrinsic surface disorder is smaller. For all of these systems, we argue that this low temperature magnetic relaxation arises predominantly from structural defects, whether introduced by the dopants or intrinsic to Fe_3O_4, rather than surface effects. In this context, we consider the α-FeOOH phase as a type of intrinsic disorder. This non-magnetic secondary phase may be stabilized by the dopants (as suggested in the XRD and Raman data) and could also contribute to the magnetic dissipation.

The areas under the relaxation peaks but above background are approximately proportional to the number of relaxing spins in the different samples. For the B-Fe_3O_4, Gd-Fe_3O_4 and La-Fe_3O_4 nanoparticles, these areas are a factor of 1.5 to 2 greater than for the undoped Fe_3O_4 sample. If each B^{3+}, Gd^{3+} and La^{3+} dopant ion produces a distortion leading to a moment participating in the relaxation in the cell in which it is located along with the nearest neighbors, a single dopant will affect 7 cells. Making the simplifying assumption that the dopants are distributed uniformly, as opposed to randomly, this means that at 5% doping, approximately 35% of the unit cells have moments contributing to the magnetic relaxation near 35 K. Since the number of relaxing spins for B, Gd and La doped particles is twice as large as for Fe_3O_4 nanoparticles, we argue that the concentration of defects should also be twice as large. This would give a concentration of defects for undoped Fe_3O_4 nanoparticles of approximately 15% of the unit cells. This increased fraction of unit cells having a structural distortion even in undoped Fe_3O_4 nanoparticles can readily be attributed to the very large surface to volume ratio in these materials. For a Fe_3O_4 nanoparticle having a diameter of 12.5 nm, over 30 % of the unit cells are at the surface of the particle, and thus may be expected to show some structural defects. We speculate that for the pure Fe_3O_4 nanoparticles the majority of the disordered spins may be near

the magnetic amorphous layer. However, for the B-doped nanoparticles we argue that the structural defects are distributed throughout the volume of the nanoparticles. This is because the saturation magnetization (M_s) value for the B doped sample is close to undoped Fe_3O_4, which implies that the magnetically amorphous layer has approximately the same thickness.

We argue that this low temperature relaxation is not greatly influenced by interparticle interactions, but rather arises from single-particle effects. This argument is based on the observation that dipolar interactions, generally the most prominent interactions for magnetic nanoparticles[33], do not differ significantly among these different samples. This can be observed directly for the Co and B doped samples, where the particle size and saturation magnetization are practically unchanged. In this case, the dipolar interactions between nanoparticles will also be fixed as the morphology is unchanged. This means that the strong enhancement in the low temperature relaxation should be attributed to single particle effects. For the rare-earth doped nanoparticles, the size is almost doubled while the saturation magnetization decreases by roughly a factor of three when compared to Fe_3O_4 nanoparticles. Therefore, the dipolar interaction energy, which varies like μ^2/r^3,[33] is also approximately unchanged. The dramatic increase in the amplitude of the low temperature magnetic relaxation anomaly in some of these nanoparticle samples, without any substantial change in the dipolar interactions, argues that the relaxation arises from single particle effects.

3.4 CONCLUSIONS

The incorporation of Gd^{3+}, B^{3+} and La^{3+} dopants into Fe_3O_4 nanoparticles have significantly enhanced the amplitude of the low temperature glassy relaxation in this system, contrary to doping with cobalt, which does not measurably affect the relaxation. The fact that

there is no significant difference in properties on doping with magnetic Gd^{3+} and non-magnetic B^{3+} or La^{3+} suggest that structural, rather than magnetic, defects play a major role in modifying the relaxation. This study strongly suggests that the low temperature magnetic relaxation observed in undoped nanoparticles arises from single-nanoparticle effects due to freezing of local moments associated with structural defects, including surface spins, rather than being driven by any weak interaction among different nanoparticles. In this context, we suggest that all structural defects, and not just surface spins, are responsible for the low-temperature glass like relaxation observed in many magnetic nanoparticles. This substantial defect-induced relaxation in nanostructures may have important implications for the design of high Q nanomagnetic devices.

CHAPTER 4

INVESTIGATING INTERACTIONS IN γ-Fe_2O_3 AND Fe_3O_4 NANOPARTICLE SYSTEMS

4.1 INTRODUCTION

Recent advances in materials synthesis and preparation have made the development and investigation of nanoscale magnetic systems widely accessible. This has led to proposals for incorporating nanoscopic magnets in applications ranging from magnetic recording [96] to targeted drug delivery [18]. While the general behaviour of these systems is well understood in the context of the Néel-Brown model for single particle magnetic relaxation [29], developing a complete model for the behavior of a collection of interacting nanoscale magnets is an active topic of current research. In the non-interacting Néel-Brown model, the magnetic moments of each nanoparticle undergo thermally assisted transitions between the easy crystallographic directions. This leads to a temperature dependent relaxation time for the nanoparticle magnetization given by an Arrhenius equation, $\tau = \tau_0 \exp(E_A/k_BT)$, where τ_0 is a microscopic time scale for the transitions, which typically lies between 10^{-9} -10^{-13} s for these non-interacting sysems [24, 61]. In this model, the energy barrier E_A is KV, where K and V are the magneto-crystalline anisotropy constant and volume of the nanoparticle respectively [24, 61]. The blocking temperature (T_B) for the system is the experimental temperature at which the zero-field cooled magnetization exhibits a peak and is generally proportional to the energy barrier KV [2, 97].

It is predicted that with increasing interactions, magnetic nanoparticles may develop a spin-glass state [98]. Experiments on concentrated and diluted nanoparticle samples have found evidence for a change in properties characterized by glassy behavior to properties associated

with superparamagnetic interactions with decreasing particle concentrations [98, 99]. In the case of dipolar interactions between nanoparticles, the two-particle dipolar energy is given by: $E_d \approx (2\mu_0/4\pi)(\mu^2/\alpha^3)$, where μ and a are the total nanoparticle moment and the interparticle spacing respectively [100]. Experimentally, decreasing the spacing between iron oxide nanoparticles is found to shift T_B to higher temperatures, as observed in studies on iron oxide nanoparticles in porous silicon [101], in Langmuir-Blodgett films [100, 102], and with the particle spacing controlled by dendrimer coatings [103]. For dipolar interactions observed in monodisperse Fe_3O_4 nanoparticles suspended in organic solvents, Bae *et al.* [33] have reported a gradual drop in the blocking temperature following an increase in the interparticle distance, although T_B tends to saturate for much larger particle spacings. Studies on γ-Fe_2O_3 nanoparticles have also found an increase in the blocking temperature T_B (or the energy barrier E_A) with increasing particle concentrations [104] following a theoretical model proposed by Dormann *et al.* [105]. However, attempting to parameterize interaction effects through a shift in the blocking temperature requires preparing an additional diluted sample to determine the non-interacting value of T_B. Pal *et al.* [106] have also shown that coating of gold onto the surface of Fe_3O_4 nanoparticles could potentially affect interparticle interactions.

Interaction effects can also be investigated by measuring the *ac* magnetic susceptibility, which exhibits an anomaly when the measurement frequency f is commensurate with the nanoparticle relaxation time. The dimensionless frequency dependent temperature shift, defined as $\alpha = \Delta T/[T\Delta\log_{10}(f)]$, where ΔT is the difference in the peak temperatures corresponding to two different frequencies and T being the average between those temperatures, is often used to estimate the relative importance of interactions, with larger values of α, typically above 0.13, being indicative of a non-interacting system, between 0.05 and 0.13, corresponds to medium or

weakly interacting systems, and smaller values, less than 0.05, associated with strong or glassy interactions [24]. Experimentally, the frequency dependent relaxation in weakly interacting systems is typically fit to a *phenomenological* Vogel-Fulcher law, $\tau = \tau_0 \exp [E_A/k_B (T-T_o)]$ [24] , which differs from the Arrhenius expression by the effective interaction energy T_0. Using the frequency dependent relaxation allows interaction effects to be estimated by measurements on a single sample, without the need to determine the non-interacting value of T_B, at the cost of measuring the response at a number of different frequencies. In this work, we present results on interparticle interactions in both γ-Fe_2O_3 and Fe_3O_4 magnetic nanoparticles using *ac* susceptibility measurements.

4.2 EXPERIMENTAL PROCEDURE

The maghemite (γ-Fe_2O_3) nanoparticles were prepared using eight iterations of a matrix-mediated precipitation reaction [107]. The synthesis was carried out by cross-linking sodium alginate with Fe^{2+} ions in a methanol-water solution. The Fe_3O_4 nanoparticles were prepared using a chemical co-precipitation technique [61]. Both nanoparticle samples were lypholized into powders for the structural and magnetic studies. The structures of the samples were measured using x-ray diffraction (XRD) (Rigaku MiniFlex 600 X-ray diffractometer), and transmission electron microscopy (JEOL FasTEM 2010 HR). The *ac* magnetization studies on these nanoparticles were conducted using the *acms* option on a Quantum Design Physical Property Measurement System (PPMS).

4.3 RESULTS AND DISCUSSION

4.3.1 X-ray diffraction & Transmission electron microscopy

We plot the x-ray diffraction pattern for the Fe_3O_4 nanoparticles in figure 4.1 (a). The graph shows the peaks expected for Fe_3O_4 (JCPDS card number: 85-1436), with no additional reflections, indicating the absence of any significant crystalline impurity phases. Using the Debye-Scherrer equation [61], we estimated the average coherent domain size [108] of Fe_3O_4 to be nearly 12 nm. The transmission electron microscope images for γ-Fe_2O_3 and Fe_3O_4 nanoparticles are shown in figures 4.1 (b) and 4.1 (c) respectively. These show nearly spherical particles having diameters of approximately 6 nm (γ-Fe_2O_3) and 12 nm (Fe_3O_4), albeit with a relatively large degree of polydispersity. Because the samples were dissolved in alcohol and then deposited on a carbon coated copper grid for imaging, the particle distribution in these images may be different from the nanoparticle distribution during the magnetic measurements. With this caveat, we note that the γ-Fe_2O_3 nanoparticles are more widely separated than the Fe_3O_4 nanoparticles, as expected for particles distributed in the alginate matrix.

4.3.2 Magnetic measurements

We plot the out-of-phase component of the magnetic susceptibility, χ'', corresponding to the loss component, as a function of temperature (T) at several different frequencies for γ -Fe_2O_3 and Fe_3O_4 nanoparticles in figures 4.2(a) and 4.2(b) respectively. These measurements were done with an excitation field of 10 Oe in the absence of any applied *dc* field. The peak in the χ'' *vs* T curve occurs when the temperature independent measurement frequency ω and the characteristic magnetic relaxation time τ satisfy the relation $\omega\tau$ =1. In the case that τ satisfies the Arrhenius equation, we expect to recover a straight line when ln τ is plotted as a function of 1/T,

with the slope and intercept of this curve giving the activation energy E_A and microscopic relaxation time τ_0 respectively. The Arrhenius fit for the γ -Fe_2O_3 nanoparticles yields $E_A/k_B \approx$ 2550 K and $\tau_0 \approx 10^{-18}$ s, while the fit for the Fe_3O_4 nanoparticles gives $E_A/k_B \approx 3100$ K and $\tau_0 \approx 10^{-12}$ s. The value for the characteristic relaxation time for the Fe_3O_4 nanoparticles is reasonable, but is unphysically short [109] for the γ -Fe_2O_3 particles. This strongly suggests that there are interactions present in the γ-Fe_2O_3 nanoparticle sample.

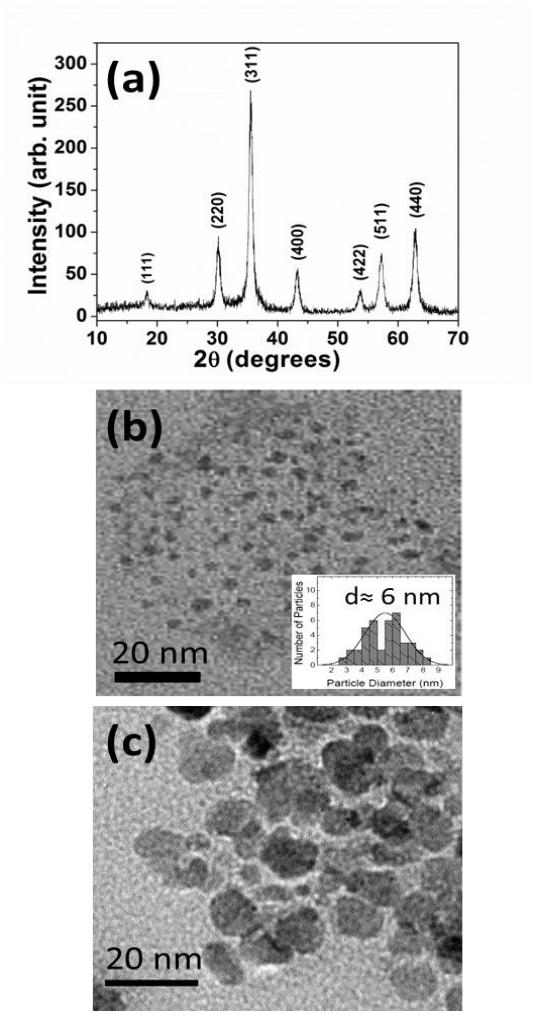

Figure 4.1 (a) XRD of Fe_3O_4 nanoparticles, TEM images of (b) γ -Fe_2O_3 and (c) Fe_3O_4 nanoparticles.

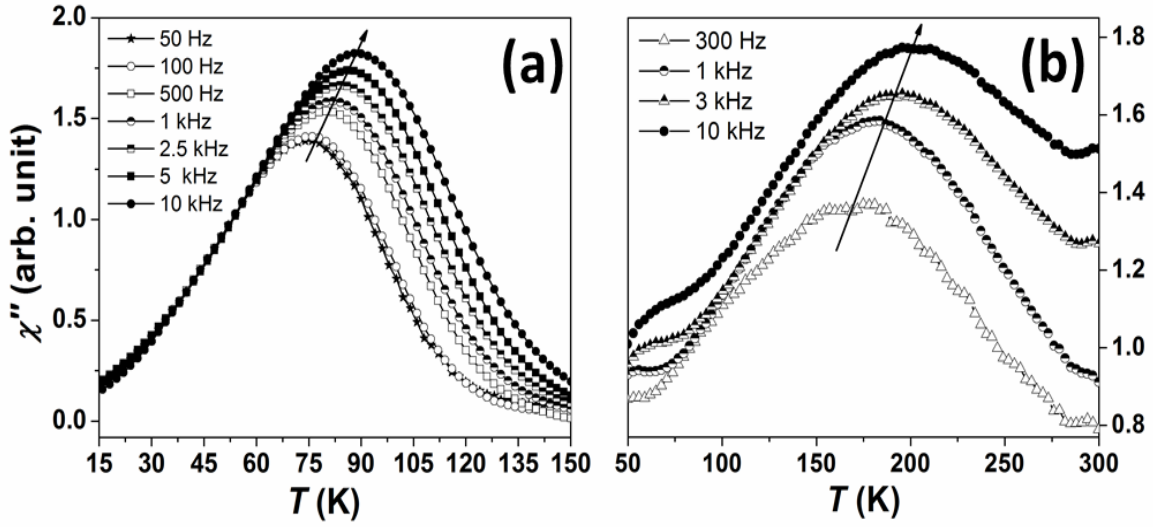

Figure 4.2 Out-of-phase component of the *ac* magnetic susceptibility (χ'') *vs* Temperature (T) plot for (a) γ-Fe_2O_3 nanoparticles in alginate matrix and (b) Fe_3O_4 nanoparticles at different frequencies under an excitation field of 10 Oe.

To more carefully explore the possible interactions in these nanoparticle systems, we fit the frequency and temperature dependent relaxation peaks for both samples to a Vogel-Fulcher equation, as shown in figures 4.3(a) and 4.3(b). We estimate the *dc* blocking temperature from the zero-frequency extrapolation of these curves as T_B=75 K for the γ -Fe_2O_3 nanoparticles and T_B=160 K for the Fe_3O_4 nanoparticles. The fitting parameters for γ -Fe_2O_3 are: $E_A/k_B \approx 350$ K, $\tau_0 \approx 10^{-9}$ s, and T_0=50 K, giving a ratio of T_0/T_B = 0.6. This ratio of the effective interaction and blocking temperature is consistent with moderate interactions (for surface spin glass features in nickel ferrite nanoparticles [97], T_0/T_B = 0.9). The best-fit parameters for Fe_3O_4 are: $E_A/k_B \approx 2350$ K, $\tau_0 \approx 10^{-11}$ s, and T_0=20 K, giving a ratio of T_0/T_B = 0.12, although a range of values for T_0 roughly between 0 K and 40 K give equally good fits. These results indicate that the γ-Fe_2O_3 nanoparticles are significantly more strongly interacting than the Fe_3O_4 nanoparticles. We also parameterized the interactions in terms of the dimensionless frequency shift α. We find that for γ

-Fe_2O_3 nanoparticles, $\alpha \approx 0.07$, indicative of a moderately interacting system, while for the Fe_3O_4 nanoparticles, $\alpha \approx 0.13$, corresponding to nearly non-interacting nanoparticles.

Assuming that the saturation magnetizations (M_s) of Fe_3O_4 and γ-Fe_2O_3 nanoparticles are approximately equal, as is the case for the bulk systems [61, 109], and the mean diameter (d) for Fe_3O_4 is twice as large as the γ-Fe_2O_3 nanoparticles suspended in the alginate matrix, we estimate $\mu(Fe_3O_4) \approx 8\mu(\gamma\text{-}Fe_2O_3)$, using the relation $\mu \sim M_s d^3$ [102]. The Fe_3O_4 nanoparticles are a single-phase powder, so we assume that the mean center-to-center interparticle spacing is roughly $1.5d(Fe_3O_4)$ supposing that the system is not close-packed. Conversely, the γ -Fe_2O_3 nanoparticles are non-uniformly distributed in the alginate matrix, with the volume of nanoparticles being roughly half the total volume as determined by measurements of the saturation magnetization for the composite (not shown). We therefore suppose that the mean spacing between γ-Fe_2O_3 nanoparticles is closer to $2d$ (γ-Fe_2O_3). As the Fe_3O_4 nanoparticles have a diameter twice as large as the γ-Fe_2O_3 nanoparticles, we finally estimate that the center-to-center mean spacing (a) between the Fe_3O_4 nanoparticles to be very roughly 1.5 times larger than between γ-Fe_2O_3 nanoparticles.

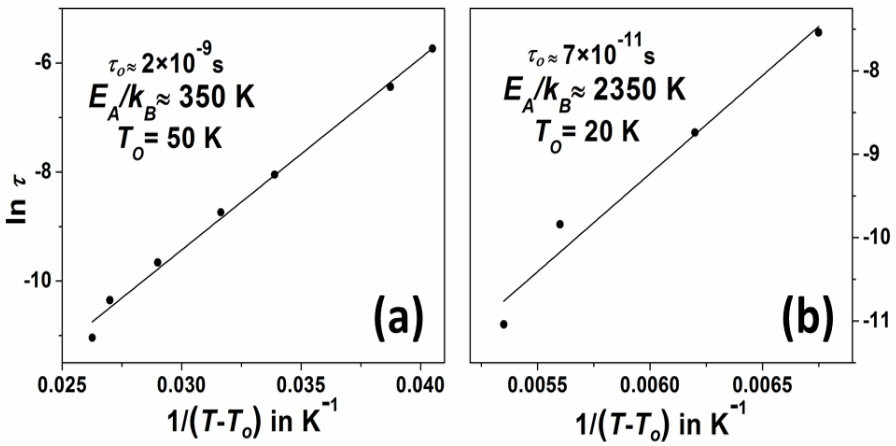

Figure 4.3 Vogel-Fulcher fits for (a) γ-Fe_2O_3 nanoparticles in alginate matrix and (b) Fe_3O_4 nanoparticles.

Using these values, the dipolar interaction energy, proportional to μ^2/a^3 [102], is approximately 20 times larger for the Fe_3O_4 nanoparticle ensemble as compared to the γ-Fe_2O_3 nanoparticles. This analysis argues that Fe_3O_4 should be more strongly interacting than γ-Fe_2O_3, even scaling to the measured blocking temperature. However, this is different from what we see experimentally, namely that the γ-Fe_2O_3 nanoparticles are significantly more interacting than the Fe_3O_4 nanoparticles. This contradiction between the theoretical and experimental expectations for the relative interaction energies is relatively robust against changes in the interparticle spacing, which is the largest uncertainty in this analysis. Therefore, we conclude that the assumption underlying this analysis, namely that the interaction energy can be estimated from the mean particle spacing, is incorrect. Motivated by the fact that the effective interaction energy in the γ-Fe_2O_3 nanoparticles, which show clustering inside the alginate matrix, is larger than in the Fe_3O_4 nanoparticles, which are more uniformly distributed, we believe that fluctuations in the nanoparticle distribution can significantly affect the interaction energy. In turn, this implies that the interaction energy cannot be accurately estimated using only the mean particle spacing, but that the actual distribution needs to be considered.

4.4 CONCLUSIONS

The *ac* magnetic susceptibility measurements provide an opportunity to probe interaction effects in a single nanoparticle sample, without having to first determine the parameters in the non-interacting limit, at the expense of requiring measurements at a number of different frequencies. By analyzing the temperature dependent *ac* magnetic susceptibility data and by fitting it to the Vogel-Fulcher equation, we find that the γ -Fe_2O_3 nanoparticles in alginate exhibit stronger interactions than the homogeneous Fe_3O_4 nanoparticle sample. However, estimates of

the dipolar interaction energies, using the expected mean values for interparticle spacings, predicts that the interactions in the Fe_3O_4 nanoparticle ensemble should be stronger than for the γ-Fe_2O_3 nanoparticles embedded in the alginate matrix. We hypothesize that the effective nanoparticle interactions depend strongly on the actual distribution of the nanoparticles and not just on the mean spacing.

CHAPTER 5

INVESTIGATING INTERACTIONS AND MAGNETIC RELAXATION IN BORON DOPED Mn_3O_4 NANOPARTICLES

5.1 INTRODUCTION

Mn_3O_4 Nanoparticles

When the oxides, hydroxides, carbonates, nitrates and sulfates of Manganese are heated above 1000^0 C in air, Mn_3O_4 gets formed as the main product [110]. The stable room-temperature phase for Mn_3O_4 is tetragonal hausmannite (space group I_{41}/amd). Mn_3O_4 has a normal spinel crystal structure where Mn^{3+} ions occupy the octahedral sites and Mn^{2+} ions occupy the tetrahedral sites as shown in figure 5.1 [111]. The octahedral site is distorted following the Jahn-Teller effect on the Mn^{3+} ions. Bulk Mn_3O_4 is paramagnetic at the room temperature but assumes ferrimagnetism below the critical transition temperature of about 42 K [112] [113]. Mn_3O_4 is an important transition metal oxide and finds applications in various fields like high-density magnetic storage media, catalysts, ion-exchanging materials among others [111-113]. It is used as a raw material for making soft magnetic materials [114]. It serves as an important catalyst in controlling air pollution by reducing the emission of NO_x and CO. It is believed that Mn_3O_4 nanoparticles, having a greatly increased surface to volume ratio, can be particularly important for these applications [111, 112, 114].

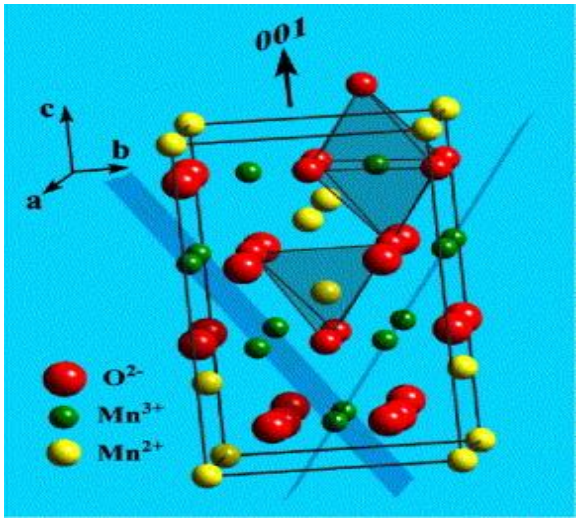

Figure 5.1 The normal spinel structure of Mn_3O_4 with Mn^{2+} ions occupying the tetrahedral sites (yellow) and Mn^{3+} ions occupying the octahedral sites (green) [112].

Bulk Mn_3O_4 is paramagnetic at room temperature but it develops ferrimagnetic order below the Neel temperature (T_N) 42 K [34]. The formally predicted superparamagnetic blocking temperature (T_B) for 15-25 nm sized Mn_3O_4 nanoparticles, using an average value for magnetocrystalline anisotropy calculated from the studies of Tackett *et al.*[38], varies from approximately 15 K to 65 K. Therefore, Mn_3O_4 nanoparticles provide a system where T_B can overlap with T_N. Two additional magnetic phase transitions, associated with the development of additional antiferromagnetic spin structures, are observed near 39-40 K and 33-34 K in bulk Mn_3O_4 [38, 113]. However, *ac* susceptibility measurements on Mn_3O_4 nanoparticles do not detect any signature of these two magnetic phase transitions, although a peak in magnetic dissipation is seen below 33 K in earlier studies [38, 113].The origin of these low temperature magnetic features in Mn_3O_4 nanoparticles is still under debate and has been associated with either superparamagnetic blocking [38] or to surface spins [113] . Our goal is to investigate interaction effects of Mn_3O_4 nanoparticles in solid-state samples. We exploited a feature of Mn_3O_4 nanoparticles namely that they readily convert to antiferromagnetic (AFM) α-Mn_2O_3 (80

K< T_N < 100 K)[115] and γ-MnOOH (T_N < 45 K)[116] under ambient conditions. This allowed us to prepare solid composites containing ferrimagnetic Mn_3O_4 particles with distinct average interparticle separations and therefore different interaction regimes. These samples allow us to explore interaction effects in nanoscale materials in a very different regime than superparamagnetic Fe_3O_4 nanoparticles, where the ferrimagnetic ordering temperature (>800 K)[117, 118] is much larger than the superparamagnetic blocking which falls generally below room temperature [119].

5.2 EXPERIMENTAL PROCEDURE

Synthesis of Mn_3O_4 nanoparticles

9.9 g of $MnCl_2.4H_2O$ was added to 50 ml of HCl and deionized water mixed in the ratio of 1:9. 25 ml of NH_4OH solution was added drop wise on to the mixture when light brown precipitate was formed. The solution containing the residual basic ions was washed several times with deionized water until it showed a pH value of 7. The light brown precipitate was filtered out and dried in a crucible in presence of air for 1h at 100^0C. The dried powder was again heated at 500^0C in air for 1 h until it became dark brown.

Synthesis of boron doped Mn_3O_4 nanoparticles

For synthesizing the 5 at.% boron doped nanoparticles, the same procedure as mentioned above was followed with the exception that $MnCl_2.4H_2O$ and H_3BO_3 was initially added to the 1:9 mixture of HCl and deionized water in a molar ratio of 2.85:0.15. We obtained light brown precipitate, which was washed with deionized water to make the solution neutral. The precipitate was filtered out and dried in air at 100^0C. The dried powder was again heated at 500^0C in air for 1 h when it turned to dark brown.

5.3 RESULTS AND DISCUSSION

5.3.1 X-ray diffraction

The XRD spectra of the MO and BMO nanoparticle samples are plotted in figure 5.2. The XRD spectrum of MO nanoparticles in figure 5.2 (a) shows the formation of Mn_3O_4 along with α-Mn_2O_3 and γ-MnOOH. (JCPDS Card Nos. 24-0734, 71-0636, 41-1379). The average crystallite size of the nanoparticles is estimated by the Debye Scherrer equation given by $d=0.9\lambda/\beta\cos\theta$, where d is the average crystallite size of the particle, λ is the X-ray wavelength (0.154 nm) and β is the full-width at half maxima of any reference peak corresponding to a Bragg angle θ [113]. The size of Mn_3O_4 and Mn_2O_3 nanoparticles estimated from their most intense peaks are roughly 35 nm and 30 nm respectively. The unwanted production of α-Mn_2O_3 and γ-MnOOH is widely associated with the synthesis of Mn_3O_4 nanoparticles [115, 120]. The transformation of Mn_3O_4 into Mn_2O_3 through annealing at an elevated temperature of 600^0C was previously reported by Wang *et al.*[115] Studies have also claimed that oxidation of Mn_3O_4 particles having a low surface area at temperatures above 400^0 C always leads to the production of α-Mn_2O_3[121]. The formation of γ- MnOOH nanowires together with Mn_3O_4 nanoparticles via a hydrothermal treatment was also reported in earlier studies by Zhang *et al*. [120] When exposed to air under ambient conditions, Mn_3O_4 particles can also get converted to MnOOH [122]. These reports suggest that development of α-Mn_2O_3 and γ-MnOOH phases occurs routinely during the preparation of Mn_3O_4 nanoparticles. The instability of spinel Mn_3O_4 is also confirmed when XRD performed on initially phase pure nanoparticle samples held under ambient conditions for several years also show the production of other Mn oxide phases (not shown).

The distinct peaks in figure 5.2 (b) confirm the synthesis of crystalline nanoparticles having the Mn_3O_4 structure (JCPDS Card No.24-0734) in the boron doped sample. Rather unexpectedly, we find that incorporating boron does not show any noticeable shift in 2θ relative to pure Mn_3O_4 nanoparticles and, more significantly, it minimizes the oxidation to other Mn oxide phases. The boron doped Mn_3O_4 nanoparticles show considerably better stability than undoped nanoparticles and, as confirmed with magnetic measurements shown in the following, produce phase-pure nanoparticles. Studies on boron substituted $LiMn_2O_4$ spinels have reported the occupancy of boron only in the octahedral Mn^{3+} sites [123], which we also expect for our BMO sample. Peaks corresponding to the diffraction planes (112), (103) and (211) have been considered in calculating the nanoparticle size. The average crystallite size calculated for the Mn_3O_4 nanoparticles in the BMO sample using the Debye Scherrer equation is approximately 23 nm. Thirunakaran *et al.* [123] have reported the formation of borates in studies performed on boron substituted $LiMn_2O_4$ spinels. The stability of the boron doped sample possibly hints at the formation of a borate layer or coating on the surface of the particles, which could prevent the oxidation of Mn_3O_4 to other Mn oxide phases in the BMO sample. Previous studies have found this borate layer to be a potential candidate for the prevention of oxidation [124].

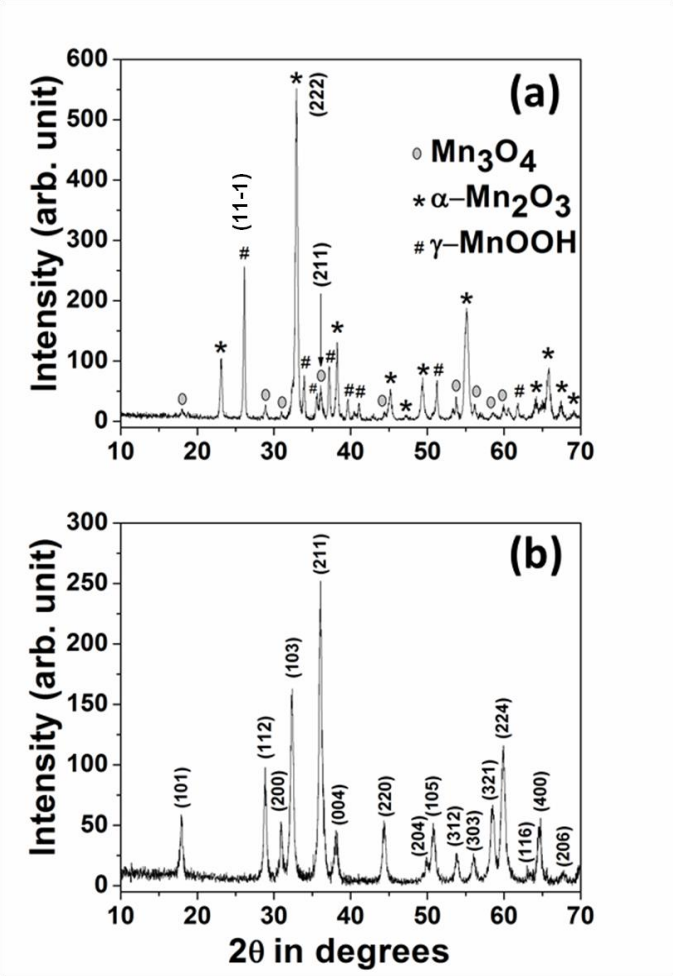

Figure 5.2 XRD spectra of (a) MO and (b) BMO nanoparticles.

5.3.2 Transmission electron microscopy

We further characterized the morphology of these nanoparticles using transmission electron microscopy (TEM). Figure 5.3 (a) shows the formation of roughly spherical nanostructures in the BMO sample with figure 5.3 (b) depicting the image of one such particle having a diameter between 26 nm and 28 nm. From the histogram showing the particle size distribution in the inset of figure 5.3 (b), the most probable diameter estimated for these nanostructures is 27 nm with a standard deviation of 4 nm. The average size of nanoparticles in the BMO sample extracted from TEM measurements is slightly larger than the crystallite size

determined by the XRD technique. This increase in the estimated particle size may be attributed with the formation of an amorphous layer on the surface of the nanoparticle, a typical signature also observed by Regmi *et al*. [113] for phase pure Mn_3O_4 nanoparticles. Several tiny particles having sizes approximately ranging between 2 nm to 5 nm are observed in the TEM image of the BMO sample in Figure 5.3(a). No such particles are found in the TEM image for the MO nanoparticle sample as shown in figure 5.3 (c). We therefore tentatively attribute the very small nanoparticles seen in figure 5.3(a) to a B_2O_3 impurity phase, which, because of their very small size, could not be detected using XRD. This was confirmed by preparing a 1 *at.*% boron substituted Mn_3O_4 nanoparticle sample (not shown), which still has phase-pure XRD patterns, but does not show any small particles in the TEM images. Based on the observations, we suggest that the solubility of boron in the spinel Mn_3O_4 structure is not more than a few *at.*%. Since both the Mn_3O_4 and Mn_2O_3 particles have roughly the same size, we believe that this approach synthesizes individual nanoparticles having different crystal structures rather than preparing nanoparticles having core-shell structures. Wang *et al.* [115] have also showed the existence of such individual Mn_2O_3 and Mn_3O_4 nanoparticles on the surface and inside of Mn_2O_3/Mn_3O_4 nanoclusters respectively. The figure 5.3 (d) represents a high resolution TEM (HRTEM) image of the MO sample possibly depicting the (11-1) planes of γ-MnOOH (JCPDS Card No. 41-1379). We have also performed the Wavelength Dispersive Spectroscopy (WDS) measurements to determine the boron content in our sample. While we could detect the presence of boron in BMO (not shown), we were unable to quantify its actual content due to the lack of suitable standards.

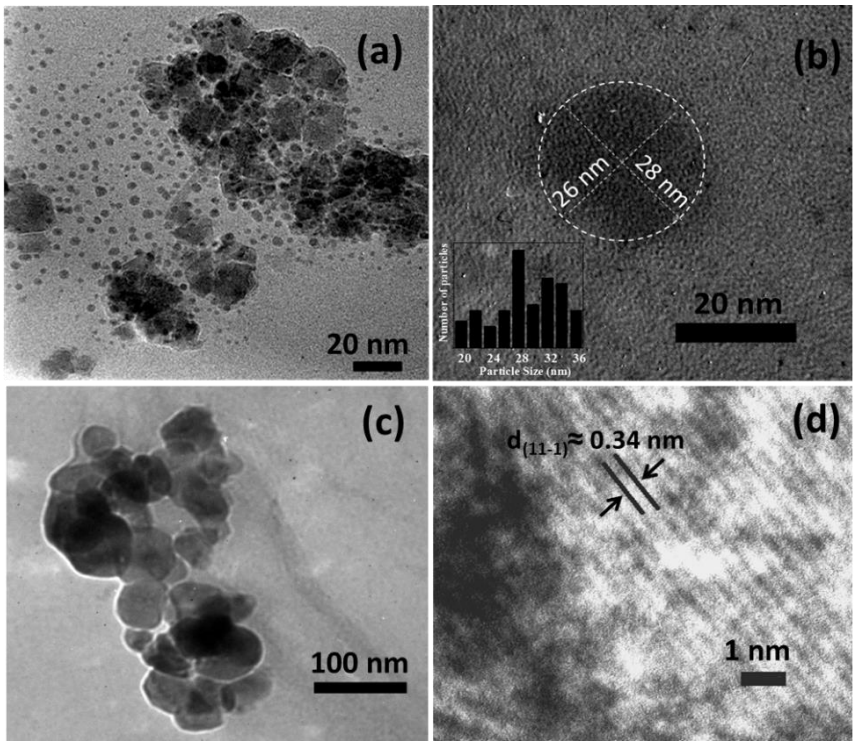

Figure 5.3 TEM images for BMO (**a** & **b**) and MO (**c** & **d**) nanoparticles. The inset in figure 5.3(b) represents the histogram showing particle size distribution for BMO nanoparticles. The figure 5.3(d) shows a HRTEM image of sample MO depicting the (11-1) planes of γ-MnOOH.

5.3.3 Magnetic measurements

Figures 5.4 (a) and 5.4 (b) show M *versus* H plots for the MO and BMO nanoparticle samples measured at a temperature of 30 K, which is well below T_N. These magnetization curves show features that can be associated with both a saturating ferrimagnetic moment together with a paramagnetic contribution. The ferrimagnetic response arising from Mn_3O_4 dominates the magnetization at lower fields, up to approximately 10 kOe. However, at higher magnetic fields, the linear magnetization curve means that the paramagnetic contribution becomes increasingly significant. We estimated the saturated contribution from the ferrimagnetically ordered Mn_3O_4 by subtracting the paramagnetic term estimated from the high-field magnetization. The saturation

magnetization (M_s) for BMO, approximately $M_s \approx 23$ emu g^{-1} (a volumetric saturation magnetization of $m_s \approx 115$ emu cm^{-3}, assuming the density of Mn_3O_4 nanoparticles is close to bulk) is substantially larger than that of the MO sample, which has $M_s \approx 8$ emu g^{-1} ($m_s \approx 40$ emu cm^{-3}). The saturation magnetization for bulk Mn_3O_4 is roughly 38 emu g^{-1},[125] and somewhat lower for nanoparticles [38]. The relatively large M_s value for BMO confirms that the sample consists of almost phase pure Mn_3O_4 nanoparticles, while the substantially smaller saturation magnetization for MO is consistent with the presence of a considerable fraction of secondary phases.

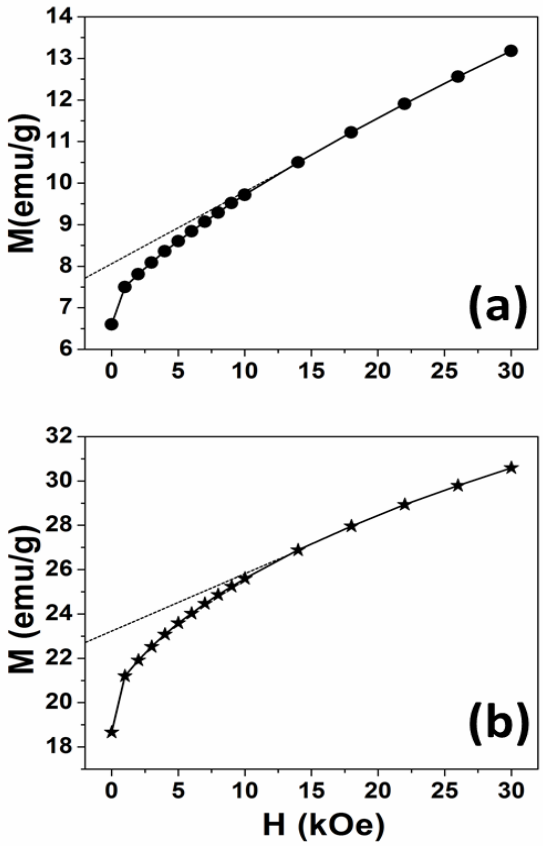

Figure 5.4 M (dc-magnetization) *versus* H (magnetic field) plots for (a) MO and (b) BMO nanoparticles recorded at 30 K.

We fit the linear high field portions of the magnetization curves in figure 5.4 to determine the effective Curie constant [117] (*C*) (per mole of Mn_3O_4) and from this, estimate the paramagnetic contribution from these nanoparticles. The Curie constant estimated for the BMO sample is approximately 1.7 emu K mol^{-1} Oe^{-1}, representing about 40 % of the *C* value for 1 mole of Mn^{2+} ions. Therefore, neglecting the distribution of Mn^{2+} and Mn^{3+} ions in Mn_3O_4, we propose that nearly 40% of the Mn spins remain paramagnetic in BMO. This estimate is very much consistent with the reduction in the saturation magnetization (M_s) for these nanoparticles by 40% with respect to the value for bulk Mn_3O_4. For the MO nanoparticle sample, the Curie constant is calculated to be 1.2 emu K mol^{-1} Oe^{-1}, which would be roughly 30% of the value expected for Mn^{2+} ions. Although this value is very approximate, both neglecting the mass difference between Mn_2O_3 and Mn_3O_4 and the mixture of Mn^{2+} and Mn^{3+} spins, this allows us to begin the estimate of the relative ferrimagnetic, paramagnetic, and antiferromagnetic components in the MO sample. The saturation magnetization (M_s) for the MO sample is reduced by nearly 80 % relative to bulk Mn_3O_4. This large decrease in the ferrimagnetic signal reflects not only the existence of paramagnetic moments but also indicates the presence of antiferromagnetically ordered phases in MO, which contributes to neither the saturated moment nor the paramagnetic susceptibility. Based on our estimate that approximately 30% of the Mn spins in the MO sample remain paramagnetic, we conclude that nearly 45-50 % of the Mn ions are antiferromagnetically ordered in this sample, consisting of the α-Mn_2O_3 and γ-MnOOH phases. We note that both ferrimagnetic (Mn_3O_4) and antiferromagnetic (α-Mn_2O_3 and γ-MnOOH) nanoparticles are expected to have paramagnetic surface spins, so the volume fraction of Mn_3O_4 in the MO sample is relatively small.

The zero-field-cooled (ZFC) and field-cooled (FC) magnetization for the MO and BMO nanoparticle samples are plotted in figures 5.5 (a) and 5.5 (b) respectively. The sharp increase in magnetization, close to 40 K in both curves marks the paramagnetic-to-ferrimagnetic phase transition in the Mn_3O_4 nanoparticles. A much larger FC/ZFC splitting, consistent with the larger value for M_S, is observed in the BMO sample as compared to the MO sample. Figure 5.5(c) plots the in-phase component of the *ac* susceptibility (χ') *versus* temperature (T) for the MO and BMO nanoparticle samples for an excitation frequency of 10 kHz under an excitation field of 10 Oe. The frequency-independent peak observed near 40 K represents the ferrimagnetic ordering temperature corresponding to Mn_3O_4 nanoparticles. The Neel temperature (T_N) calculated for the MO and BMO samples are 42 K and 41 K respectively. This slight suppression in the transition temperature by approximately 1 K in the boron doped sample (BMO) is also observed in the FC/ZFC measurements.

Figure 5.5(c) represents in-phase component of the *ac* magnetic signal (χ') *vs* temperature (T) for the two different Mn oxide nanoparticle samples. The magnitude of χ' provides a method for determining the ordered Mn_3O_4 fraction present in the samples. The amplitude of the magnetic response at the ferrimagnetic transition temperature for Mn_3O_4 nanoparticles is taken as an approximate measure of the sample phase purity, although this underestimates the Mn_3O_4 fraction because of the existence of a non-magnetic surface layer on the nanoparticles. The amplitude of χ' for the BMO sample approximately agrees with that measured for phase pure Mn_3O_4 nanoparticles reported by Regmi *et al*.[113] as well as values measured by Martin *et al*.[126]. These temperature dependent susceptibility measurements are therefore consistent with the suggestions that the BMO sample contains phase-pure Mn_3O_4 nanoparticles with no secondary phases. The marked decrease in the amplitude of χ' for the MO sample is consistent

with results from our XRD measurement where we clearly see the formation of several other Mn oxide phases in addition to Mn_3O_4. This reduction in the magnetic signal by approximately a factor of three (from $6x10^{-3}$ emu/g-Oe in BMO to $2x10^{-3}$ emu/g-Oe in MO) is attributed to the presence of secondary paramagnetic and antiferromagnetic phases in sample MO, which do not show any ferrimagnetic response at T_N. This is a different interpretation from some previous studies, where the relative decrease in the magnetic susceptibility was attributed to reduced interparticle interactions among Mn_3O_4 nanoparticles suspended in a polymer solution [127]. Because the impurity phases are AFM, their contribution to the ferrimagnetic signal can be approximately neglected. In principle, there could be signatures of additional magnetic effects at the interfaces between the different Mn oxide phases in the MO sample. These effects may be distinguished in exchange-bias measurements, which are sensitive to the interfacial spin arrangement. Because the *ac* magnetic measurements presented in the study are performed at zero bias field, these possible contributions have been neglected.

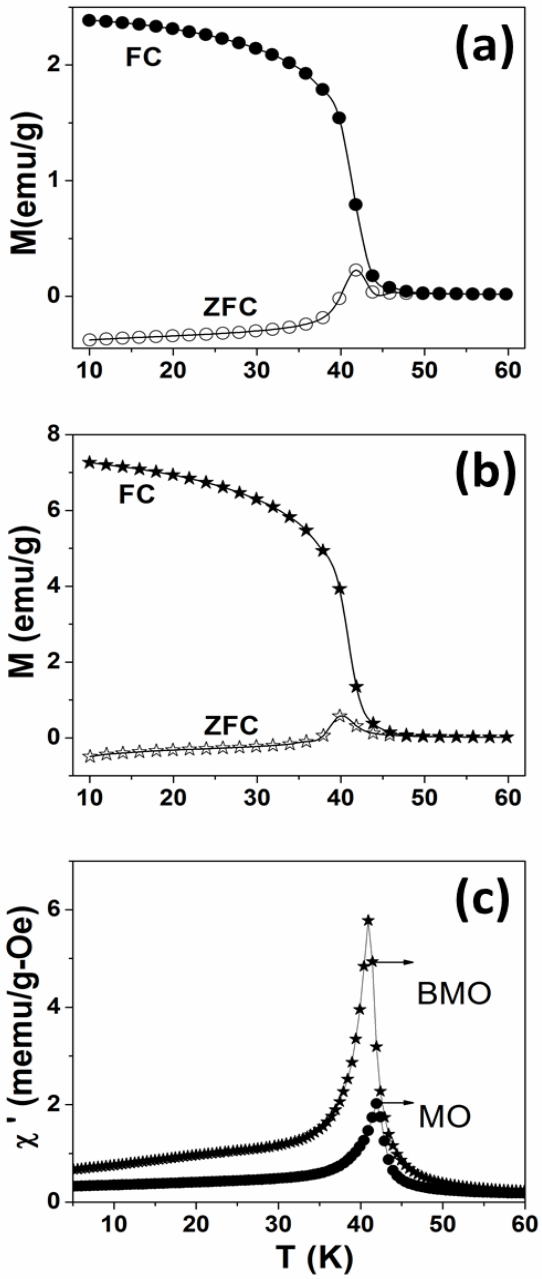

Figure 5.5 Zero-field-cooled (ZFC) and field-cooled (FC) magnetization curves for (a) MO and (b) BMO nanoparticles measured at 100 Oe. (c) In-phase susceptibility (χ') *vs* Temperature (T) graph for MO and BMO nanoparticles at a specific frequency of 10kHz under an excitation field of 10 Oe.

The low temperature magnetic relaxation for both the MO and BMO samples is shown in figure 5.6(a) for three different excitation frequencies: 100 Hz, 1 kHz and 10 kHz. The

pronounced peaks at low temperatures reflect the onset of magnetic relaxation in these systems. As the temperature range for this relaxation is very similar for both the MO and BMO systems, we argue that the relaxation arises solely from Mn_3O_4 nanoparticles, and is not affected by any other secondary phases. One of the primary parameters used to distinguish between an interacting and a non-interacting system is the dimensionless temperature dependent frequency shift of the relaxation peak given by $\alpha = \Delta T/[T\Delta(log_{10} f)]$. Here, ΔT is the difference between two frequency (f) dependent temperatures and T is the mean value between them [24]. For strongly interacting systems, the value of α lies between 0.005 and 0.05, while weakly interacting and non-interacting systems are typically described by α assuming values greater than approximately 0.05 and 0.13 respectively [24]. To analyze the nature of the magnetic relaxation, we fit the low temperature relaxation at frequencies of 100 Hz, 300 Hz, 1 kHz, 3 kHz, 6 kHz and 10 kHz to the Neel-Brown equation. For the MO nanoparticle sample, this yields τ_0 in the order of 10^{-12} s, as shown in figure 5.6(b), with the dimensionless relaxation parameter α close to 0.18. This relatively large magnitude of α, together with the physically meaningful value for τ_0 rule out any significant interactions in the MO nanoparticle system. The magnetic relaxation for the MO sample containing additional secondary phases acting as non-magnetic spacers between the ferrimagnetic Mn_3O_4 cores are thus well described by the non-interacting Neel-Brown model. This magnetic blocking occurs below the temperature predicted for 25-35 nm sized Mn_3O_4 nanoparticles. This discrepancy may be attributed to a difference in the effective particle volume or could reflect some modification to simple Neel-Brown theory when the blocking temperature overlaps with the magnetic ordering temperature.

Converse to the non-interacting MO sample, Neel-Brown fits to the magnetic relaxation in the BMO nanoparticle sample (figure 5.6 (c)) extract a microscopic relaxation time τ_0 that is

unphysically small, 8×10^{-16} s. However, the low temperature magnetic relaxation can be fit to a Vogel-Fulcher equation (figure 5.6 (d)) giving the physically reasonably value of τ_0 of roughly 10^{-12}s with T_o= 4.5 K and E_A/k_B =186 K. The value of the dimensionless interaction parameter α determined for the BMO sample, consisting only of phase pure Mn_3O_4 nanoparticles, is approximately 0.09. Both the values of τ_0 and α correspond to weak, but not insignificant, interactions in the BMO sample. Additionally, the ratio of the effective interaction temperature from this Vogel-Fulcher fit to blocking temperature (~ 15 K), T_o/T_B, is relatively small, only 0.3, again consistent with weak interactions among the Mn_3O_4 nanoparticles ($T_0/T_B \approx 0.9$, signifying spin glass features, indicative of strong interactions, in nickel ferrite nanoparticles[74]).

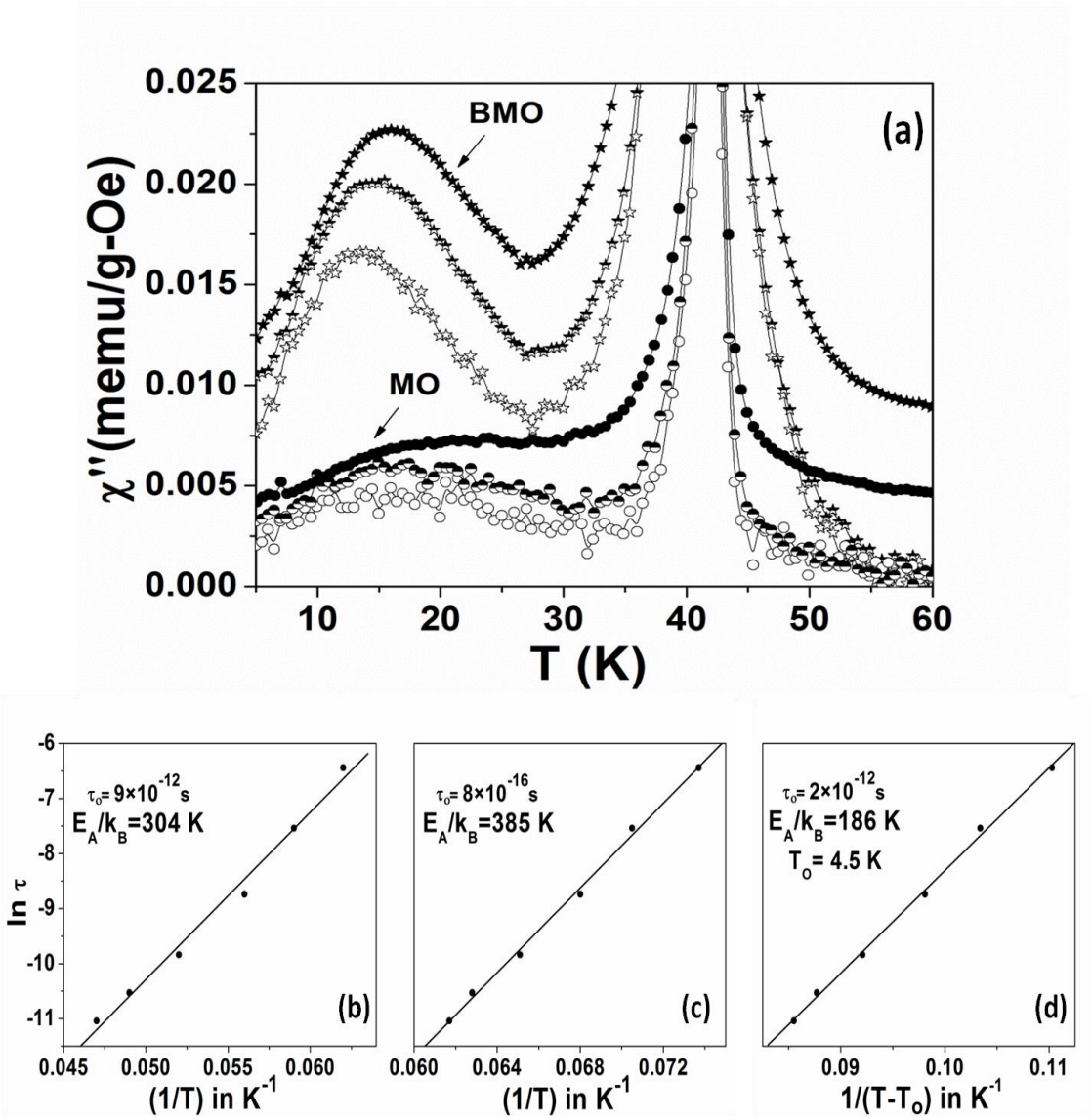

Figure 5.6 (a) Out-of-phase susceptibility (χ'') *vs* Temperature (T) graph for MO and BMO nanoparticles at three different frequencies of 100 Hz (open symbols), 1kHz (half-filled symbols) and 10kHz (filled symbols) under an excitation field of 10 Oe. The curves have been offset vertically for clarity. Neel-Brown fits for (b) MO and (c) BMO nanoparticles, (d) Vogel-Fulcher fit for BMO nanoparticles.

We attribute this crossover from non-interacting relaxation among the Mn_3O_4 nanoparticles in the MO sample to weakly interacting magnetic relaxation for nanoparticles in the BMO sample to increasing average dipolar interactions among the ferrimagnetic Mn_3O_4

cores. The dipolar interaction energy (E_d) between two adjacent magnetic nanoparticles is given by the expression

$$E_d = \frac{\mu_o \mu^2}{4\pi a^3}\left(\frac{\pi}{4}\right)^2 \quad (5.2)$$

with $\mu = m_s(\pi d^3/6)$,where μ, m_s, a and d represent the average moment, volumic saturation magnetization, average inter-particle separation and diameter of these nanoparticles respectively [33, 102]. For our nanoparticles, we estimate that m_s(BMO) ≈ 3m_s(MO) and d(MO) ≈ 1.5 d(BMO) (based on the magnetization data and size estimates from XRD and TEM), leading to μ(MO) ≈ μ(BMO). The antiferromagnetic secondary phases (α-Mn_2O_3 and γ-MnOOH) present in the MO sample act as non-magnetic spacers by increasing the average spacing (a) between the Mn_3O_4 ferrimagnetic cores. Assuming an average of a single α-Mn_2O_3 nanoparticle between two adjacent Mn_3O_4 ferrimagnetic cores, based on the very roughly 50% volume fraction for each in MO sample and close-packing for the BMO nanoparticles, we used Eq.(1) to estimate the relative dipolar interaction energies between the ferrimagnetic Mn_3O_4 cores in each set of samples. These calcuations suggest that the average dipolar interaction energy in BMO is approximately a factor of 20 larger than the magnetic interaction energies in MO. This substantially larger magnetic interaction in the BMO sample is qualitatively consistent with our measurement of the *ac* susceptibility for these nanoparticle samples.

5.4 CONCLUSIONS

Our findings reveal that incorporating a small percentage of boron can stabilize the spinel structure in Mn_3O_4 nanoparticles and prevent the unwanted conversion to other Mn oxide phases possibly due to the formation of a borate layer on the surface of the nanoparticles. We find that phase pure Mn_3O_4 nanoparticles (BMO sample) show a substantially larger signal at the

ferrimagnetic ordering temperature than the MO sample containing secondary phases, and suggest that the amplitude of this anomaly can serve as a measure of sample purity. The relaxation dynamics observed in the MO nanoparticle sample follows simple Neel-Brown behaviour consistent with a non-interacting system despite the proximity between the ferrimagnetic ordering and superaparamagnetic blocking temperatures. This relaxation is slightly modified for the boron stabilized nanoparticles, where the Mn_3O_4 nanoparticles are not separated by non-magnetic oxides and we find evidence of weak interactions as a perturbation to the non-interacting case. Although the Neel-Brown energy barrier is not fixed at the temperatures relevant for this magnetic relaxation, due to the temperature dependence of the magnetocrystalline anisotropy, the Neel-Brown model still seems to fit well for the non-interacting system and requires only a small modification in the interacting case. These studies demonstrate that the magnetic dynamics of nanoparticles can also be tuned by incorporating non-magnetic components into the sample.

CHAPTER-6

MAGNETIC PROPERTIES OF GADOLINIUM DOPED Fe_3O_4 NANOPARTICLES

6.1 INTRODUCTION

In the last few decades, iron oxide based nanoparticles have attracted huge attention because they offer applications ranging from magnetic recording to biomedicine [2, 128]. Studies have been conducted on several doped (Zn, Au and MgB_2) Fe_3O_4 nanoparticles [129-131] and also on magnetite based nanocomposites [132-134] in an attempt to tune their magnetic and dielectric properties and make them more effective for technological and biomedical applications. Researchers have extensively studied rare-earth doped spinels as an important candidate which finds applications in magneto-optical recording [135] as well as in MRI contrast agents [136]. It has been found that introduction of Gd^{3+} to the inverse spinel cobalt ferrite prepared through different synthetic routes has altered the average crystallite size, lattice constants and more importantly the magnetic properties [137, 138]. The concentration of the rare-earth ions inside the spinel is found to greatly influence the saturation magnetization which is considered to be a crucial parameter for determining the practical applications of these nanostructures. Till now, prominent studies conducted on Gd^{3+} doped Fe_3O_4 nanoparticles have essentially discussed about the proposed site of Gd^{3+} entry into the spinel structure [81], their low temperature magnetic properties [61] and also explored this material for future biomedical applications [89, 136]. It has been observed that introduction of Gd^{3+} into Fe_3O_4 causes structural defects resulting in an enhancement of *ac* magnetic features at low temperatures [61]. Studies have also found these nanoparticles to be of potential interest in cancer hyperthermia for treating malignant tumors [89].

Also, gadolinium chelate complexes and iron oxide nanoparticles are the most commonly used contrast agents for MRI imaging [139-141]. The former are well known for enhancing the T_1 (spin-lattice relaxation) [139-141] relaxation rates while the latter serve as an excellent T_2 (spin-spin relaxation) [139-141] contrast agent. The Gd-DTPA is the commonly used Gd based contrast agent for MRI purposes. In this complex, the Gd^{3+} ion having a magnetic moment of $7\mu_B$ has 9 coordination sites, out of which 8 sites are occupied by 5 oxygen and 3 nitrogen atoms of the carboxylates and the amines groups respectively. The remaining ninth site is occupied by a water molecule and as a result, there is a tendency of the water molecules to remain in close proximity with the Gd^{3+} ions. Since the effective electron-proton interaction energy falls as d^{-6}, so this distance of closest approach highly influences the rate of T_1 relaxation [140]. Again, superparamagnetic Fe_3O_4 nanoparticles with size less than 20 nm carry huge magnetic moments (>10,000 μ_B) and while diffusion through the tissues affect water molecules and can cause dephasing of the magnetic moments of protons which eventually enhances the T_2 relaxation rate ($1/T_2$) [140, 141]. Therefore, studies performed on PEGylated gadolinium doped Fe_3O_4 have found these nanoparticles favorable for T_1–T_2 dual-modal MRI contrast agent in the diagnosis of brain glioma cells [136]. Moreover, the presence of heavy metal Gd along with a highly magnetic component Fe could possibly make these nanoparticles a better candidate for multimodal imaging purposes [142, 143]. Hence, a detailed understanding regarding the magnetic behavior of this very unique system of Gd doped Fe_3O_4 nanoparticles is crucial so as to make it an efficient applicant for advanced biomedical purposes.

In the present study, we aimed for investigating the effect of gadolinium doping on the magnetic properties of Fe_3O_4 nanoparticles. We found that penetration of excess Gd^{3+} ions into Fe_3O_4 spinel has significantly influenced the average crystallite size and the saturation

magnetization as well as the magnetic susceptibility of our nanoparticle systems. The average crystallite size is found to increase with an enhanced Gd^{3+} concentration, while the reverse is true with the saturation magnetization of these nanoparticles. The magnetic hyperthermia studies were also conducted on one of the doped nanoparticle samples and the specific absorption rate (SAR) as a function of time was recorded.

6.2 EXPERIMENTAL PROCEDURE

Both undoped and Gd doped Fe_3O_4 nanoparticles were synthesized by using the chemical co-precipitation technique. $GdCl_3.6H_2O$ serves as the dopant material for the synthesis of the Gd doped nanoparticles. The structural and magnetic properties of these nanoparticles were studied by using X-ray diffraction and a Quantum Design physical property measurement system (PPMS).

Synthesis of Fe_3O_4 nanoparticles

An aqueous solution of $FeCl_3 \cdot 6H_2O$ (2.70g) and $FeCl_2 \cdot 4H_2O$ (1.00g) taken in a molar ratio of 2:1 were mixed in a beaker followed by drop-wise addition of 1(M) NH_4OH (125 ml) into the resulting mixture under continuous stirring. The black precipitate formed at the end of the reaction was washed with deionized water to remove the residual basic ions and then air-dried to produce fine powders of Fe_3O_4 (denoted by S1).

Synthesis of Gd doped Fe_3O_4 nanoparticles

For synthesizing 5 *at.*% Gd–Fe_3O_4 nanoparticles, aqueous solution of $FeCl_3 \cdot 6H_2O$, $FeCl_2 \cdot 4H_2O$ and $GdCl_3 \cdot 6H_2O$ were mixed in a beaker in a molar ratio of 1.85:1.00:0.15. Initially, 0.27 g of $GdCl_3 \cdot 6H_2O$ was added to 2.50 g of $FeCl_3 \cdot 6H_2O$ dissolved in distilled water and then after few minutes of stirring, aqueous solution containing 1.00g of $FeCl_2 \cdot 4H_2O$ was

poured into it. This was followed by drop-wise addition of 1(M) NH_4OH (125 ml) to the mixture containing the iron and gadolinium salts under continuous stirring. If the sequence in which these salts are added is altered, then the saturation magnetization of these nanoparticles can also get affected [61]. At first, a brown precipitate was obtained, which eventually turned black. The entire reaction was carried out in N_2 atmosphere in order to avoid the partial oxidation of Fe^{2+} to α-FeOOH as found in a previous study [61]. The solution was then washed with deionized water until it reached a neutral pH of 7. The precipitate was then air dried to obtain fine powders of Gd doped nanoparticles. For the preparation of 1 *at*.% and 2.5 *at*.% Gd–Fe_3O_4 nanoparticles, $FeCl_3 \cdot 6H_2O$, $FeCl_2 \cdot 4H_2O$ and $GdCl_3 \cdot 6H_2O$ were mixed in a molar ratio of 1.97:1.00:0.03 and 1.925:1.00:0.075 respectively and then the same procedure as mentioned above was adopted. For our simplicity, we denote the 1, 2.5 and 5 *at*.% doped Fe_3O_4 nanoparticles as S2, S3 and S4 respectively.

6.3 RESULTS AND DISCUSSION

6.3.1 X-ray diffraction

The figure 6.1 shows the XRD spectra of undoped and gadolinium doped Fe_3O_4 nanoparticle samples. All the well-defined diffraction peaks are indexed to the formation of inverse spinel crystal structure of Fe_3O_4 (JCPDS card number: 85-1436). The absence of any secondary peaks in all spectra confirms the formation of phase-pure nanoparticles. Following earlier studies, Gd^{3+} ions are most likely to replace the Fe^{3+} ions of the octahedral sites in inverse spinel Fe_3O_4 [81]. It is evident from the XRD spectra that doping of gadolinium does not have any significant impact on the crystal structure of Fe_3O_4. Using the Debye-Scherrer equation [61], the average crystallite size obtained for the S1, S2, S3 and S4 nanoparticles are approximately 12

nm, 11.5 nm, 13.5 nm and 18 nm respectively. Therefore, it has been found that the crystals grow bigger with an increase in the Gd doping percentage. This significant increase in the average crystallite size has previously been reported in studies conducted by Peng *et al.* on Gd doped $CoFe_2O_4$ spinel [135]. The gadolinium content in S2, S3 and S4 samples were estimated to be around 1.3, 3.0 and 5.5 at.% respectively according to the results obtained from the energy dispersive spectroscopy (EDS) measurements (not shown) conducted on these doped nanoparticles.

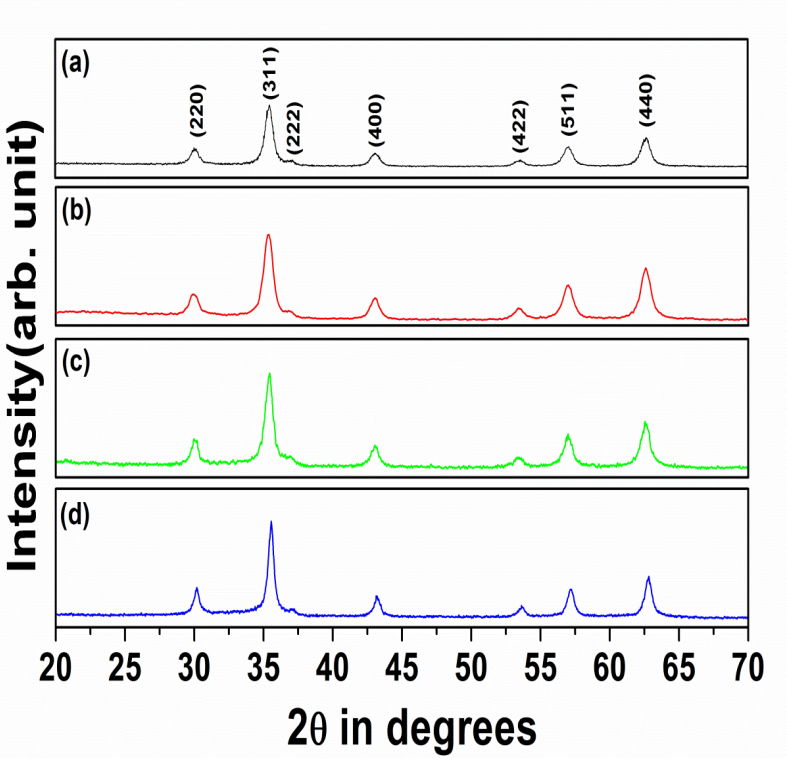

Figure 6.1 XRD spectra for (a) S1 (black), (b) S2 (red), (c) S3 (green) and (d) S4 (blue) nanoparticle samples.

6.3.2 Magnetic measurements

The magnetization (M) *vs* magnetic field (H) data for our nanoparticles recorded at 300K (room temperature) are shown in figure 6.2. The sigmoidal shape of these curves with nearly zero hysteresis confirms the superparamagnetic nature of these nanoparticles at the room

temperature. The saturation magnetization (M_s) values obtained for the S2, S3 and S4 samples are 65 emu/g, 51 emu/g and 45.5 emu/g respectively within the experimental uncertainties (±1 emu g^{-1}, coming mainly from the uncertainty in measuring the sample mass). The M_s value for undoped Fe_3O_4 nanoparticles (S1) is approximately 69.5 emu/g. From these data, it can certainly be concluded that an enhanced doping percentage of gadolinium could substantially decrease the saturation magnetization in Fe_3O_4 nanoparticles, an observation also seen in earlier studies [136]. The saturation magnetization decreases roughly by 35% in the S4 nanoparticles as compared to its undoped (S1) counterpart. This reduction in saturation magnetization at room temperature is attributed to the fact that magnetic Fe^{3+} ions are supposedly getting replaced by the non-magnetic Gd^{3+} ions ($T_c \approx 292$ K) [144] in the octahedral sites of the inverse spinel Fe_3O_4 [135].

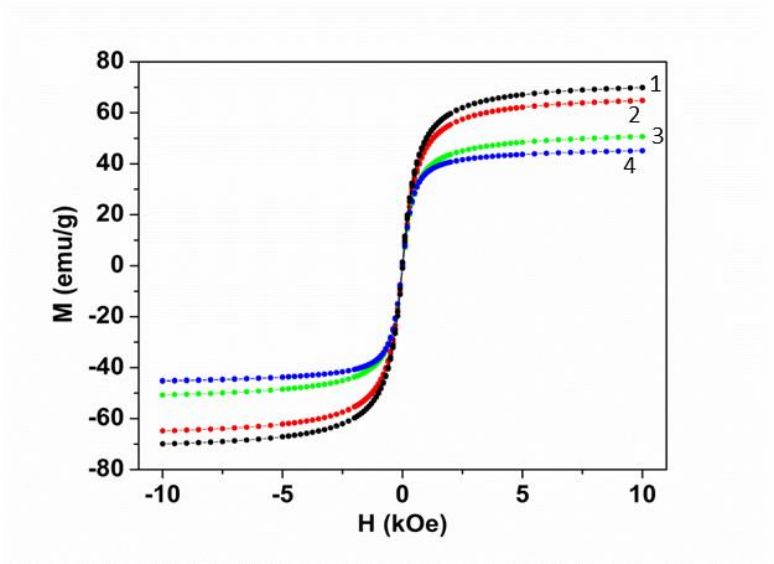

Figure 6.2 M *vs* H plots for 1. S1 (black), 2. S2 (red), 3. S3 (green) and 4. S4 (blue) nanoparticle samples at 300 K.

For understanding the *ac* magnetic dynamics of these nanoparticles, frequency dependent susceptibility measurements were performed on all samples. The real (in-phase) and the imaginary (out-of-phase) components of the *ac* susceptibilities (χ' and χ'') *vs* temperature (T) at

several different frequencies were plotted and analyzed. The figure 6.3 shows the χ' and χ'' *vs* T plots for all samples conducted at a specific frequency of 500 Hz under zero *dc* field and an *ac* excitation field amplitude of 10 Oe. The magnitudes of χ' and χ'' are almost the same in the S1 and S2 samples while it decreases with an increment in the Gd doping percentage as observed for the S3 and S4 nanoparticles. As expected, the nature of both χ' and χ'' curves for S1 (undoped) and S2 (1 *at.%* doped) samples are roughly identical, whereas the nanoparticles with an increased Gd content show a decrement in the susceptibility values. This is also in good agreement with reduced saturation magnetization values as seen for these nanoparticles. The occurrence of well-defined peaks in the χ'' *vs* T plots between 150 K to 200 K represent the superparamagnetic blocking of Fe_3O_4 nanoparticles [61].

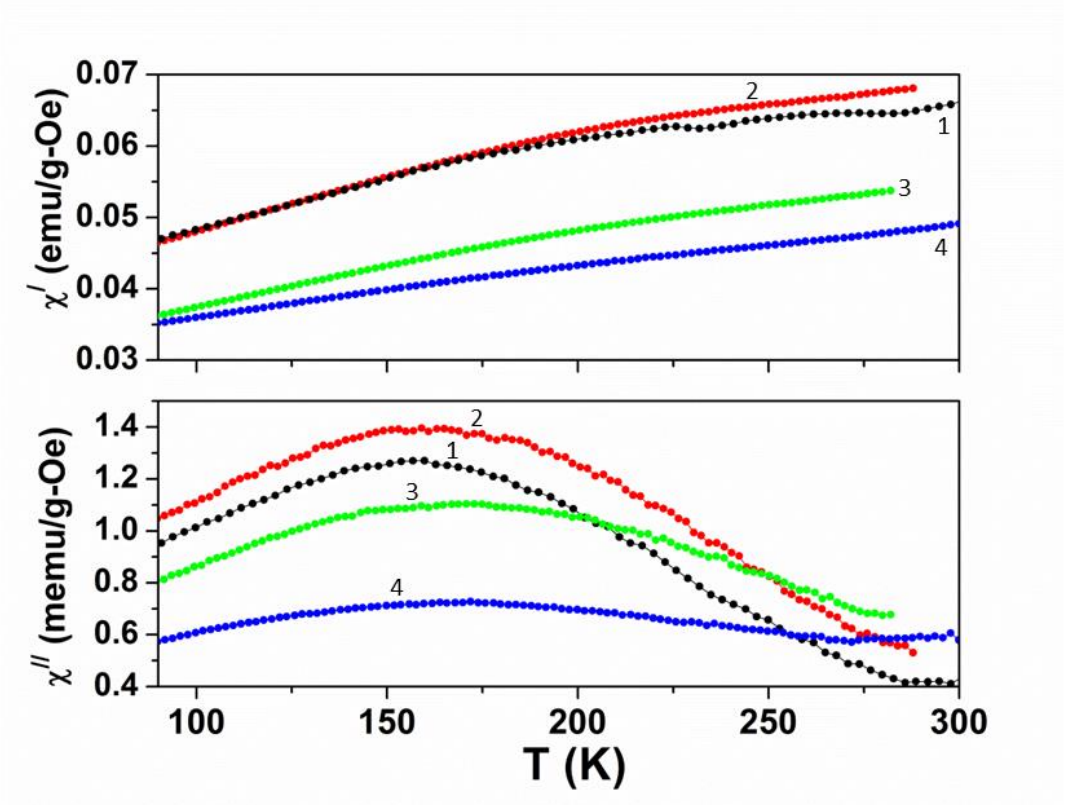

Figure 6.3 In-phase susceptibility (χ') & Out-of-phase susceptibility (χ'') *vs* Temperature (T) graphs for 1. S1 (black), 2. S2 (red), 3. S3 (green) and 4. S4 (blue) nanoparticle samples at a specific frequency of 500 Hz under an excitation field of 10 Oe.

The figure 6.4 shows the $\chi^{//}$ *vs* T plots for all samples conducted at six different frequencies of 500 Hz, 650 Hz, 800 Hz, 950 Hz, 1100 Hz and 1250 Hz under zero *dc* field and an *ac* excitation field amplitude of 10 Oe. The simplest model which describes the behavior of an ensemble of non-interacting and single domain magnetic nanoparticles is explained by the Neel-Brown (NB) theory. The mean relaxation time for the magnetic moments of such individual nanoparticles is governed by the Arrhenius relation given by $\tau = \tau_0 \exp (E_A/k_BT)$, where k_B is the Boltzmann's constant, T is the temperature and τ_0 is the attempt time characteristic of the material and is of the order of 10^{-13}–10^{-9} s. However, this model gets slightly modified with the introduction of interactions into the system and is expressed by the Vogel-Fulcher relation given by $\tau = \tau_0 \exp [E_A/k_B(T-T_0)]$, where T_0 measures the strength of the interaction. The information obtained from these frequency dependent peaks has been fitted to the Neel-Brown equation in order to understand the magnetic relaxation phenomena of these nanoparticles. The $\ln \tau$ *vs* 1/T plots shown in figure 6.5 represent the Neel-Brown fits for samples S1, S2, S3 and S4. The values of τ_o and E_A/k_B for all the samples are represented in Table 6.1.

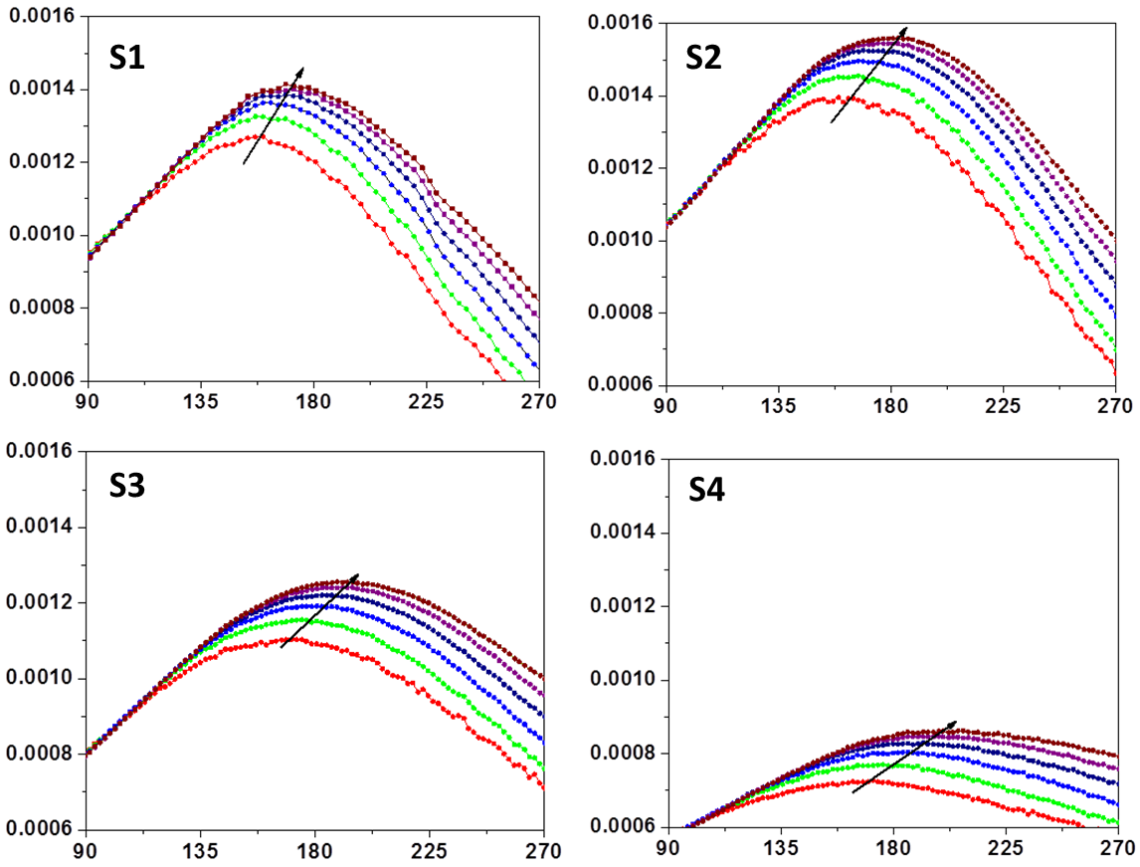

Figure 6.4 Out-of-phase susceptibility ($\chi^{//}$) *vs* Temperature (T) graph for S1, S2, S3 and S4 nanoparticle samples at six different frequencies of 500 Hz (red), 650 Hz (green), 800 Hz (blue), 950 Hz (navy), 1100 Hz (purple) and 1250 Hz (wine) under an excitation field of 10 Oe.

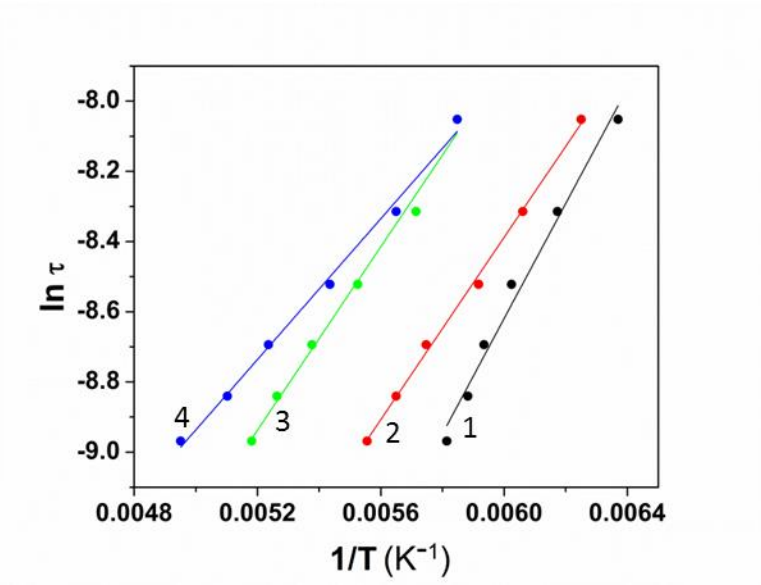

Figure 6.5 Neel-Brown fits for 1. S1 (black), 2. S2 (red), 3. S3 (green) and 4. S4 (blue) nanoparticle samples.

SAMPLES	τ_o (s)	E_A/k_B (K)
S1	9.6×10^{-9}	1640
S2	9.4×10^{-8}	1298
S3	1.5×10^{-7}	1305
S4	8.7×10^{-7}	1002

Table 6.1 τ_o and E_A/k_B values for S1, S2, S3 and S4 nanoparticle samples

The magnitude of τ_o is enhanced while E_A/k_B roughly diminishes (although the E_A/k_B values are almost the same for S2 and S3 nanoparticles) following an increment in the Gd doping percentage. The value of $\tau_o \approx 10^{-9}$s obtained for the S1 sample falls well within the accepted NB range and signifies superparamagnetic blocking in these nanoparticles. The magnetic dipolar

interaction energy (E_d) existing amongst these nanoparticles is estimated using the relation [33, 145] given by

$$E_d = \frac{\mu_o \mu^2}{4\pi a^3}\left(\frac{\pi}{4}\right)^2$$

with $\mu = m_s(\pi d^3/6)$, where μ, m_s, a and d represent the average magnetic moment, volumic saturation magnetization, average inter-particle separation and diameter of these nanoparticles respectively [145]. Considering close-packing, the magnitude of this interaction is found to be the highest, close to 0.031 eV at 300 K, for the S4 nanoparticle system while it revolves around 0.02 eV (~ 0.017 eV for S2 and S3 while ~ 0.022 eV for S1 samples) for the other nanoparticle samples. Although a very approximate way of estimating the dipolar interactions in an ensemble of magnetic nanoparticles [146], however, it can certainly be concluded that the order of magnitude of these magnetic interactions is very much comparable with the thermal energy (~ 0.026 eV) at the room temperature.

6.3.3 Magnetic Hyperthermia Measurements (MHT)

The MHT studies were performed on the dextran coated S1 and S4 samples and SAR as a function of time was recorded. The heating curves of the ferrofluids conducted at a frequency of 375 KHz and under an *ac* magnetic field amplitude of 235 Oe are shown in figure 6.6. The figure 6.7 represents the SAR corresponding to heating as a function of temperature for both the undoped and Gd doped samples. The SAR for our 18 nm sized S4 ferrofluid (~12 mg/ml) is found to be around 40 W/g near room temperature which is very much less when compared to the SAR (~110 W/g) obtained for 12 nm sized Fe_3O_4 ferrofluid (S1) (~12 mg/ml) sample taken under the same experimental conditions (235Oe, 375 kHz) [70, 147]. The magnitude of SAR is expected to increase for bigger sized particles [70], however, in this case we have seen that

doping of Gd (around 5 at.%) modifies the magnetic properties in such a way that the effective SAR decreases. This decrease in SAR for the S4 sample is attributed to the reduced values of saturation magnetization and E_A/k_B, which essentially is a measure of the magnetic anisotropy constant K [70].

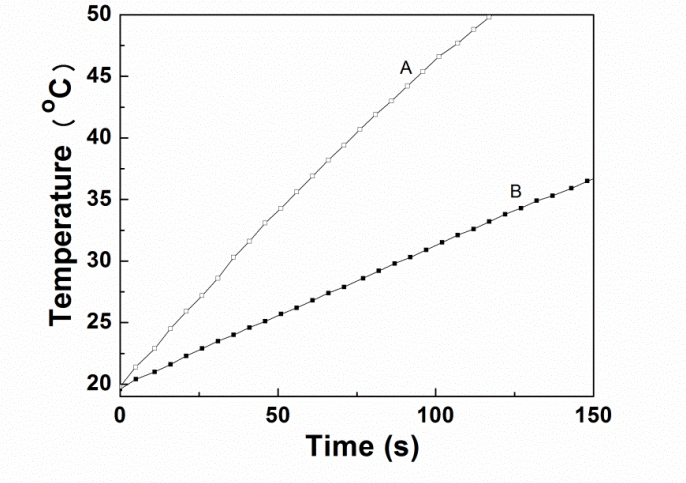

Figure 6.6 Temperature *vs* time plot for heating for A. S1 & B. S4 at a frequency 375 KHz and under an *ac* magnetic field amplitude of 235 Oe.

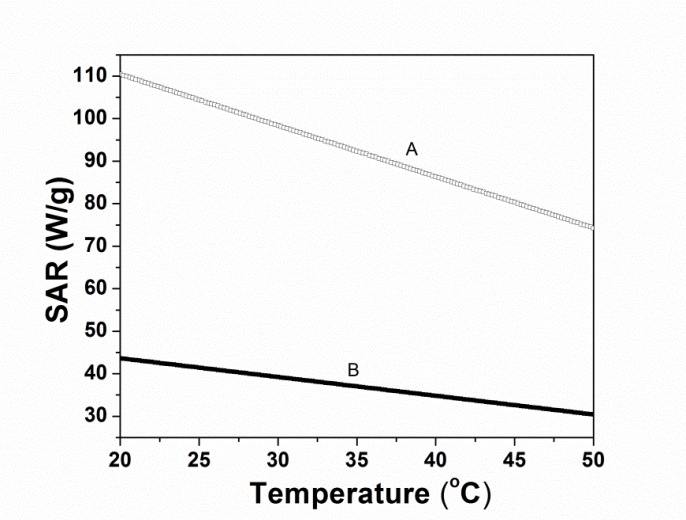

Figure 6.7 Variation of SAR for heating with temperature for A. S1 & B. S4 at a frequency of 375 KHz and under an *ac* magnetic field amplitude of 235 Oe.

6.4 CONCLUSIONS

The undoped and gadolinium doped Fe_3O_4 nanoparticles were synthesized successfully using the chemical co-precipitation technique. The average crystallite size estimated using the Debye-Scherrer equation increases with an increase in the Gd doping percentage. On contrary, the saturation magnetization decreases roughly by about 35 % in the S4 sample when compared to the undoped Fe_3O_4 nanoparticles. The effective SAR for the S4 sample decreases by a considerable amount when compared with undoped iron oxide ferrofluid. This decrease in SAR for the S4 sample is attributed to its reduced values of saturation magnetization and the magnetic anisotropy constant K. In future, we would also like to explore this material for possible biomedical applications in MRI as a T_1–T_2 dual-modal contrast agent.

CHAPTER 7

INTRACELLULAR DISTRIBUTION OF $BiFeO_3$ NANOPARTICLES INTO THE HUMAN PANCREATIC CARCINOMA (MIA PACA-2) CELL LINES

7.1 INTRODUCTION

$BiFeO_3$ (BFO) is a multiferroic material having a perovskite crystal structure (figure 7.1). It shows antiferromagnetic behavior below the Neel temperature, T_N = 643K and exhibits ferroelectricity with a ferroelectric Curie temperature, T_C = 1143 K [148]. The presence of room temperature multiferroic behavior makes BFO a useful material with potential applications in data storage, spintronics, quantum electromagnets, transducers, and microelectronic devices. [149]. Being an antiferromagnet at room temperature, bulk BFO exhibits negligible magnetization; however, a finite value of M_s is recorded for BFO nanoparticles due to the uncompensated surface spins [150]. Previous studies have shown that doping of BFO nanoparticles with elements like Gd, Eu, or Co could enhance this magnetization [151, 152].

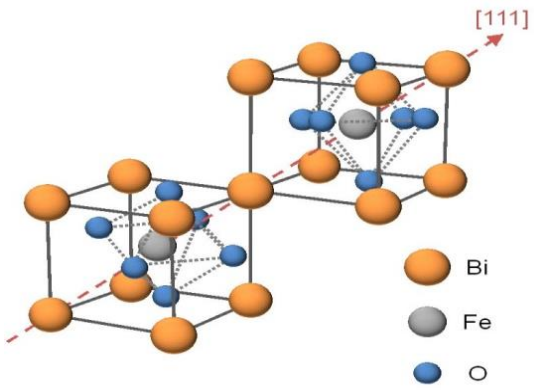

Figure 7.1 Perovskite structure of $BiFeO_3$ crystals [153]

In the current work, we present BFO nanoparticles as a potential candidate for imaging applications. The BFO nanoparticles may be particularly interesting as multimodal contrast agents for both magnetic resonance imaging (MRI) and x-ray imaging because these combine a

significant magnetic susceptibility with higher atomic mass constituents. We synthesized BFO nanoparticles using a chemical co-precipitation technique. We measured the structural and morphological characteristics of these nanoparticles using XRD, TEM, and DLS, and probed the magnetic properties through *dc* magnetization studies. In order to investigate the cytotoxicity and intracellular distribution of these BFO nanoparticles, we cultured them with the human pancreatic cancer cell line (MIA PaCa-2) and used optical microscopy to investigate the distribution and cell growth. We discuss the cytotoxicity of these nanoparticles, which will be a crucial factor for determining possible biomedical applications together with a discussion of the cellular distribution of these nanoparticles.

7.2 EXPERIMENTAL PROCEDURES

BFO nanoparticles were synthesized using a chemical co-precipitation technique with oxalic acid serving as the chelating agent. The structural and morphological properties of the BFO nanoparticles were characterized by XRD and TEM. A Rigaku MiniFlex 600 X-ray diffractometer generating Cu K_α radiation at a wavelength of 1.54 Å was used for the XRD analysis. A JEOL-2010 FasTEM transmission electron microscope operated at 200 kV was employed to capture high resolution microscopy images. The UV-Visible spectrophotometer (Evolution 220, Thermo Scientific) was also used for the optical characterization of these nanostructures. The stability of the colloidal dispersion of BFO nanoparticles was determined using a Zetasizer (Nano ZS90, Malvern Instruments) and the hydrodynamic sizes of these nanoparticles were determined from the Dynamic Light Scattering (DLS) measurements. The intracellular distribution of these nanoparticles into the human pancreatic carcinoma (MIA PaCa-2) cell lines was imaged with an optical microscope (Axiovert 200, Zeiss). The *dc* magnetic

measurements were also conducted on these nanoparticles by using a Quantum Design physical property measurement system (PPMS).

Synthesis of $BiFeO_3$ (BFO) nanoparticles

The nitrate salts of bismuth and iron, $Bi(NO_3)_3.5H_2O$ (1.94g) and $Fe(NO_3)_3.9H_2O$ (1.60g), mixed in a molar ratio of 1:1, were initially dissolved in 2 N nitric acid. Subsequently, oxalic acid (1.00g), taken in a 1:1 molar ratio with respect to the cations, was poured into the mixture containing the nitrates under continuous stirring. The reaction ended with the formation of an orange precipitate, which was dried initially in a hot plate at 150^0C for 30-45 minutes, followed by annealing in air at 600^0C for 2 h to produce fine powders of bismuth ferrite. The as-prepared powder was then collected for the structural, optical and magnetic characterizations followed by cell culture studies.

Cell Culture Protocol

MIA PaCa-2 human pancreatic cancer cells were grown on poly L-lysine-coated petri dishes at 37 ºC and 5 % CO_2, in Dulbecco's modified essential medium (DMEM) containing 10% fetal bovine serum (FBS) and 5% Penicillin-Streptomycin. To split the cells and plate them into other cell culture petri dishes, the cell culture dishes containing MIA PaCa 2 cells were obtained from the incubator, and the growth media was carefully aspirated. The cells were washed twice with 10 ml of sterile 1X phosphate buffered saline (PBS) at pH 7.4. This was followed by exposure to 0.25% trypsin in PBS for 3-4 minutes inside the incubator. Media containing DMEM, 10% FBS, and 1% antibiotics (Penicillin –Streptomycin- Glutomine) was added to the dish. The resulting cell suspension was centrifuged for 4 minutes at 1,500 rpm (300 xg), and the pellet re-suspended in 3 ml of cell growth medium. Then 1 ml of this suspension

was added to each new cell culture dishes containing 9 ml of media, and the dishes were placed in the incubator.

7.3 RESULTS AND DISCUSSION

7.3.1 X-ray diffraction

The XRD plot of the as-prepared BFO nanoparticles demonstrated the formation of phase-pure nanoparticles (JCPDS Card No. 86-1518), corresponding to the rhombohedral perovskite structure of bismuth ferrite (figure 7.2). The average crystallite diameter was approximately 33 nm, as determined from the major peaks (012), (104), and (110) using the Debye-Scherrer equation.

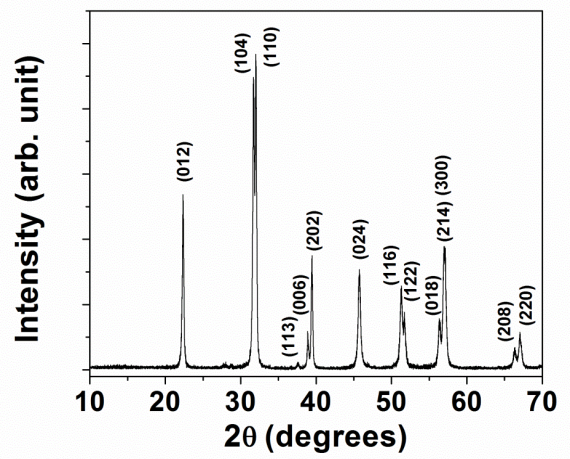

Figure 7.2 XRD spectra of BFO nanoparticles.

7.3.2 Transmission electron microscopy

TEM images were captured to investigate the morphology, shape and crystalline structure of these nanoparticles. The particles were found to be roughly spherical in shape and the TEM image clearly showed agglomeration for our BFO nanoparticle system (figure 7.3(a)). Figure 7.3(b) represents the high resolution TEM (HRTEM) image depicting the atomic planes (*indicated by arrows*) of the crystalline bismuth ferrite nanoparticles.

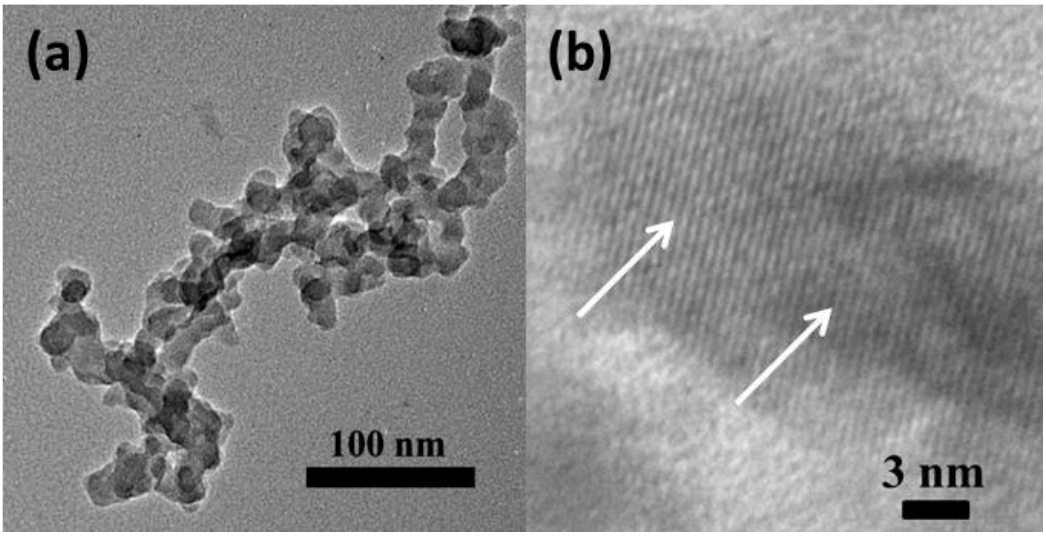

Figure 7.3 (a) TEM image of BFO nanoparticles (b) HRTEM image depicting the lattice planes of BFO .

7.3.3 UV-Visible spectrometry

The UV-Visible spectrum supports the production of phase-pure nanoparticles with an absorption maximum near 528 nm corresponding to BFO (figure 7.4) [154] .

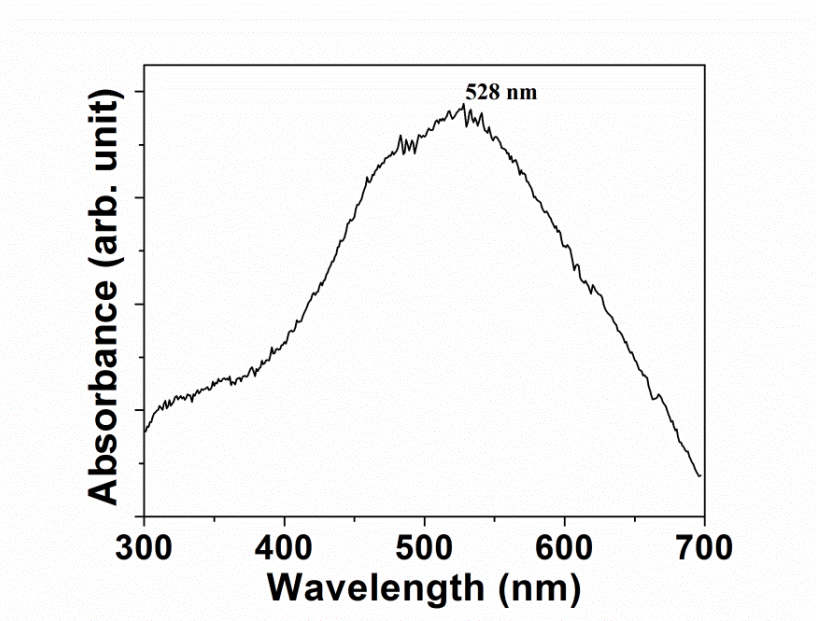

Figure 7.4 UV-Visible spectrum of BFO nanoparticles

7.3.4 Zeta potential & Dynamic Light Scattering (DLS) measurements

For a stable colloidal dispersion, zeta potential (ζ) generally assumes a high positive or negative value, usually $|\zeta| > 40$ mV. The zeta potentials for our BFO nanoparticles dispersed in deionized water were measured to be -12.5 ±1.5 mV (figure 7.5), and therefore these kind of low values of ζ suggest that the nanoparticles may not be well suspended in the solution.

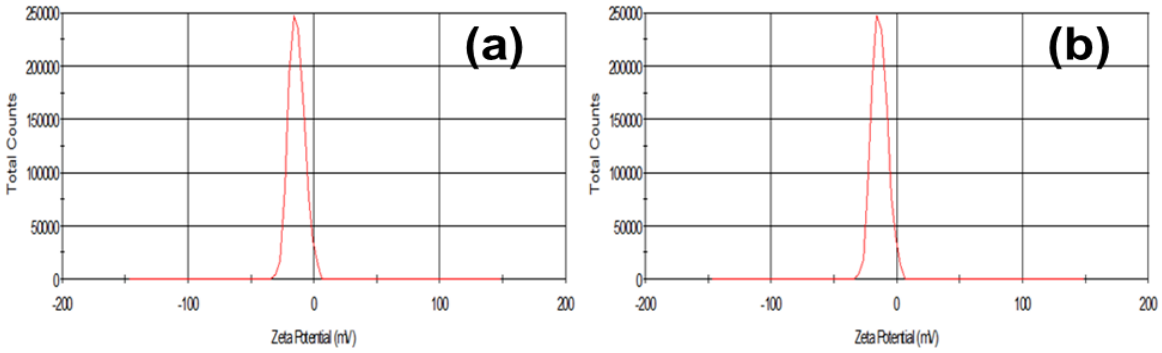

Figure 7.5 Zeta potential measurements of BFO nanoparticles dissolved in deionized water for two slightly different concentrations. ζ **(a)** = -11.6 mV and ζ **(b)** = -13.8 mV.

The DLS measurements determine the hydrodynamic diameter of these BFO nanoparticles to be approximately 400 nm, which once again signifies an increased agglomeration or clustering for our nanoparticle sample (figure 7.6).

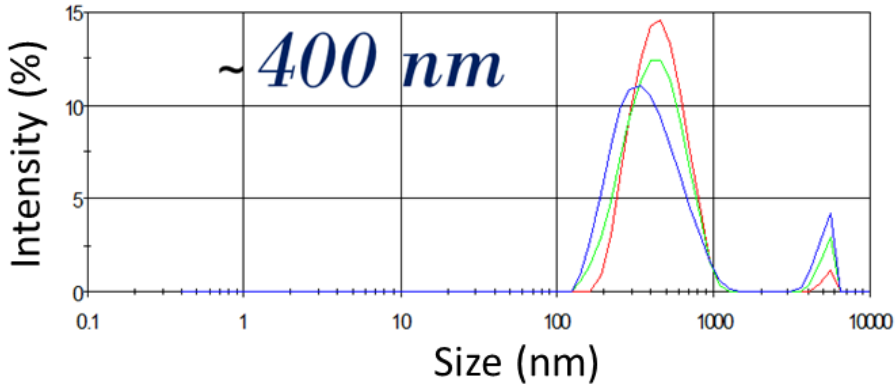

Figure 7.6 DLS measurements of BFO nanoparticles dispersed in deionized water**.** The red, green and blue curves represent three slightly different concentrations.

7.3.5 Magnetic measurements

Figure 7.7 shows the M *vs* H plot for BFO nanoparticles at room temperature. At very low fields (below 10kOe), the nanoparticles show weak magnetism with a saturation value of approximately 0.01emu/g, while paramagnetism dominates at much higher fields. Although BFO is antiferromagnetic at room temperature, the weak magnetic behavior below 10 kOe as shown in the inset of figure 7.7 is attributed to the uncompensated spins present on the surface of these nanoparticles [150].

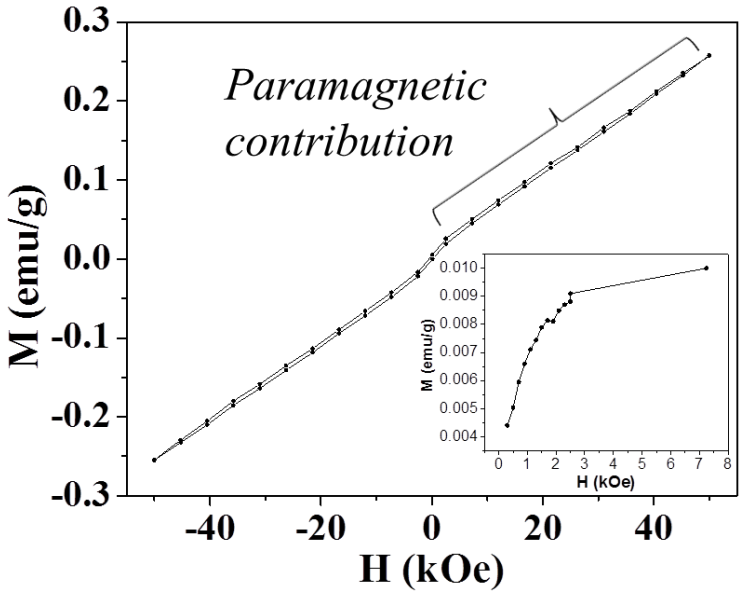

Figure 7.7 M *versus* H plot for BFO nanoparticles at 300 K. The inset shows the M *versus* H plot for BFO nanoparticles at 300 K after extraction of the paramagnetic contribution.

7.3.6 MIA PaCa-2 Cell studies

The BFO nanoparticles dispersed in deionized water (100 µg/ml) were exposed to MIA PaCa-2 cells. The petri dishes, three for each time point, were marked as 0 h, 24 h, 48 h and 72 h. Four other dishes containing the MIA PaCa-2 cells were also taken with each dish serving as control corresponding to one particular time frame. Immediately following exposure of

nanoparticles to the MIA PaCa-2 cells, the 0 h petri dish and its control were imaged under an optical microscope. Care was taken while imaging so as to make sure that all parts of the dish were equally covered for maintaining uniformity and also to minimize the error during the cell counting process. Similarly, the petri dishes for 24 h, 48 h and 72 h along with their respective controls were imaged. Then the cells were counted manually (four petri dishes for each time frame - three with nanoparticles and one control) and an average cell count was estimated with the results from these dishes. The cytotoxicity studies conducted during the initial 72 h reveal that there is no significant change in cell viability with BFO exposure (figure 7.8). Therefore, the BFO nanoparticles did not cause any acute cytotoxicity.

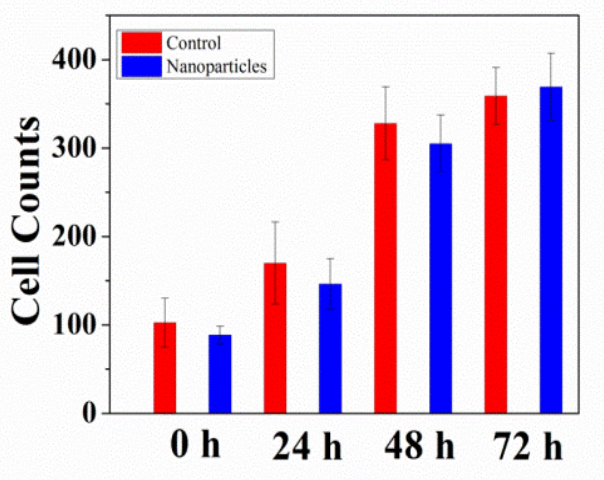

Figure 7.8 Cytotoxicity studies performed during the initial 72 h period demonstrate that BFO nanoparticles do not cause any acute cytotoxicity.

From the microscopy images as shown in figure 7.9, it can be inferred that the nanoparticles have formed clusters which most likely prevent their entry through the cell membrane. Therefore, surface functionalization of these nanoparticles is an essential task to do away with the agglomeration in order to facilitate an easy passage of these tiny structures through the cell membrane.

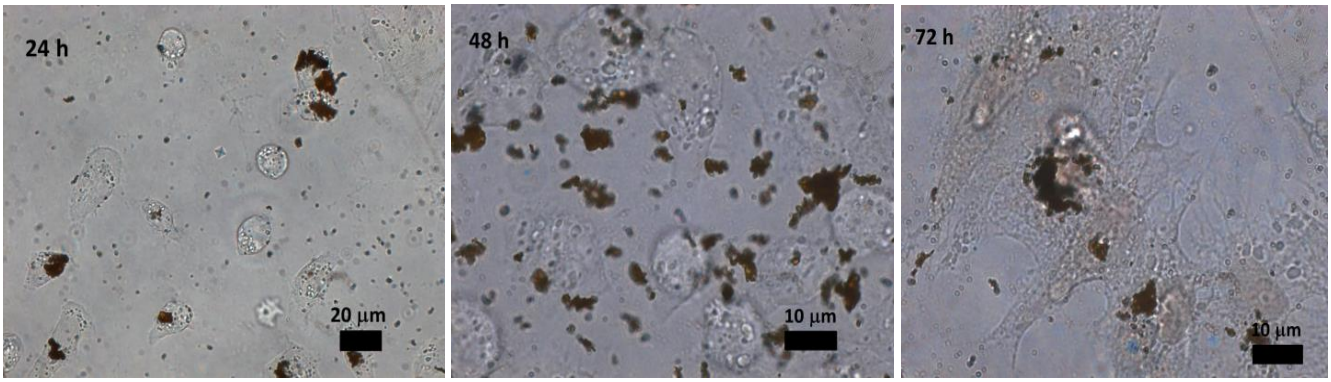

Figure 7.9 The optical images of BFO nanoparticles injected to MIA PaCa-2 Cell line after 24h, 48h and 72h showing clusters and agglomeration.

SDS-PAGE

Cells were lysed with 2% Triton X-100, centrifuged for 1 min at 1000 rpm. The supernatant was removed and the pellet containing nanoparticle-bound proteins was washed using PBS at pH 7.4. The nanoparticle-associated proteins were re-suspended in Laemmli reducing sample preparation buffer, boiled for 2 min, and used for sodium dodecyl sulfate-polyacrylamide gel electrophoresis (SDS-PAGE) [155]. SDS-PAGE was run in order to separate nanoparticle-bound proteins based upon their size. The gels were stained with Coomassie Blue overnight, de-stained for 3-4 hours, and imaged. The gels showed bands with a greater optical density for the 48 hour samples, relative to the gel background. As seen in figure 7.10, the presence of a higher volume of proteins indicates greater nanoparticle-protein binding, and therefore, 48 hours may be an ideal time for clinical treatment in the future. However, this change in optical density may be due to differences in total protein concentration in the original cell homogenates. If different proteins would have associated with the nanoparticles at later times, then it would be evident from new protein bands in the SDS-PAGE gel. Since no new bands appeared at later times, the nanoparticles most likely did not internalize into the cytoplasm or interact with any subcellular organelles.

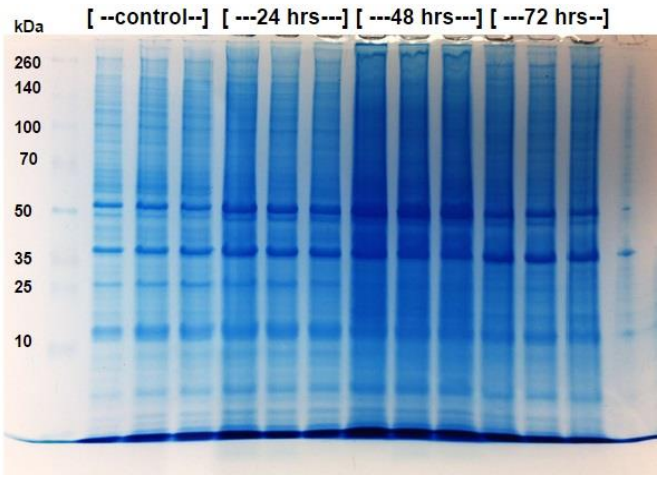

Figure 7.10 Gel image for BFO nanoparticles obtained 2-d SDS PAGE

7.4 CONCLUSIONS

The BFO nanoparticles having an approximate crystallite size of 33 nm were synthesized by the chemical co-precipitation method. From the TEM images, crystallinity of the nanoparticles were confirmed; however, excess aggregation and clustering of these particles were reported. The saturation magnetization of the BFO particles was measured to be 0.01 emu/g. Cell binding studies on these nanoparticles were conducted using the human pancreatic cancer cells (MIA PaCa-2). It was observed that the BFO nanoparticles do not cause any acute cytotoxicity over a period of 72 h. From the microscopy images and also from the SDS- PAGE results, no evidence was found for the migration of these nanoparticles across the cell membrane. The zeta potential measurements showed instability for the aqueous suspension of these BFO nanoparticles. Although our initial attempts of coating these tiny particles with dextran did not succeed, in future, we would like to surface functionalize these nanoparticles with suitable surfactants in order to avoid agglomeration and also to facilitate their entry into the cell membrane. The non-toxic nature of these nanoparticles leaves a possibility that if coated with appropriate surfactants, they can be used for multimodal imaging purposes.

CHAPTER 8

BINDING AND ENTRY OF FITC CONJUGATED DEXTRAN COATED Fe_3O_4 NANOPARTICLES INTO ARTIFICIAL LIPID MEMBRANES

8.1 INTRODUCTION

Understanding the kinetics of the binding and internalization of nanoparticles in live human cancer cell line is still a challenging topic which needs considerable research and study [156-158]. Nanoparticle-cancer cell system may be very intricate with complex interactions between the nanoparticles and the membrane proteins, carbohydrates, and lipids [158, 159]. The non-specific nanoparticle-lipid interactions are fundamental in directing the nanoparticle-cell interaction, including binding and internalization through the plasma membrane. The surface distribution, binding, and entry of nanoparticles into model lipid membranes were investigated. The primary objective of this study was to optimize these nanoparticles for multi-modal imaging purposes. We have successfully synthesized FITC conjugated dextran coated Fe_3O_4 nanoparticles and performed preliminary characterizations of these nanoparticles to model membranes.

8.2 EXPERIMENTAL PROCEDURE

Synthesis of FITC conjugated dextran coated Fe_3O_4 nanoparticles

An aqueous solutions of $FeCl_3 \cdot 6H_2O$ (5.40g) and $FeCl_2 \cdot 4H_2O$ (2.00g) were mixed in a beaker in a molar ratio of 2:1. 1 M NH_4OH solution (250 ml) was added drop wise to the mixture containing the iron salts under continuous stirring. Initially a brown precipitate was obtained, which eventually turned black as the sample continued to oxidize. After 15-20 minutes, the

precipitate was then washed with DI water until it reached a neutral pH. One half of the resulting nanoparticle solution was then separated and dried in air to obtain Fe_3O_4 nanoparticle powder (~1.00g) while the other half (~1.00g of Fe_3O_4 in 50 ml solution) was subsequently used for coating with dextran. An equal amount of dextran (~1.00g) and the nanoparticles were separately mixed in 0.5 M NaOH solution. Then the nanoparticle solution was added to the dextran drop wise under continuous sonication. After sonication for 24 hours, dextran coated Fe_3O_4 nanoparticle suspension was obtained. Then, 2 mL of Fe_3O_4 ferrofluid, 5 mL of 5 M NaOH, 1 mL of DI water and 2 mL of epichlorohydrin was mixed for 24 hours using a rotary shaker to ensure proper cross-linking of dextran coated Fe_3O_4 with the organic phase of epichlorohydrin. To remove excess epichlorohydrin, the mixture was then dialyzed several times using 6-8 kDa cut off filters. After that, 2.5 mL of concentrated NH_4OH (14 M) was added to the resulting solution to obtain amino functionalized dextran coated Fe_3O_4 nanoparticles. Finally, these nanoparticles were labeled with the green fluorescent dye Fluorescein isothiocyanate (FITC). 1 mL of 0.01 M FITC in phosphate buffer saline (PBS) with pH 7.4 was added to 1 mL of amino functionalized dextran Fe_3O_4. The mixture was then kept for 1 hour at room temperature and dialyzed using 6-8 kDa cut off filters to do away with the excess FITC.

Supported Lipid Bilayer (SLB) formed via GUV fusion

Giant unilamellar vesicles (GUVs) of 1-palmitoyl-2-oleoyl-sn-glycero-3-phosphocholine (POPC, Avanti Polar Lipids, Inc.) labeled with 0.3 mol% 1,1'-didodecyl-3,3,3',3' tetramethylindocarbocyanine perchlorate (DiI, Life Technologies) were formed by electro-formation, as described briefly below and in detail by Veatch [160]. Lipid films were made by drying the lipids in chloroform under vacuum for an hour upon a conducting indium tin oxide (ITO)-coated slide. A second ITO-coated slide and silicon spacer enclosed the dried lipids into

an incubation chamber. A hydration buffer of 200 mM sucrose was added to the dried lipid films and the ITO slides were connected to an either sides of an external AC voltage source. Growth of the GUVs occurred over 3 hours at 55 °C at AC voltage of 10 Hz and 1 Vrms. GUVs were extracted from the growth chamber and stored at 55°C until use or discarded after 3 days. The GUVs were incubated on the glass bottom dishes for 10 minutes at room temperature. The interaction between the GUVs with the plasma cleaned glass coverslip resulted in bursting of the GUVs and the formation of a continuous supported lipid bilayer over the glass. This method of SLB creation proved to create more uniform SLBs over the nanoparticles than SLBs formed by the fusion of small unilaminar vesicles. Figure 8.1 represents a microscopic image of a supported lipid bilayer.

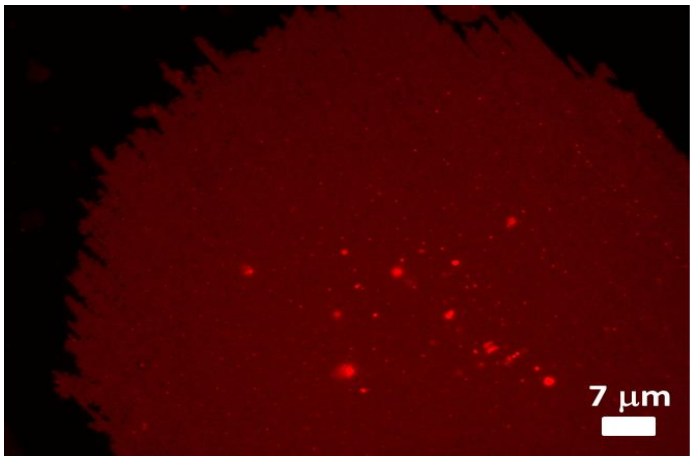

Figure 8.1 Fluorescence image of a supported lipid bilayer (SLB)

Combining SLBs and unconjugated, free FITC

To examine the effects of free FITC on the membrane, 200 μg of FITC dissolved in 1X PBS was added to the petri dish containing the lipid membrane. After 30 minutes of incubation, the resulting distribution of FITC was imaged. To test our ability to rinse away the free FITC, the

lipid surface was washed for 20 times (10×20 = 200 mL) with 1X PBS solution and the sample was imaged (figure 8.2).

Combining SLBs and FITC-dextran-conjugated nanoparticles

To examine the effects of FITC-dextran-conjugated nanoparticles on the membrane, 200 μg of FITC conjugated dextran-coated Fe_3O_4 nanoparticles were exposed to the artificial lipid membranes. After 30 minutes of incubation, the resulting distribution of nanoparticles was imaged. The lipid surface was washed for 10 times (10×10 = 100 mL) with 1X PBS solution and the sample was again imaged (figure 8.3).

8.3 RESULTS AND DISCUSSION

A sample combining an SLB and free FITC displayed a bright green background (after initial 10 washings), signifying the presence of excess FITC in solution above the membrane (figure 8.2(a)). The removal of the unbound FITC via vigorous washing (another 10 times) resulted in dramatic reduction in the FITC fluorescence from the sample and the possibility of observing stronger nanoparticle-membrane interactions (figure 8.2(b)). However, some punctuate green spots were located on the membrane after washing away the free FITC (figure 8.2(b)). This may imply that free FITC have a tendency to bind to the membrane surface and care has to be taken to resolve the differences between nanoparticle-membrane binding and free FITC-membrane binding.

FITC-dextran-nanoparticles were exposed to the membrane and unbound nanoparticles were rinsed away to reveal the strong nanoparticle-membrane interactions (figure 8.3). The dark background in this figure implies that much of the unbounded FITC was removed and few green

dots were found to get stuck to the membrane. We hypothesize that the punctate green dots which still remain seated on the membrane surface even after repeated washings demonstrate the binding of FITC conjugated dextran-coated Fe_3O_4 nanoparticles to the lipid bilayer surface. However, since free FITC alone could firmly seat on the membrane surface, greater experimentation is necessary. Furthermore, we realized that the amount of FITC used for the control experiment was large as compared to the content actually present in the conjugated Fe_3O_4 nanoparticles. Therefore, for a better comparison, we need to perform the control experiment with roughly the same amount of FITC present in the nanoparticle samples.

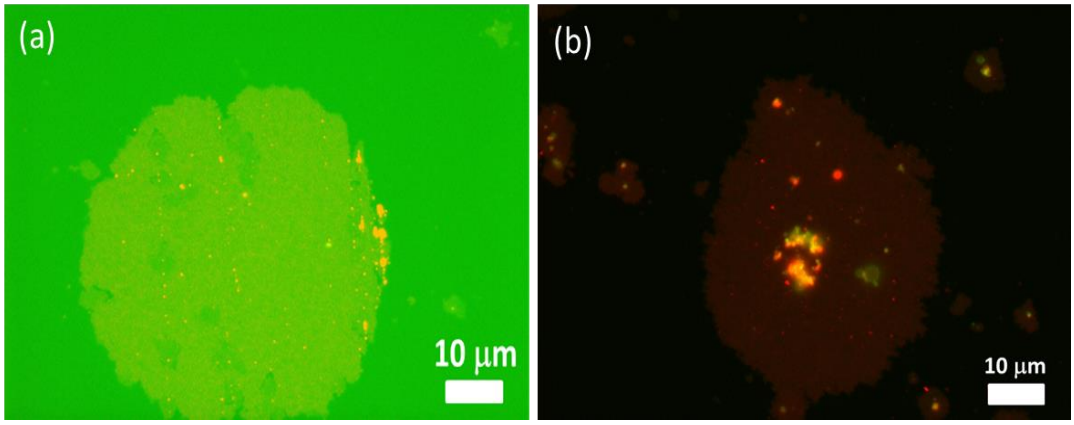

Figure 8.2 Images of SLBs after FITC addition and 30 minutes of incubation (a) after 10 washings with PBS (b) after 20 washings with PBS.

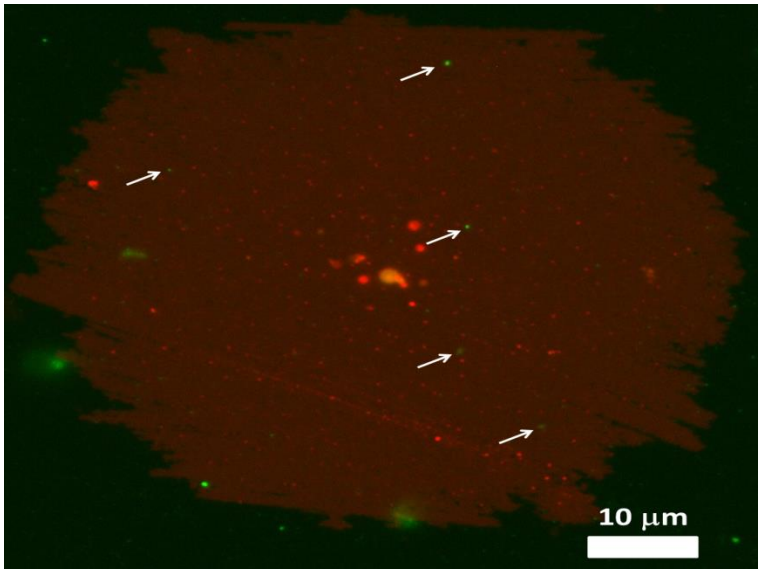

Figure 8.3 Image of a SLB following addition of FITC-conjugated Fe_3O_4 nanoparticles after 30 minutes of incubation and 10 washings with PBS. Some of the green dots shown by arrows may represent the nanoparticle binding to the artificial lipid membranes.

8.4 CONCLUSIONS

FITC-conjugated dextran-coated Fe_3O_4 nanoparticles were successfully synthesized and their interactions with artificial lipid membranes were reported. It has been observed that even after repeated washings, the FITC-dextran-nanoparticle combination firmly adhere to the surface of the lipid membrane. However, we have no proper estimate on the percentage of free FITC and free dextran available in our sample. So purification of nanoparticles in order to do away with the unbounded FITC is a challenging task and needs to be addressed before a detailed analysis of nanoparticle-membrane binding can be performed. If successful, this work would further the use of dextran-coated Fe_3O_4 nanoparticles in biomedical applications and support the targeting of Fe_3O_4 nanoparticles for multi-modal imaging and drug delivery purposes.

CHAPTER 9

CONCLUSIONS & FUTURE WORK

This dissertation focuses on two major aspects of magnetic nanoparticles, (a) understanding their fundamental physics of dipolar interactions and the relaxation dynamics and (b) their interactions with human cancer cell lines and artificial lipid bilayers. In addition to features attributed to superparamagnetism, these nanoparticles can also exhibit additional magnetic relaxation effects at very low temperatures ($\lesssim$ 50 K).Using *ac* magnetic susceptibility measurements, our studies show that the incorporation of boron, gadolinium, or lanthanum into iron oxide (Fe_3O_4) nanoparticles substantially enhances these low-temperature magnetic relaxation properties. The fact that there is no significant difference in properties on doping with magnetic Gd^{3+} and non-magnetic B^{3+} or La^{3+} suggest that structural, rather than magnetic, defects play a major role in modifying the relaxation. These results further demonstrate that the low-temperature magnetic relaxation typically observed in magnetic nanoparticles is a single-particle effect produced by structural defects and is not significantly influenced by the inter-particle dipolar interactions.

We have also investigated interaction effects in two different systems of iron oxide nanoparticles (γ-Fe_2O_3 in alginate matrix & Fe_3O_4 nanoparticles in powder form). The temperature dependent *ac* magnetic susceptibility measurements were performed to investigate the interactions among these nanoparticles. Our analysis showed that the characteristic interaction energy does not depend simply on the average spacing between the nanoparticles but is likely to be strongly influenced by the fluctuations in the nanoparticle size distribution.

The magnetic interactions in phase-pure Mn_3O_4 and composite Mn_2O_3/Mn_3O_4 nanoparticle systems having different inter-particle separations between the Mn_3O_4 ferrimagnetic cores were also studied. We found that the incorporation of boron stabilizes

the Mn_3O_4 spinel structure resulting in the formation of phase-pure nanoparticles, while in the absence of boron, the sample consists of both Mn_3O_4 and antiferromagnetic Mn_2O_3 nanoparticles. We correlate the morphology of these systems with their magnetic properties using *ac* susceptibility studies. The low temperature frequency dependent relaxation exhibits larger magnetic interactions in the phase pure Mn_3O_4 nanoparticles as compared to the Mn_3O_4/Mn_2O_3 composites, which we attribute to differences in the separation between the ferrimagnetic cores in these two samples.

We have further investigated $BiFeO_3$ nanoparticles as a potential candidate for multi-modal imaging purposes. When cultured with human pancreatic cancer cells (MIA PaCa-2), the $BiFeO_3$ nanoparticles did not show any acute cytotoxicity over a period of 72 h. However, they showed a reduced value of saturation magnetization as compared to undoped iron oxide nanoparticles and also no evidence was found for the migration of these nanoparticles across the cell membrane. The nanoparticles in aqueous solution show comparatively low values of zeta potentials implying the instability of the suspension, which is consistent with our optical and electron micrographs. Although our initial attempts of coating these tiny particles with dextran did not succeed, future experiments will achieve better stability by improved nanoparticle surface functionalization so that they can serve as carriers of anti-cancer drugs.

We have conducted a detailed investigation on the magnetic properties of Gd-doped Fe_3O_4 nanoparticles. Our studies reveal that introduction of Gd strongly influences the average crystallite size and the saturation magnetization of the Fe_3O_4 nanoparticles. The crystallite size gets larger while M_s is reduced following an increase in the Gd doping percentage. In case of magnetic hyperthermia measurements, the effective SAR decreases by a considerable amount for the nanoparticle sample with the highest doping concentration of Gd (~5 *at.*%) when compared

with undoped iron oxide ferrofluid. In future, we would also like to explore this material for possible biomedical applications in MRI as a T_1–T_2 dual-modal contrast agent.

Preliminary studies involving interactions of FITC conjugated iron oxide nanoparticles with artificial lipid bilayers were also reported. The purification of nanoparticles from free FITC was a challenging task, and, in the future, we would like to improve the purity of our nanoparticle samples for more detailed analysis of the nanoparticles interacting with membranes. Furthermore, the interactions of FITC-conjugated iron oxide based nanoparticles with live human cancer cells will also be studied to optimize these structures for advanced imaging and targeted drug/gene delivery.

In cellular physiology, pH is a vital parameter as most of the cellular processes are highly influenced by its subtle changes. Therefore, how the introduction of nanoparticles inside the cells affects the cellular pH could guide therapeutic strategies. The fluorescence intensity of the quantum dots changes with pH [161] and also these semiconductor nanoparticles exhibit low bleaching as compared to the pH sensitive dyes. Therefore, in future, with the aid of CdTe quantum dots, we would like to monitor the intracellular pH upon exposure to iron oxide nanoparticles.

REFERENCES

1. Gubin, S.P., *Magnetic Nanoparticles*. 2009: Wiley.
2. Leslie-Pelecky, D.L. and R.D. Rieke, *Magnetic properties of nanostructured materials.* Chemistry of materials, 1996. **8**(8): p. 1770-1783.
3. Delley, B. and E.F. Steigmeier, *Quantum confinement in Si nanocrystals.* Physical Review B, 1993. **47**(3): p. 1397-1400.
4. Jain, P.K., et al., *Review of some interesting surface plasmon resonance-enhanced properties of noble metal nanoparticles and their applications to biosystems.* Plasmonics, 2007. **2**(3): p. 107-118.
5. Fonseca, F., et al., *Superparamagnetism and magnetic properties of Ni nanoparticles embedded in SiO 2.* Physical Review B, 2002. **66**(10): p. 104406.
6. Yang, H.G. and H.C. Zeng, *Preparation of Hollow Anatase TiO2 Nanospheres via Ostwald Ripening.* The Journal of Physical Chemistry B, 2004. **108**(11): p. 3492-3495.
7. Park, S.-J., et al., *Synthesis and magnetic studies of uniform iron nanorods and nanospheres.* Journal of the American Chemical Society, 2000. **122**(35): p. 8581-8582.
8. Dai, Z.R., et al., *Tin Oxide Nanowires, Nanoribbons, and Nanotubes.* The Journal of Physical Chemistry B, 2002. **106**(6): p. 1274-1279.
9. Park, W.I., et al., *Metalorganic vapor-phase epitaxial growth of vertically well-aligned ZnO nanorods.* Applied Physics Letters, 2002. **80**(22): p. 4232-4234.
10. Jana, N.R., L. Gearheart, and C.J. Murphy, *Wet Chemical Synthesis of High Aspect Ratio Cylindrical Gold Nanorods.* The Journal of Physical Chemistry B, 2001. **105**(19): p. 4065-4067.

11. Liu, B. and H.C. Zeng, *Mesoscale Organization of CuO Nanoribbons: Formation of "Dandelions".* Journal of the American Chemical Society, 2004. **126**(26): p. 8124-8125.

12. Li, Y., Y. Bando, and D. Golberg, *MoS 2 nanoflowers and their field-emission properties.* Applied Physics Letters, 2003. **82**(12): p. 1962-1964.

13. Luders, U., et al., *Spin filtering through ferrimagnetic NiFe 2 O 4 tunnel barriers.* Applied physics letters, 2006. **88**(8): p. 082505-082505-3.

14. Berkowitz, A., et al., *Antiferromagnetic MnO nanoparticles with ferrimagnetic Mn 3 O 4 shells: doubly inverted core-shell system.* Physical Review B, 2008. **77**(2): p. 024403.

15. Manna, P., et al., *The magnetic proximity effect in a ferrimagnetic Fe3O4 core/ferrimagnetic γ-Mn2O3 shell nanoparticle system.* Journal of Physics: Condensed Matter, 2011. **23**(50): p. 506004.

16. Yang, F.Y. and C.L. Chien, *Spiraling Spin Structure in an Exchange-Coupled Antiferromagnetic Layer.* Physical Review Letters, 2000. **85**(12): p. 2597-2600.

17. Fiebig, M., et al., *Second harmonic generation in the centrosymmetric antiferromagnet NiO.* Physical review letters, 2001. **87**(13): p. 137202.

18. Pankhurst, Q.A., et al., *Applications of magnetic nanoparticles in biomedicine.* Journal of Physics D: Applied Physics, 2003. **36**(13): p. R167.

19. Wahab, M.A., *Solid State Physics: Structure and Properties of Materials*. 2005: Alpha Science International.

20. Mørup, S., C. Frandsen, and M.F. Hansen, *Uniform excitations in magnetic nanoparticles.* Beilstein Journal of Nanotechnology, 2010. **1**: p. 48-54.

21. Chen, X., et al., *Superparamagnetism versus superspin glass behavior in dilute magnetic nanoparticle systems.* Physical Review B, 2005. **72**(21): p. 214436.

22. Mørup, S., M.F. Hansen, and C. Frandsen, *Magnetic interactions between nanoparticles.* Beilstein Journal of Nanotechnology, 2010. **1**: p. 182-190.

23. He, Y.P., et al., *Synthesis and characterization of functionalized silica-coated Fe 3 O 4 superparamagnetic nanocrystals for biological applications.* Journal of Physics D: Applied Physics, 2005. **38**(9): p. 1342.

24. Aslibeiki, B., et al., *Superspin glass state in MnFe2O4 nanoparticles.* Journal of Magnetism and Magnetic Materials, 2010. **322**(19): p. 2929-2934.

25. Bartolome, L., et al., *Superparamagnetic [gamma]-Fe2O3 nanoparticles as an easily recoverable catalyst for the chemical recycling of PET.* Green Chemistry, 2014. **16**(1): p. 279-286.

26. Guardia, P., et al., *Surfactant effects in magnetite nanoparticles of controlled size.* Journal of Magnetism and Magnetic Materials, 2007. **316**(2): p. e756-e759.

27. Mody Vicky, V., A. Singh, and B. Wesley, *Basics of magnetic nanoparticles for their application in the field of magnetic fluid hyperthermia*, in *European Journal of Nanomedicine*. 2013. p. 11.

28. Thakur, S., S.C. Katyal, and M. Singh, *Structural and magnetic properties of nano nickel–zinc ferrite synthesized by reverse micelle technique.* Journal of Magnetism and Magnetic Materials, 2009. **321**(1): p. 1-7.

29. Brown, W.F., Jr., *Thermal Fluctuations of a Single-Domain Particle.* Physical Review, 1963. **130**(5): p. 1677-1686.

30. Shtrikman, S. and E.P. Wohlfarth, *The theory of the Vogel-Fulcher law of spin glasses.* Physics Letters A, 1981. **85**(8–9): p. 467-470.

31. Dormann, J.L., D. Fiorani, and E. Tronc, *On the models for interparticle interactions in nanoparticle assemblies: comparison with experimental results.* Journal of Magnetism and Magnetic Materials, 1999. **202**(1): p. 251-267.

32. Nadeem, K., et al., *Distinguishing magnetic blocking and surface spin-glass freezing in nickel ferrite nanoparticles.* Journal of Applied Physics, 2011. **109**(1): p. 013912-6.

33. Bae, C.J., et al., *Experimental studies of strong dipolar interparticle interaction in monodisperse Fe[sub 3]O[sub 4] nanoparticles.* Applied Physics Letters, 2007. **91**(10): p. 102502-3.

34. Winkler, E., R.D. Zysler, and D. Fiorani, *Surface and magnetic interaction effects in Mn_{3}O_{4} nanoparticles.* Physical Review B, 2004. **70**(17): p. 174406.

35. Kodama, R.H., et al., *Surface Spin Disorder in NiFe_{2}O_{4} Nanoparticles.* Physical Review Letters, 1996. **77**(2): p. 394-397.

36. Winkler, E., et al., *Surface spin-glass freezing in interacting core–shell NiO nanoparticles.* Nanotechnology, 2008. **19**(18): p. 185702.

37. Peddis, D., et al., *Spin-glass-like freezing and enhanced magnetization in ultra-small CoFe 2 O 4 nanoparticles.* Nanotechnology, 2010. **21**(12): p. 125705.

38. Tackett, R.J., et al., *Evidence of low-temperature superparamagnetism in Mn 3 O 4 nanoparticle ensembles.* Nanotechnology, 2010. **21**(36): p. 365703.

39. Tiwari, S.D. and K.P. Rajeev, *Signatures of spin-glass freezing in NiO nanoparticles.* Physical Review B, 2005. **72**(10): p. 104433.

40. Maggioni, D., et al., *Superparamagnetic iron oxide nanoparticles stabilized by a poly(amidoamine)-rhenium complex as potential theranostic probe.* Dalton Transactions, 2014. **43**(3): p. 1172-1183.

41. Cai, W., et al., *Applications of gold nanoparticles in cancer nanotechnology.* Nanotechnology, Science and Applications, 2008. **1**: p. 17-32.

42. Bhattacharyya, S., et al., *Inorganic Nanoparticles in Cancer Therapy.* Pharmaceutical Research, 2011. **28**(2): p. 237-259.

43. Jeyaraj, M., et al., *Biogenic silver nanoparticles for cancer treatment: An experimental report.* Colloids and Surfaces B: Biointerfaces, 2013. **106**(0): p. 86-92.

44. Huber, D.L., *Synthesis, Properties, and Applications of Iron Nanoparticles.* Small, 2005. **1**(5): p. 482-501.

45. Rosenholm, J.M., et al., *Targeting of Porous Hybrid Silica Nanoparticles to Cancer Cells.* ACS Nano, 2009. **3**(1): p. 197-206.

46. Soppimath, K.S., et al., *Biodegradable polymeric nanoparticles as drug delivery devices.* Journal of Controlled Release, 2001. **70**(1–2): p. 1-20.

47. AshaRani, P.V., et al., *Cytotoxicity and Genotoxicity of Silver Nanoparticles in Human Cells.* ACS Nano, 2009. **3**(2): p. 279-290.

48. Connor, E.E., et al., *Gold Nanoparticles Are Taken Up by Human Cells but Do Not Cause Acute Cytotoxicity.* Small, 2005. **1**(3): p. 325-327.

49. Sharma, V., et al., *DNA damaging potential of zinc oxide nanoparticles in human epidermal cells.* Toxicology Letters, 2009. **185**(3): p. 211-218.

50. Lin, W., et al., *In vitro toxicity of silica nanoparticles in human lung cancer cells.* Toxicology and Applied Pharmacology, 2006. **217**(3): p. 252-259.

51. Lin, W., et al., *Toxicity of cerium oxide nanoparticles in human lung cancer cells.* International Journal of Toxicology, 2006. **25**(6): p. 451-457.

52. Gupta, A.K. and M. Gupta, *Synthesis and surface engineering of iron oxide nanoparticles for biomedical applications.* Biomaterials, 2005. **26**(18): p. 3995-4021.

53. Yu, M.K., et al., *Drug-loaded superparamagnetic iron oxide nanoparticles for combined cancer imaging and therapy in vivo.* Angewandte Chemie International Edition, 2008. **47**(29): p. 5362-5365.

54. Kievit, F.M. and M. Zhang, *Surface engineering of iron oxide nanoparticles for targeted cancer therapy.* Accounts of chemical research, 2011. **44**(10): p. 853-862.

55. Santra, S., et al., *Drug/Dye-Loaded, Multifunctional Iron Oxide Nanoparticles for Combined Targeted Cancer Therapy and Dual Optical/Magnetic Resonance Imaging.* small, 2009. **5**(16): p. 1862-1868.

56. Mahmoudi, M., et al., *Magnetic resonance imaging tracking of stem cells in vivo using iron oxide nanoparticles as a tool for the advancement of clinical regenerative medicine.* Chemical Reviews, 2010. **111**(2): p. 253-280.

57. Ito, A., et al., *Tissue engineering using magnetite nanoparticles and magnetic force: heterotypic layers of cocultured hepatocytes and endothelial cells.* Tissue engineering, 2004. **10**(5-6): p. 833-840.

58. Dobson, J., *Magnetic nanoparticles for drug delivery.* Drug Development Research, 2006. **67**(1): p. 55-60.

59. Arruebo, M., et al., *Magnetic nanoparticles for drug delivery.* Nano Today, 2007. **2**(3): p. 22-32.

60. Ito, A., et al., *Medical application of functionalized magnetic nanoparticles.* Journal of Bioscience and Bioengineering, 2005. **100**(1): p. 1-11.

61. Laha, S.S., R. Regmi, and G. Lawes, *Structural origin for low-temperature relaxation features in magnetic nanoparticles.* Journal of Physics D: Applied Physics, 2013. **46**(32): p. 325004.

62. Berry, C.C. and A.S.G. Curtis, *Functionalisation of magnetic nanoparticles for applications in biomedicine.* Journal of Physics D: Applied Physics, 2003. **36**(13): p. R198.

63. Chen, F.-H., et al., *Synthesis of a novel magnetic drug delivery system composed of doxorubicin-conjugated Fe3O4 nanoparticle cores and a PEG-functionalized porous silica shell.* Chemical Communications, 2010. **46**(45): p. 8633-8635.

64. Nigam, S., et al., *Poly(ethylene glycol)-Modified PAMAM-Fe3O4-Doxorubicin Triads with the Potential for Improved Therapeutic Efficacy: Generation-Dependent Increased Drug Loading and Retention at Neutral pH and Increased Release at Acidic pH.* Langmuir, 2014. **30**(4): p. 1004-1011.

65. Akbarzadeh, A., et al., *Preparation and in vitro evaluation of doxorubicin-loaded Fe3O4 magnetic nanoparticles modified with biocompatible copolymers.* International journal of nanomedicine, 2012. **7**: p. 511.

66. Guardia, P., et al., *Water-Soluble Iron Oxide Nanocubes with High Values of Specific Absorption Rate for Cancer Cell Hyperthermia Treatment.* ACS Nano, 2012. **6**(4): p. 3080-3091.

67. Hee Kim, E., et al., *Synthesis of ferrofluid with magnetic nanoparticles by sonochemical method for MRI contrast agent.* Journal of Magnetism and Magnetic Materials, 2005. **289**(0): p. 328-330.

68. Catherine, C.B., *Progress in functionalization of magnetic nanoparticles for applications in biomedicine.* Journal of Physics D: Applied Physics, 2009. **42**(22): p. 224003.

69. Crozier, K.B., et al., *Plasmonics for surface enhanced raman scattering: Nanoantennas for single molecules.* Selected Topics in Quantum Electronics, IEEE Journal of, 2014. **20**(3): p. 152-162.

70. Nemala, H.B., *Investigation Of Temperature Dependent Magnetic Hyperthermia In Fe3O4 Ferrofluids*, in *Wayne State University Dissertations. Paper 1159.* 2015.

71. Gossuin, Y., et al., *Magnetic resonance relaxation properties of superparamagnetic particles.* Wiley Interdisciplinary Reviews: Nanomedicine and Nanobiotechnology, 2009. **1**(3): p. 299-310.

72. Salado, J., et al., *Synthesis and magnetic properties of monodisperse Fe3O4 nanoparticles with controlled sizes.* Journal of Non-Crystalline Solids, 2008. **354**(47–51): p. 5207-5209.

73. Mandal, M., et al., *Magnetite nanoparticles with tunable gold or silver shell.* Journal of Colloid and Interface Science, 2005. **286**(1): p. 187-194.

74. Ronald, J.T., W.B. Abdul, and E.B. Cristian, *Dynamic susceptibility evidence of surface spin freezing in ultrafine NiFe 2 O 4 nanoparticles.* Nanotechnology, 2009. **20**(44): p. 445705.

75. Hochepied, J.F. and M.P. Pileni, *Magnetic properties of mixed cobalt--zinc ferrite nanoparticles.* Journal of Applied Physics, 2000. **87**(5): p. 2472-2478.

76. Kahn, M.L. and Z.J. Zhang, *Synthesis and magnetic properties of CoFe[sub 2]O[sub 4] spinel ferrite nanoparticles doped with lanthanide ions.* Applied Physics Letters, 2001. **78**(23): p. 3651-3653.

77. Burianova, S., et al., *Surface spin effects in La-doped CoFe[sub 2]O[sub 4] nanoparticles prepared by microemulsion route.* Journal of Applied Physics, 2011. **110**(7): p. 073902-7.

78. Suzuki, M., et al., *Observation of superspin-glass behavior in Fe_{3}O_{4} nanoparticles.* Physical Review B, 2009. **79**(2): p. 024418.

79. Liang, X., et al., *Synthesis of Nearly Monodisperse Iron Oxide and Oxyhydroxide Nanocrystals.* Advanced Functional Materials, 2006. **16**(14): p. 1805-1813.

80. Huan, W., et al., *A Study on the Magnetic and Photoluminescence Properties of Eun+ and Sm3+ Doped Fe3O4 Nanoparticles.* Journal of Nanoscience and Nanotechnology, 2012. **12**(6): p. 4621-4634.

81. Kim, Y.-I., et al., *Preferential site of Gd in Gd-doped Fe3O4 nanopowder.* Journal of nanoscience and nanotechnology, 2011. **11**(1): p. 810-814.

82. Zhao, B. and Z. Nan, *One-pot synthesis of ZnLaxFe2-xO4 clusters without any template and their possible application in water treatment.* Journal of Materials Chemistry, 2012. **22**(14): p. 6581-6586.

83. Tripathy, D., et al., *Magnetic and transport properties of Co-doped Fe[sub 3]O[sub 4] films.* Journal of Applied Physics, 2007. **101**(1): p. 013904-6.

84. Binu, P.J., et al., *Effect of Gd 3+ doping on the structural and magnetic properties of nanocrystalline Ni–Cd mixed ferrite.* Physica Scripta, 2011. **84**(4): p. 045702.

85. Wen-Chen, Z., W. Shao-Yi, and Z. Jian, *Investigations of the electron paramagnetic resonance parameters and atomic positions for Co 2+ ions in 3C-, 2H- and 4H-ZnS.* Semiconductor Science and Technology, 2002. **17**(5): p. 493.

86. Lu, Y.-W., Q.-S. Zhu, and F.-X. Liu, *Magnetic properties of tin-doped magnetite nanoparticles.* Physics Letters A, 2006. **359**(1): p. 66-69.

87. More, S.S., et al., *Cation distribution in nanocrystalline Al3+ and Cr3+ co-substituted CoFe2O4.* Journal of Alloys and Compounds, 2010. **502**(2): p. 477-479.

88. Julien, C., *Local structure and electrochemistry of lithium cobalt oxides and their doped compounds.* Solid State Ionics, 2003. **157**(1–4): p. 57-71.

89. Drake, P., et al., *Gd-doped iron-oxide nanoparticles for tumour therapy via magnetic field hyperthermia.* Journal of Materials Chemistry, 2007. **17**(46): p. 4914-4918.

90. Cao, S.-W., Y.-J. Zhu, and J. Chang, *Fe3O4 polyhedral nanoparticles with a high magnetization synthesized in mixed solvent ethylene glycol-water system.* New Journal of Chemistry, 2008. **32**(9): p. 1526-1530.

91. Legodi, M.A. and D. de Waal, *The preparation of magnetite, goethite, hematite and maghemite of pigment quality from mill scale iron waste.* Dyes and Pigments, 2007. **74**(1): p. 161-168.

92. Ni, S., et al., *Low temperature synthesis of Fe3O4 nanoparticles and its application in lithium ion batteries.* Materials Chemistry and Physics, 2011. **130**(3): p. 1260-1264.

93. Feldman, C., *Evaporation of boron from acid solutions and residue.* Analytical Chemistry, 1961. **33**(13): p. 1916-1920.

94. Tackett, R., et al., *Magnetic and optical response of tuning the magnetocrystalline anisotropy in Fe3O4 nanoparticle ferrofluids by Co doping.* Journal of Magnetism and Magnetic Materials, 2008. **320**(21): p. 2755-2759.

95. Tripathy, D., et al., *Effect of cobalt doping concentration on the structural and magnetic properties of Fe3O4.* Thin Solid Films, 2006. **505**(1–2): p. 45-49.

96. Pérez, N., et al., *Surface anisotropy broadening of the energy barrier distribution in magnetic nanoparticles.* Nanotechnology, 2008. **19**(47): p. 475704.

97. Tackett, R.J., A.W. Bhuiya, and C.E. Botez, *Dynamic susceptibility evidence of surface spin freezing in ultrafine NiFe 2 O 4 nanoparticles.* Nanotechnology, 2009. **20**(44): p. 445705.

98. Jonsson, T., et al., *Aging in a Magnetic Particle System.* Physical Review Letters, 1995. **75**(22): p. 4138-4141.

99. Dormann, J.L., et al., *From pure superparamagnetic regime to glass collective state of magnetic moments in γ-Fe2O3 nanoparticle assemblies.* Journal of Magnetism and Magnetic Materials, 1998. **187**(2): p. L139-L144.

100. Fleutot, S., et al., *Spacing-dependent dipolar interactions in dendronized magnetic iron oxide nanoparticle 2D arrays and powders.* Nanoscale, 2013. **5**(4): p. 1507-1516.

101. Rumpf, K., et al., *Magnetic Properties of an Iron Oxide/Porous Silicon System Controlled by Magnetic Interactions.* ECS Transactions, 2013. **50**(37): p. 83-86.

102. Pauly, M., et al., *Size dependent dipolar interactions in iron oxide nanoparticle monolayer and multilayer Langmuir-Blodgett films.* Journal of Materials Chemistry, 2012. **22**(13): p. 6343-6350.

103. Frankamp, B.L., et al., *Direct Control of the Magnetic Interaction between Iron Oxide Nanoparticles through Dendrimer-Mediated Self-Assembly.* Journal of the American Chemical Society, 2005. **127**(27): p. 9731-9735.

104. Dormann, J.L., et al., *Effect of interparticle interactions on the dynamical properties of γ-Fe2O3 nanoparticles.* Journal of Magnetism and Magnetic Materials, 1998. **183**(3): p. L255-L260.

105. Dormann, J.L., L. Bessais, and D. Fiorani, *A dynamic study of small interacting particles: superparamagnetic model and spin-glass laws.* Journal of Physics C: Solid State Physics, 1988. **21**(10): p. 2015.

106. Pal, S., et al., *Synthesis and magnetic properties of gold coated iron oxide nanoparticles.* Journal of Applied Physics, 2009. **105**(7): p. -.

107. Kroll, E., F.M. Winnik, and R.F. Ziolo, *In Situ Preparation of Nanocrystalline γ-Fe2O3 in Iron(II) Cross-Linked Alginate Gels.* Chemistry of Materials, 1996. **8**(8): p. 1594-1596.

108. Vallat-Sauvain, E., et al., *Evolution of the microstructure in microcrystalline silicon prepared by very high frequency glow-discharge using hydrogen dilution.* Journal of Applied Physics, 2000. **87**(6): p. 3137-3142.

109. Leite, E.S., et al., *Spin-glass-like characteristics of extremely small γ-Fe 2 O 3 nanoparticles.* Journal of Physics: Conference Series, 2010. **200**(7): p. 072060.

110. Guimin, A., et al., *Low-temperature synthesis of Mn 3 O 4 nanoparticles loaded on multi-walled carbon nanotubes and their application in electrochemical capacitors.* Nanotechnology, 2008. **19**(27): p. 275709.

111. Baykal, A., Y. Köseoğlu, and M. Şenel, *Low temperature synthesis and characterization of Mn3O4 nanoparticles.* Central European Journal of Chemistry, 2007. **5**(1): p. 169-176.

112. Vázquez-Olmos, A., et al., *One-step synthesis of Mn3O4 nanoparticles: Structural and magnetic study.* Journal of Colloid and Interface Science, 2005. **291**(1): p. 175-180.

113. Regmi, R., R. Tackett, and G. Lawes, *Suppression of low-temperature magnetic states in Mn3O4 nanoparticles.* Journal of Magnetism and Magnetic Materials, 2009. **321**(15): p. 2296-2299.

114. Gopalakrishnan, I.K., et al., *Synthesis of superparamagnetic Mn3O4 nanocrystallites by ultrasonic irradiation.* Journal of Crystal Growth, 2005. **280**(3–4): p. 436-441.

115. Wang, Z.H., et al., *Magnetic properties and exchange bias in Mn[sub 2]O[sub 3]/Mn[sub 3]O[sub 4] nanoclusters.* Journal of Applied Physics, 2009. **105**(7): p. 07A315-3.

116. Oxford, G.A.E. and A.M. Chaka, *Density functional theory study of the γ-MnOOH (010) surface: Response to oxygen and water partial pressures and temperature.* Physical Review B, 2011. **84**(20): p. 205453.

117. Orchard, A.F., *Magnetochemistry*. 2007, Oxford: Oxford University Press.

118. Vijayakumar, R., et al., *Sonochemical synthesis and characterization of pure nanometer-sized Fe3O4 particles.* Materials Science and Engineering: A, 2000. **286**(1): p. 101-105.

119. Daniela, C., C. Gabriel, and J.O.C. Charles, *Magnetic properties of variable-sized Fe 3 O 4 nanoparticles synthesized from non-aqueous homogeneous solutions of polyols.* Journal of Physics D: Applied Physics, 2007. **40**(19): p. 5801.

120. Zhang, H., et al., *Organization of Mn3O4 nanoparticles into [gamma]-MnOOH nanowires via hydrothermal treatment of the colloids induced by laser ablation in water.* CrystEngComm, 2011. **13**(4): p. 1063-1066.

121. Gillot, B., M. El Guendouzi, and M. Laarj, *Particle size effects on the oxidation–reduction behavior of Mn3O4 hausmannite.* Materials Chemistry and Physics, 2001. **70**(1): p. 54-60.

122. Rabiei, S., et al., *Conversion of hausmanite (Mn3O4) particles to nano-fibrous manganite (MnOOH) at ambient conditions.* Journal of Materials Science, 2005. **40**(18): p. 4995-4998.

123. Thirunakaran, R., et al., *Solution synthesis of boron substituted LiMn2O4 spinel oxide for use in lithium rechargeable battery.* Ionics, 2004. **10**(3-4): p. 188-192.

124. McKee, D.W., *Oxidation behavior and protection of carbon/carbon composites.* Carbon, 1987. **25**(4): p. 551-557.

125. López-Ortega, A., et al., *Size-Dependent Passivation Shell and Magnetic Properties in Antiferromagnetic/Ferrimagnetic Core/Shell MnO Nanoparticles.* Journal of the American Chemical Society, 2010. **132**(27): p. 9398-9407.

126. Ortega-San Martin, L., et al., *Magnetic Properties of the Ordered Double Perovskite Sr2MnTeO6.* European Journal of Inorganic Chemistry, 2006. **2006**(7): p. 1362-1370.

127. Winkler, E., et al., *Dynamic study of the internal magnetic order of Mn3O4 nanoparticles.* Journal of Nanoparticle Research, 2011. **13**(11): p. 5653-5659.

128. Pankhurst, Q.A., et al., *Applications of magnetic nanoparticles in biomedicine.* Journal of physics D: Applied physics, 2003. **36**(13): p. R167.

129. Liu, J., Y. Bin, and M. Matsuo, *Magnetic Behavior of Zn-Doped Fe3O4 Nanoparticles Estimated in Terms of Crystal Domain Size.* The Journal of Physical Chemistry C, 2012. **116**(1): p. 134-143.

130. Bao, J., et al., *Bifunctional Au-Fe3O4 Nanoparticles for Protein Separation.* ACS Nano, 2007. **1**(4): p. 293-298.

131. Qu, B., et al., *Significant improvement of critical current density in MgB 2 doped with ferromagnetic Fe 3 O 4 nanoparticles.* Superconductor Science and Technology, 2009. **22**(1): p. 015027.

132. Du, G.H., et al., *Characterization and application of Fe3O4/SiO2 nanocomposites.* Journal of Sol-Gel Science and Technology, 2006. **39**(3): p. 285-291.

133. Hongting, P. and J. Fengjing, *Towards high sedimentation stability: magnetorheological fluids based on CNT/Fe 3 O 4 nanocomposites.* Nanotechnology, 2005. **16**(9): p. 1486.

134. Yang, T.-I., et al., *Magneto-dielectric properties of polymer– nanocomposites.* Journal of Magnetism and Magnetic Materials, 2008. **320**(21): p. 2714-2720.

135. Peng, J., et al., *Hydrothermal synthesis and magnetic properties of gadolinium-doped CoFe2O4 nanoparticles.* Journal of Magnetism and Magnetic Materials, 2011. **323**(1): p. 133-137.

136. Xiao, N., et al., *T1–T2 dual-modal MRI of brain gliomas using PEGylated Gd-doped iron oxide nanoparticles.* Journal of Colloid and Interface Science, 2014. **417**(0): p. 159-165.

137. Panda, R.N., J.C. Shih, and T.S. Chin, *Magnetic properties of nano-crystalline Gd- or Pr-substituted CoFe2O4 synthesized by the citrate precursor technique.* Journal of Magnetism and Magnetic Materials, 2003. **257**(1): p. 79-86.

138. Tahar, L.B., et al., *Characterization and magnetic properties of Sm- and Gd-substituted CoFe2O4 nanoparticles prepared by forced hydrolysis in polyol.* Materials Research Bulletin, 2007. **42**(11): p. 1888-1896.

139. Yim, H., S. Seo, and K. Na, *MRI contrast agent-based multifunctional materials: diagnosis and therapy.* Journal of Nanomaterials, 2011. **2011**: p. 19.

140. Krishnan, K.M., *Biomedical nanomagnetics: a spin through possibilities in imaging, diagnostics, and therapy.* Magnetics, IEEE Transactions on, 2010. **46**(7): p. 2523-2558.

141. Jena, B.P. and D.J. Taatjes, *NanoCellBiology: Multimodal Imaging in Biology and Medicine*. 2014: Pan Stanford.

142. Osseni, S.A., et al., *Gadolinium oxysulfide nanoparticles as multimodal imaging agents for T 2-weighted MR, X-ray tomography and photoluminescence.* Nanoscale, 2014. **6**(1): p. 555-564.

143. Thorek, D.L., et al., *Superparamagnetic iron oxide nanoparticle probes for molecular imaging.* Annals of biomedical engineering, 2006. **34**(1): p. 23-38.

144. Benford, S.M. and G.V. Brown, *T-S diagram for gadolinium near the Curie temperature.* Journal of Applied Physics, 1981. **52**(3): p. 2110-2112.

145. Laha, S.S., R. Mukherjee, and G. Lawes, *Interactions and magnetic relaxation in boron doped Mn 3 O 4 nanoparticles.* Materials Research Express, 2014. **1**(2): p. 025032.

146. Laha, S.S., R.J. Tackett, and G. Lawes, *Interactions in γ-Fe2O3 and Fe3O4 nanoparticle systems.* Physica B: Condensed Matter, 2014. **448**(0): p. 69-72.

147. Nemala, H., et al., *Investigation of magnetic properties of Fe3O4 nanoparticles using temperature dependent magnetic hyperthermia in ferrofluids.* Journal of Applied Physics, 2014. **116**(3): p. 034309.

148. Mocherla, P.S.V., et al., *Tunable bandgap in BiFeO3 nanoparticles: The role of microstrain and oxygen defects.* Applied Physics Letters, 2013. **103**(2): p. 022910.

149. Dutta, D.P., et al., *Magnetic, Ferroelectric, and Magnetocapacitive Properties of Sonochemically Synthesized Sc-Doped BiFeO3 Nanoparticles.* The Journal of Physical Chemistry C, 2013. **117**(5): p. 2382-2389.

150. Huang, F., et al., *Peculiar magnetism of BiFeO3 nanoparticles with size approaching the period of the spiral spin structure.* Sci. Rep., 2013. **3**.

151. Lotey, G. and N.K. Verma, *Structural, magnetic, and electrical properties of Gd-doped BiFeO3 nanoparticles with reduced particle size.* Journal of Nanoparticle Research, 2012. **14**(3): p. 1-11.

152. Chakrabarti, K., et al., *Enhanced magnetic and dielectric properties of Eu and Co co-doped BiFeO3 nanoparticles.* Applied Physics Letters, 2012. **101**(4): p. 042401.

153. Shima, H., H. Naganuma, and S. Okamura, *Optical Properties of Multiferroic BiFeO3 Films*. Materials Science - Advanced Topics. 2013.

154. Bhushan, B., et al., *Enhancing the magnetic characteristics of BiFeO3 nanoparticles by Ca, Ba co-doping.* Materials Chemistry and Physics, 2012. **135**(1): p. 144-149.

155. Laemmli, U.K., *Cleavage of structural proteins during the assembly of the head of bacteriophage T4.* nature, 1970. **227**(5259): p. 680-685.

156. Peer, D., et al., *Nanocarriers as an emerging platform for cancer therapy.* Nat Nano, 2007. **2**(12): p. 751-760.

157. Kim, K.Y., *Nanotechnology platforms and physiological challenges for cancer therapeutics.* Nanomedicine: Nanotechnology, Biology and Medicine, 2007. **3**(2): p. 103-110.

158. Verma, A. and F. Stellacci, *Effect of Surface Properties on Nanoparticle–Cell Interactions.* Small, 2010. **6**(1): p. 12-21.

159. Giustini, A.J., et al., *Noninvasive assessment of magnetic nanoparticle-cancer cell interactions.* Integrative Biology, 2012. **4**(10): p. 1283-1288.

160. Veatch, S.L., *From small fluctuations to large-scale phase separation: Lateral organization in model membranes containing cholesterol.* Seminars in Cell & Developmental Biology, 2007. **18**(5): p. 573-582.

161. Kim, J., et al., *Highly fluorescent CdTe quantum dots with reduced cytotoxicity-A Robust biomarker.* Sensing and Bio-Sensing Research, 2015. **3**: p. 46-52.

ABSTRACT

UNDERSTANDING THE PHYSICS OF MAGNETIC NANOPARTICLES AND THEIR APPLICATIONS IN THE BIOMEDICAL FIELD

by

SUVRA SANTA LAHA

August 2015

Co- Advisors: Prof. Christopher V. Kelly & Prof. Bhanu P. Jena

Major: Physics

Degree: Doctor of Philosophy

The study of magnetic nanoparticles is of great interest because of their potential uses in magnetic-recording, medical diagnostic and therapeutic applications. Additionally, they also offer an opportunity to understand the physics underlying the complex behavior exhibited by these materials. Two of the most important relaxation phenomena occurring in magnetic nanoparticles are superparamagnetic blocking and spin-glass-like freezing. In addition to features attributed to superparamagnetism, these nanoparticles can also exhibit magnetic relaxation effects at very low temperatures ($\lesssim 50$ K). Our studies suggest that all structural defects, and not just surface spins, are responsible for the low-temperature glass-like relaxation observed in many magnetic nanoparticles. The characteristic dipolar interaction energy existing in an ensemble of magnetic nanoparticles does not apparently depend on the average spacing between the nanoparticles but is likely to be strongly influenced by the fluctuations in the nanoparticle distribution. Our findings revealed that incorporating a small percentage of boron can stabilize the spinel structure in Mn_3O_4 nanoparticles. We have also demonstrated that the dipolar interactions between the magnetic cores can be tuned by introducing non-magnetic nanoparticles. In particular, we studied the magnetic properties of Gd-doped Fe_3O_4 nanoparticles, a potential

applicant for T_1–T_2 dual-modal MRI contrast agent. We have explored the interactions of $BiFeO_3$ nanoparticles on live cells and the binding of FITC-conjugated Fe_3O_4 nanoparticles with artificial lipid membranes to investigate these materials as candidates in medical imaging. Taken together, these studies have advanced our understanding of the fundamental physical principles that governs magnetism in magnetic materials with a focus on developing these nanoparticles for advanced biomedical applications. The materials developed and studied expand the repertoire of tools available for multimodal imaging, using both x-ray and magnetic resonance.

AUTOBIOGRAPHICAL STATEMENT

EDUCATION

PhD (Physics): Wayne State University, Detroit, USA, 2010 - 2015
MS (Physics): Wayne State University, Detroit, USA, 2010 - 2012
MSc (Physics): Indian Institute of Technology Guwahati, INDIA, 2007 - 2009
BSc (Physics Honours): University of Calcutta, INDIA, 2004 – 2007

PUBLICATIONS

1) Joseph T. Rakowski, **Suvra S. Laha**, Matthew G. Buczek, Michael G. Snyder, Mark A. Tucker, Yair Hillman, Gavin Lawes; Measurement of gold nanoparticle dose enhancement using unlaminated radiochromic film**.** ***Medical Physics*** (*UNDER EDITORIAL REVIEW*)

2) **S.S.Laha,** R.Mukherjee, G.Lawes; Interactions and magnetic relaxation in boron doped Mn_3O_4 nanoparticles. ***Materials Research Express*** 2014, **1**(2), 025032.

3) **S.S.Laha,** R.J.Tackett, G.Lawes; Interactions in γ -Fe_2O_3 and Fe_3O_4 nanoparticle systems. ***Physica B: Condensed Matter*** 2014, **448**, 69-72.

4) **S.S.Laha,** R.Regmi, G.Lawes; Structural origin for low-temperature relaxation features in magnetic nanoparticles. ***Journal of Physics D: Applied Physics*** 2013**, 46** (32), 325004.

5) A.Nath, **S.S.Laha,** A.Khare; Effect of focusing conditions on synthesis of titanium oxide nanoparticles via laser ablation in titanium–water interface. ***Applied Surface Science*** 2011**, 257** (7), 3118-3122.

6) A.Nath, **S.S.Laha,** A.Khare; Synthesis of TiO_2 Nanoparticles Via Laser Ablation at Titanium-Water Interface. ***Integrated Ferroelectrics*** 2010**, 121** (1), 58-64.

FELLOWSHIPS AND AWARDS

1. Awarded ***"Summer Dissertation Fellowship"*** by the Graduate School at Wayne State University for Spring/Summer 2015.

2. Awarded ***"Thomas C. Rumble University Fellowship"*** by the Graduate School at Wayne State University during the academic year Aug. 2013- May 2014.

3. Won ***"Best Poster Award"*** at American Physical Society (APS) Ohio-Region Section Meeting held in Detroit during October 2012.